ABSTRACT

Title of dissertation: MARS OZONE ABUNDANCES FROM INFRARED HETERODYNE SPECTRA AND THEIR APPLICATION TO THE STUDY OF THE STABILITY OF THE MARTIAN ATMOSPHERE

Kelly Elizabeth Fast, Doctor of Philosophy, 2005

Dissertation directed by: Professor Michael F. A'Hearn
Department of Astronomy

The stability of the carbon dioxide atmosphere of Mars is thought to be maintained through catalytic chemistry involving "odd hydrogen" products of water vapor photolysis. Ozone is destroyed by odd hydrogen and therefore its abundance is an excellent tracer of those species that play a vital role in reforming carbon dioxide. Photochemical models of the atmosphere of Mars rely on observables such as ozone to test their predictions.

Infrared heterodyne spectroscopy with a spectral resolution $\geq 10^6$ is the only technique that can directly measure ozone in the Martian atmosphere from the surface of the Earth. Observations were made using the Goddard Infrared Heterodyne Spectrometer and Heterodyne Instrument for Planetary Wind and Composition at the NASA Infrared Telescope Facility. Ozone abundances from seven data sets taken between 1988 and

2003 are presented, along with observation and analysis techniques. Measured spatial, seasonal, and orbital variability of total ozone column abundance is compared to that predicted by the first three-dimensional gas phase photochemical model of Mars. Overall agreement in the behavior of ozone across aphelion and perihelion periods supports the theory that odd hydrogen chemistry is responsible for maintaining the stability of the carbon dioxide atmosphere. Underestimation of modeled low latitude ozone around aphelion may indicate the suppression of odd hydrogen abundance through heterogeneous processes involving water ice clouds. The weak but not strict anticorrelation of the observed total column densities of ozone and water supports the role that the altitude distribution of water vapor is thought to play in regulating ozone abundance. Ozone abundances from this work are compared with those retrieved using ultraviolet techniques, showing generally good agreement. Techniques for extracting ozone altitude distribution are investigated by incorporating $O_2(^1\Delta)$ dayglow observations which indirectly probe ozone above ~20 km altitude.

The abundance and altitude distribution of ozone in the Earth's atmosphere retrieved from calibration spectra are compared to nearby contemporaneous measurements using Dobson, lidar, and ozonesonde techniques. Excellent agreement with altitude distribution measured by lidar and ozonesonde is achieved when total ozone column densities from Dobson spectrophotometry are used as a constraint in the radiative transfer analysis of the spectra.

MARS OZONE ABUNDANCES FROM INFRARED HETERODYNE SPECTRA AND THEIR APPLICATION TO THE STUDY OF THE STABILITY OF THE MARTIAN ATMOSPHERE

by

Kelly Elizabeth Fast

Dissertation submitted to the Faculty of the Graduate School of the
University of Maryland, College Park in partial fulfillment
of the requirements for the degree of
Doctor of Philosophy
2005

Advisory Committee:

Professor Michael F. A'Hearn, Chair
Dr. Theodor Kostiuk
Professor Douglas Hamilton
Professor Robert Hudson
Dr. Rosemary Killen
Dr. Vladimir Krasnopolsky

©Copyright by

Kelly Elizabeth Fast

2005

Dedication

To Don, Kirsten, and Nathan

God could provide no greater blessing here on Earth than you.
I could not have done this without you.

By the way, I promise not to park my spaceship on the grass.

To Mom & Dad

Thank you so much for your unending support and love.

Do you still want a refund from CH?

To Grandpa Brown

♫ …I'll be looking at the Moon, but I'll be seeing you… ♫

Acknowledgements

There are many people who have provided guidance, data, software, and encouragement throughout this long project. I would like to extend my deepest, heartfelt thanks to:

- Prof. Michael A'Hearn for serving as my advisor at the University of Maryland, College Park, in spite of his very busy schedule as the principle investigator on the Deep Impact mission.
- Dr. Theodor Kostiuk for serving as my advisor at NASA's Goddard Space Flight Center and for his support and guidance over the years.
- Prof. Douglas Hamilton, Prof. Robert Hudson, Dr. Rosemary Killen, and Dr. Vladimir Krasnopolsky for serving on my dissertation committee.
- Dr. Tilak Hewegama for maintaining the BEAMINT radiative transfer software and for modifying it to allow me to explore new analysis techniques.
- Dr. Gene Francis for providing assistance with the GENLN2 radiative transfer software.
- Dr. Michael Smith for providing Mars Global Surveyor Thermal Emission Spectrometer data, and for informative discussions.
- Dr. Ann Sprague for providing water vapor abundance data for Mars.
- Dr. Vladimir Krasnopolsky and Dr. Robert Novak for providing $O_2(^1\Delta)$ dayglow data for Mars and for informative discussions.
- Dr. R. Todd Clancy for providing HST-FOS ozone data for Mars.
- Dr. Franck Lefèvre and Dr. Sebastien Lebonnois for providing listings of their three-dimensional photochemical model of the atmosphere of Mars.
- Dr. Stuart McDermid, Dr. Thierry LeBlanc, Dr. Samuel Oltmans and Dr. John Barnes for providing Mauna Loa Observatory data.
- The directors and staff of the NASA Infrared Telescope Facility for supporting the infrared heterodyne observations of ozone on Mars over the years.
- Dr. Timothy Livengood, Dr. Guido Sonnabend, John Annen, Dr. David Buhl, and Juan Delgado for their support.
- Fred Espenak for seeing the potential of infrared heterodyne spectroscopy for studying ozone on Mars, for carrying out observations in the 1980s and 1990s, and for providing insight and guidance.
- Dr. Drake Deming, Frank Ottens, Dr. John Trasco, Grace Deming, and Dr. Theodor Kostiuk for seeing the potential in me that I had yet to see.

Table of Contents

Chapter 1: Introduction 1
I. Mars 1
II. The CO_2 Stability Problem on Mars 4
III. The Importance of Atmospheric Data to Photochemical Modeling 10
IV. Techniques for Observing Ozone on Mars 13
V. Goals 17
Chapter 2: Observations of Ozone on Mars and Data Reduction 19
I. The Infrared Heterodyne Spectrometers 19
II. Observing Campaigns 22
III. Data Acquisition and Reduction Schemes 23
Chapter 3: Modeling Earth's Atmospheric Transmittance and Ozone Profile 26
I. Ozone Profile Retrieval 26
II. Results and Comparison to Other Methods 30
III. Conclusions 33
Chapter 4: Modeling Martian Ozone and Thermal Profiles 35
Chapter 5: Ozone Abundances from Infrared Heterodyne Spectra of Mars 43
I. Atmospheric Contribution to Absorption Features 43
II. Seasonal and Solar Cycle Information 44
III. Retrievals of Ozone on Mars 46
IV. Spatial and Seasonal/Orbital Behavior of Ozone on Mars and the Anticorrelation of Total Ozone and Water Vapor Column Abundance 65
Chapter 6: Investigating the Altitude Distribution of Ozone on Mars Using Total Ozone Column Abundance and $O_2(^1\Delta)$ Dayglow Intensities 70
I. $O_2(^1\Delta)$ Dayglow Intensity and Ozone Abundance and Distribution 70
II. Retrievals of Ozone Altitude Distribution Using Heterodyne Ozone Retrievals and $O_2(^1\Delta)$ Dayglow Measurments 74
A. Investigating Ozone Altitude Distribution During Late Northern Spring 75
B. Investigating Ozone Altitude Distribution During Early Northern Summer 77
C. Investigating Ozone Altitude Distribution During Early Northern Winter 82
D. Solar Activity During Observations 82

III. Conclusions 83
Chapter 7: Infrared Heterodyne and Ultraviolet Ozone Measurements 86
I. Ultraviolet Spectroscopy of Ozone on Mars 86
II. Infrared Heterodyne and Ultraviolet Ozone Retrievals Compared 87
III. Discussion 95
Chapter 8: Using Observations of Ozone on Mars to Test Photochemical Models 98
I. Ozone and Photochemistry 98
II. Photochemical Models 99
III. Ozone as a Test of Photochemical Models 101
IV. The First Three-Dimensional Model 102
A. Total Ozone Column Abundance and Seasonal/Orbital Variability 102
B. Ozone Altitude Distribution 109
V. Correcting Photochemical Models 111
Chapter 9: Conclusions 114
I. Ozone, Photochemistry, and CO_2 Stability on Mars 114
II. Looking to the Future 119
Appendix 1: Significance of the Reflected Solar Spectrum 121
Appendix 2: Observational Details 123
Appendix 3: Analysis Details 132
References 135

List of Tables

Table 1.1. Properties of the terrestrial planets [Yung and DeMore 1999]. 1
Table 1.2. Atmospheric composition of Mars [Yung and DeMore 1999] 5
Table 2.1. Martian Ozone Heterodyne Data Sets..... 23
Table 2.2. $^{16}O^{12}C^{16}O$ laser local oscillator transitions used for observing ozone on Mars. 24
Table 3.1. Total ozone column density retrievals for Earth 32
Table 5.1. Seasonal coverage and sub-solar latitudes of observations of Mars ozone 45
Table 5.2. Total ozone column densities and 1σ uncertainties retrieved from infrared heterodyne spectra taken during 14-16 Feburary 1993 at Ls=40°. 50
Table 5.3. Total ozone column densities and 1σ uncertainties retrieved from infrared heterodyne spectra taken during 17-23 March 1995 at Ls=74°. 53
Table 5.4. Total ozone column densities and 1σ uncertainties retrieved from infrared heterodyne spectra taken during 4-7 July 1993 at Ls=102°..... 55
Table 5.5. Total ozone column densities and 1σ uncertainties retrieved from infrared heterodyne spectra taken during 24-29 March 1999 at Ls=115°. 58
Table 5.6. Total ozone column densities and 1σ uncertainties retrieved from infrared heterodyne spectra taken during 10-16 June 2003 at Ls=202°. 60
Table 5.7. Total ozone column densities and 1σ uncertainties retrieved from infrared heterodyne spectra taken during 3-6 June 1988 at Ls=208°. Retrieved column densities are ~30% smaller than those from the analysis of Espenak *et al.* [1991]. This is due to warmer temperatures retrieved through an updated analysis technique more extensive than was available at that time of the earlier analysis. 63
Table 6.1. Observations during late northern spring on Mars. 76
Table 6.2. Ozone altitude distribution results (late northern spring) 76
Table 6.3. Observations during early northern summer on Mars. 77
Table 6.4. Ozone altitude distribution results (early northern summer) 78
Table 6.5. Dayglow intensities from L_S=113° 79
Table 6.6. Observations during early northern summer on Mars. 81
Table 6.7. Ozone altitude distribution results (early northern summer) 81
Table 7.1. Hubble Space Telescope observations corresponding to those from this work. 89
Table A2.1. Observational Details of Infrared Heterodyne Martian Ozone Campaigns (June 1888, February & July 1993) 124-126
Table A2.2. Observational Details of Infrared Heterodyne Martian Ozone Campaigns (March 1995, March 1999) 127-129

Table A2.3. Observational Details of Infrared Heterodyne Martian Ozone Campaigns (June & March 2003) 130-131
Table A2.4. Mars Aspect Geometry Information 131
Table A3.1. February 1993 Analysis Details..... 132
Table A3.2. July 1993 Analysis Details 132
Table A3.3. June 1988 Analysis Details..... 133
Table A3.4. March 1995 Analysis Details..... 133
Table A3.5. March 1999 Analysis Details..... 134
Table A3.6. June 2003 Analysis Details..... 134

List of Figures

Figure 1.1. Seasons on Mars. The solar longitude, or L_S, is the position of Mars in its orbit around the sun. The northern spring equinox is at 0°, the northern summer solstice is at 90° and so on. The coincidence of aphelion and perihelion close to the solstices accentuates the seasons on Mars. Dates for data sets used in this work are displayed above their corresponding season. 3
Figure 1.2. Example reaction rates for odd hydrogen production (solid) and some reprocessing reactions (blue). Rates were calculated at 20 km altitude intervals from the atmospheric model and reaction coefficients of Nair *et al.* [1994], and water photolysis rates are taken from that work. 7
Figure 1.3. Example reaction rates for CO_2 destruction (red), CO_2 reformation (blue) and reactions important for recycling OH. Rates were calculated at 20 km altitude intervals from the atmospheric model and reaction coefficients of Nair *et al.* [1994], and CO_2 photolysis rates are taken from that work. 8
Figure 1.4. Example reaction rates for odd hydrogen destruction, showing relative importance at different altitudes. Rates were calculated at 20 km altitude intervals from the atmospheric model and reaction coefficients of Nair *et al.* [1994]. 9
Figure 1.5. Example reaction rates for ozone destruction, showing relative importance at different altitudes. Rates were calculated at 20 km altitude intervals from the atmospheric model and reaction coefficients of Nair *et al.* [1994]. 13
Figure 1.6. A non-comprehensive view of ozone (O_3), $O_2(^1\Delta)$ dayglow, and water vapor (H_2O) observations made since 1988. The upper axis displays Martian solar longitude corresponding to the terrestrial date on the lower axis. L_S=0° corresponds to the northern vernal equinox. Dotted lines separate Martian years. Abbreviations used refer to the following: 14
Figure 1.7. Telluric atmospheric transmittance between 10.2 and 8.9 μm (upper panel), and at 9.7 μm at heterodyne resolution (lower panel). Martian ozone features can be observed when Doppler shifted to regions of higher transmittance (arrow). 16
Figure 1.8. Example infrared heterodyne spectra from Espenak *et al.* 1991. 17
Figure 2.1. IRHS front-end optics at IRTF Coudé. 19
Figure 2.2. HIPWAC optics and support electronics at IRTF Cassegrain focus. 20
Figure 2.3. Schematic of infrared heterodyne system. In addition to the components mentioned in the text, a calibration cell containing a gas can be placed in the blackbody path and the absorption features of the gas can be measured for the purpose of calibration or laboratory spectroscopy. The flip mirror switches between

the optical paths to the source via the telescope and the blackbody calibrator. The dual CO_2 laser capability means that two lasers with different isotopic mixes can be available to provide a wider array of local oscillator frequencies, targeting multiple spectral regions of interest. OAP refers to an off-axis parabolic mirror.....21
Figure 2.4. Example heterodyne spectrum of Mars. The low resolution (25 MHz) filter bank samples both a deep CO_2 absorption feature (~1200 MHz) and ozone absorption features (~400 MHz). The ozone features are simultaneously sampled by the high resolution (5 MHz) filter bank (inset). 22
Figure 3.1. Example heterodyne double-sideband spectrum at 25 MHz spectral resolution against the Moon (histogram) showing individual absorption features that are matched by a radiative transfer model (solid line). Except for a weak CO_2 feature at 0 MHz, all structure is due to Earth's atmospheric ozone.....27
Figure 3.2. AFGL tropical (15°N) thermal and ozone mole fraction profiles. Contribution functions are shown for the center (uppermost profile) and wings (lower profiles, 200 MHz increments) for one of the target ozone absorption features, indicating that line wing contribution originates at altitudes below (i.e. pressures above) that of the line center. Contribution is calculated by multiplying the change in atmospheric transmittance with height by the Planck function at a particular frequency and altitude. This is an indication of the formation region of the modeled absorption feature at line center and along the wing at different frequencies (every 200 MHz) from line center. 28
Figure 3.3. The contour plot indicates how well radiative transfer models using different scalings of the thermal and ozone mole fraction profiles fit the spectrum at left. The "X" marks the best-fit parameters, which produce the model spectrum shown at left. 29
Figure 3.4. Ozone total column density retrievals. Bold indicates Dobson measurements (dates displayed). Other error bars indicate retrievals from radiative transfer analysis of heterodyne spectra using a scaled, unshifted AFLG ozone profile (solid), and a scaled profile shifted down 1 km in altitude (dotted).....30
Figure 3.5. Model ozone profiles and 1σ uncertainties retrieved from heterodyne spectra compared to available nearby lidar [McDermid *et al*. 1995] or ozonesonde [Johnson *et al*. 2002] profiles. The bold profiles indicate those chosen according to their consistency with Dobson column densities. Dotted profiles were rejected because their resulting column densities differed from the Dobson measurements. The error bar indicates the range of statistically acceptable (1σ) scaled ozone profiles. 31
Figure 4.1. Double sideband spectra of telluric transmittance against the Moon (left) and Martian and telluric transmittance against Mars (right). The shape of the right spectrum is that of the telluric transmittance at left along with Martian ozone absorption at ~400 MHz and Martian CO_2 absorption at ~1200 MHz.....35
Figure 4.2. Example thermal profile from Mars Global Surveyor [M. D. Smith *et al*. 2001, private communication] and constant-with-height ozone mole fraction profile. Dotted curves are initial profiles, solid curves are post-analysis profiles, and dot-dash curves represent 1σ uncertainties in a radiative transfer fit. They illustrate how the profiles are modified in the fitting process.....40

Figure 5.1. Example contribution functions. The upper panels show contribution to the line intensities (z-axis) as a function of frequency (x-axis) and height (y-axis). The large feature on the upper left panel is CO_2, while the smaller feature to its left is ozone, which is displayed on its own in the upper right panel. The lower panels show slices of the contribution functions at different frequencies. 44
Figure 5.2. Dates and L_S values for IR Heterodyne ozone observations of Mars are noted on this plot of monthly average International Sunspot Numbers compiled by the Sunspot Index Data Center in Belgium. 46
Figure 5.3. Martian observing geometry and heterodyne spectra (above) and observational coverage (below) from 14-16 February 1993, L_S=40°. 49
Figure 5.4. Total ozone column densities and 1σ uncertainties retrieved from 25 MHz (left) and 5 MHz (right) resolution infrared heterodyne spectra taken during 14-16 February 1993 at Ls=40°. Water vapor column densities from 9-11 March 1993 [Sprague *et al.* 1996, private communication] are shown as open diamonds. 50
Figure 5.5. Martian observing geometry and heterodyne spectra (above) and observational coverage (below) from 17-23 March 1995, L_S=74°. 51
Figure 5.6. Total ozone column densities and 1σ uncertainties retrieved from 25 MHz (top left) and 5 MHz (bottom left) resolution infrared heterodyne spectra taken during 17-23 March 1995 at Ls=74°. Water vapor column densities from 20 March 1995 [Sprague *et al.* 1996, private communication] are shown as open diamonds. Ozone column densities retrieved at 60°N are displayed as a function of local time from 25 MHz (top right) and 5 MHz (bottom right) resolution spectra. No significant variation in ozone column density is seen over the local times sampled (~4 hours). 52
Figure 5.7. Martian observing geometry and heterodyne spectra (above) and observational coverage (below) from 4-7 July 1993, L_S=102°. 54
Figure 5.8. Total ozone column densities and 1σ uncertainties retrieved from 25 MHz (left) and 5 MHz (right) resolution infrared heterodyne spectra taken during 4-7 July 1993 at Ls=102°. Water vapor column densities from 3 June 1993 [Sprague *et al.* 1996, private communication] are shown as open diamonds. The limited data do not allow the study of behavior with latitude. 55
Figure 5.9. Martian observing geometry and heterodyne spectra (above) and observational coverage (below) from 24-29 March 1999, L_S=115°. 56
Figure 5.10. Total ozone column densities and 1σ uncertainties retrieved from 25 MHz (top left) and 5 MHz (bottom left) resolution infrared heterodyne spectra taken during 24-29 March 1999 at Ls=115°. The dotted curve indicates contemporaneous measurement of total water vapor column density [MGS-TES, Smith *et al.* 2004, private communication]. Ozone column densities retrieved at 40°S are displayed as a function of local time from 25 MHz (top right) and 5 MHz (bottom right) resolution spectra. No significant variation in ozone column density can be reliably inferred from the local times sampled (~5 hours). 57
Figure 5.11. Martian observing geometry and heterodyne spectra (above) and observational coverage (below) from 10-16 June 2003, L_S=202°. 59

Figure 5.12. Total ozone column densities and 1σ uncertainties retrieved from 25 MHz (left) and 5 MHz (right) resolution infrared heterodyne spectra taken during 10-16 June 2003 at Ls=202°. The dotted curve indicates contemporaneous measurement of total water vapor column density [MGS-TES, Smith *et al.* 2004, private communication]. 60
Figure 5.13. Martian observing geometry and heterodyne spectra (above) and observational coverage (below) from 3-6 June 1988, L_S=208°. 61
Figure 5.14. Total ozone column densities and 1σ uncertainties retrieved from 25 MHz (left) and 5 MHz (right) resolution infrared heterodyne spectra taken during 3-6 June 1988 at Ls=208°. Water vapor column densities from 04 June 1988 [Rizk *et al.* 1991] are shown as open diamonds. Ozone column densities retrieved at 60°S are displayed as a function of local time from 25 MHz (top right) and 5 MHz (bottom right) resolution spectra. No significant variation in ozone column density can be reliably inferred from the local times sampled (~7 hours)..... 62
Figure 5.15. Martian observing geometry and heterodyne spectra (above) and observational coverage (below) from 1-3 November 2003, L_S=291°. Displayed spectra show contribution from both Earth and Mars, and only an upper limit retrieval for the ozone abundance was possible (~0.5 μm-atm). 64
Figure 5.16. No ozone was detected in the infrared heterodyne spectra taken at 20°N, 20°S, and 60°S during 1-2 November 2003 at Ls=291°. An upper limit of ~0.5 μm-atm was inferred from the noise level. The dotted curve indicates contemporaneous measurement of total water vapor column density [MGS-TES, Smith *et al.* 2004, private communication]. 65
Figure 5.17. Ozone abundances and 1σ uncertainties retrieved from 5 MHz resolution infrared heterodyne spectra are displayed for periods with sufficient spatial coverage for investigating anticorrelation with water vapor abundance. Water vapor column densities are from Sprague *et al.* [1996, private communication] (panels *a* and *b*), MGS-TES, Smith *et al.* [2004, private communication] (panels *c* and *d*), and Rizk *et al.* [1991] (panel *e*). The correlation coefficient, r, between the ozone and water vapor column densities is indicated, along with the percent probability that uncorrelated values could produce that particular r value. The correlation coefficients between the total column densities are consistently negative, indicating anticorrelation, but are not all close to -1, indicating the need to consider the distribution of species within the column. 66
Figure 5.18. Total ozone column densities from this work at the latitudes indicated, as a function of L_S. The curve indicates measurement of total water vapor column density [MGS-TES, Smith *et al.* 2004, private communication] for Mars Year 26, which ran from mid-2002 to early 2004. This period was chosen because it is the only complete year (L_S=0°-360°) measured by MGS-TES without a global dust storm. The correlation coefficient, r, between the ozone and water vapor column densities is indicated, along with the percent probability that uncorrelated values could produce that particular r value. The correlation coefficients between the total column densities are consistently negative, indicating anticorrelation, but are not

always close to -1, indicating the need to consider the distribution of species within the column. 68
Figure 6.1. Ozone profile (solid) for L_S=112° from Krasnopolsky [private communication]. Additional information on the model is given in the text. The overlay of the scaled total atmosphere number density profile (dashed) illustrates that ozone has a smaller scale height in this model (i.e. number density falls off at a faster rate than that of the rest of the atmosphere), except between 40 and 60 km where excess abundance appears. 80
Figure 6.2. Dates for IR Heterodyne ozone observations (dashed, L_S=upper row) and corresponding $O_2(^1\Delta)$ observations (dotted, L_S=lower row) are noted on this plot of monthly average International Sunspot Numbers compiled by the Sunspot Index Data Center in Belgium. 83
Figure 7.1. (following page) Ozone retrievals from infrared heterodyne spectroscopy (diamonds with 1σ uncertainties) compared to those from ultraviolet measurements made by the Hubble Space Telescope Faint Object Spectrograph [Clancy *et al.* 1996, 1999, R. T. Clancy, private communication]. The dates and orbital positions (L_S) of the UV measurements (open squares) are detailed in Table 7.1. (In panel *a,* large squares are from the same year as this work, and small squares are from a different year, and the UV measurements were earlier than IR measurements by ~10° in L_S.) The error bars on the UV measurements represent the uncertainty in the accuracy as quoted in Clancy *et al.* [1999], which was +50%, -20%. The error bars on the infrared heterodyne measurements reflect the uncertainty in the accuracy and were calculated for each individual measurement. 89
Figure 7.2. Dates for IR Heterodyne ozone observations (dashed, L_S=upper row) and UV ozone observations (dotted, L_S=lower row) are noted on this plot of monthly average International Sunspot Numbers compiled by the Sunspot Index Data Center in Belgium. 95
Figure 8.1. (following page) Ozone column abundances and 1σ uncertainties from this work are displayed with corresponding slices from the three-dimensional photochemical model of Lefèvre *et al*. [2004]. The longitudes and local times of the model curves are indicated on the plots by color-coded text, and are close to those of the observations. Color also indicates the correspondence between observed and modeled ozone column densities. Numbers displayed with data points indicate day of month of observation. The general behavior of ozone column abundance with L_S seen in the data is reproduced by the model, but there is significant quantitative departure of the model from the observed values at lower latitudes during aphelion periods. Better agreement overall is seen during perihelion periods. (Aphelion is at L_S=71° and perihelion is at L_S=251°.) The large ozone abundances modeled in the polar regions occur during their respective winters when those latitudes are not visible from Earth. 104
Figure 8.2. Ozone column abundances and 1σ uncertainties from this work are displayed as a function of L_S with model abundances from the three-dimensional photochemical model of Lefèvre *et al.* [2004] (0° longitude, 12:00 local time). Aphelion is at L_S=71° and perihelion is at L_S=251°. Excellent agreement is seen for

the most part in the seasonal behavior at 60°N, and during perihelion seasons at lower latitudes, but the model consistently underestimates ozone at low latitude during aphelion seasons. 106
Figure A1.1. Geometry for determining intensity of the solar spectrum reflected from the Moon 121

List of Abbreviations

μm-atm	Column density unit micron-atmosphere, or 2.69×10^{15} molecules cm^{-2}. This unit describes the amount of a gaseous constituent as an equivalent thickness in microns at standard temperature and pressure.
AU	Astronomical Unit. The distance from the Earth to the Sun.
D. U.	Column density unit Dobson Unit, or 2.69×10^{16} molecules cm^{-2}.
FOV	Field-of-view
HIPWAC	Goddard Heterodyne Instrument for Planetary Wind and Composition
IR	Infrared
IRHS	Goddard Infrared Heterodyne Spectrometer
L_S	Solar longitude, or angular position of Mars in its orbit about the Sun. The northern spring equinox is 0°, northern summer solstice is 90°, and so on.
MR	MegaRayleigh, or $10^{12}/4\pi$ photons cm^{-2} s^{-1} $ster^{-1}$
pr. μm	Column density unit precipitable micron, or 3.36×10^{18} molecules cm^{-2}. This unit describes the equivalent depth in microns of water vapor as a precipitate.
UV	Ultraviolet

Chapter 1: Introduction

I. Mars

The planet Mars has gone from being the subject of mystery in antiquity to the target of spacecraft at every launch opportunity in recent years. It is one of the more accessible planets via Earth-based and in situ observations. Along with Venus, Mars is considered important for understanding properties of terrestrial planets in general and even for understanding properties and processes that shape conditions on Earth. On its own, Mars is a unique geological and atmospheric environment, raising more questions with each new discovery.

Table 1.1. Properties of the terrestrial planets [Yung and DeMore 1999].

	Mars	Earth	Venus
Surface Pressure	6.9 mbar	1000 mbar	93,000 mbar
Surface Temperature	210 K	297 K	737 K
Radius	3393 km	6378 km	6052 km
Major Atmospheric Constituents	95% CO_2 3% N_2	78% N_2 21% O_2	96% CO_2 3% N_2
Solar Day	24 hr 40 m	24 hr	243 days
Year	687 days	365 days	225 days
Orbital Eccentricity	0.093	0.017	0.0068
Heliocentric Distance	1.52 AU	1 AU	0.72 AU

Various properties of the terrestrial planets are presented in Table 1.1. The length of the day on Mars is just slightly longer than the Earth, which would make adjusting to Mars easier for future explorers, but the low atmospheric pressure and greater heliocentric distance lead to bitterly cold temperatures. Although Venus and Earth are very similar in size, their environments differ drastically. The major atmospheric constituents of Mars and Venus and their proportions are practically identical, but their

atmospheric pressures differ by over 4 orders of magnitude. Even though the differences among the terrestrial planets appear to outweigh the similarities, the same physical laws apply to all of them, and therefore an understanding of a process on one can be a key to understanding another.

The atmosphere of Mars is very thin relative to Earth, with an average surface pressure of ~6 mbar, which is less than 1% that of Earth. To the geologist, the atmosphere is a thin veil that interferes with observations of the rocks that hold keys to the history of the planet (tongue in cheek, of course). To the atmospheric scientist, the atmosphere is a laboratory rich in chemical and dynamical processes. Where the atmosphere meets the rocks, chemistry and weather make it important to consider one when studying the other.

Atmospheric conditions on Mars vary over the course of the year. Mars has an eccentric orbit compared to that of Earth and Venus, which results in ~45% greater solar flux at perihelion than at aphelion. In addition, perihelion and aphelion occur near the solstices (Fig. 1.1), accentuating seasonal variations (e.g. longer southern winter). Atmospheric pressure changes by ~20% over the course of the year due to changing temperatures that result in sublimation of CO_2 from the polar caps and later refreezing. The existence of southern highlands and northern lowlands results in a range of atmospheric pressures with latitude. Water vapor sublimates mainly from the north polar cap during warmer periods and freezes out of the atmosphere during colder periods.

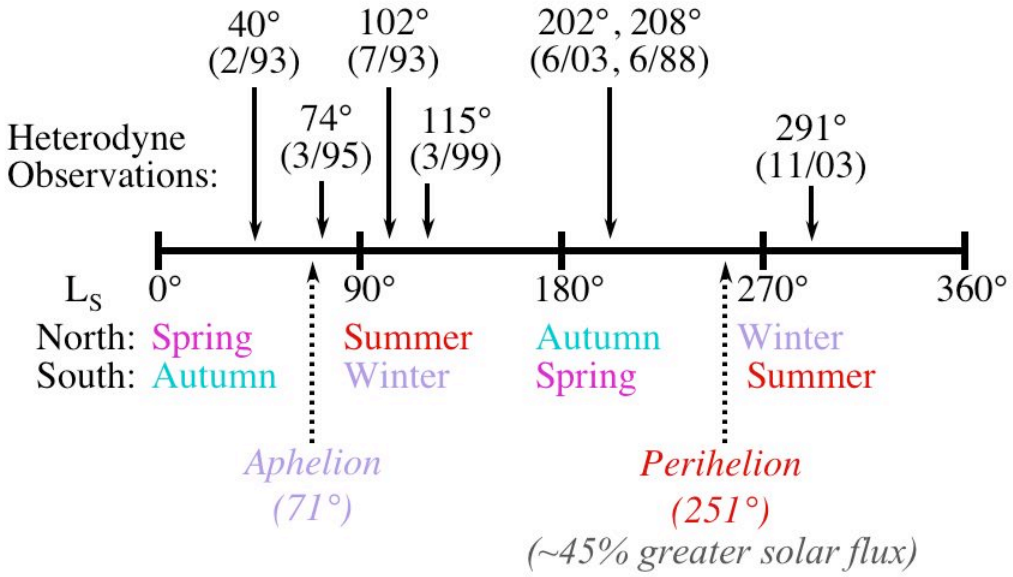


Figure 1.1. Seasons on Mars. The solar longitude, or L_S, is the position of Mars in its orbit around the sun. The northern spring equinox is at 0°, the northern summer solstice is at 90° and so on. The coincidence of aphelion and perihelion close to the solstices accentuates the seasons on Mars. Dates for data sets used in this work are displayed above their corresponding season.

Computational models have been developed that simulate the environment of Mars, and as the computational ability of computers has increased, so has the complexity of the models. Observations of actual conditions on Mars are extremely important for testing models and for identifying and improving potentially correct models. A model may be able to reproduce a particular set of observed conditions, but the richer and more varied the available data, the greater the burden the model must bear to reproduce those conditions.

Observations of ozone will be presented as important for testing models that seek to simulate the photochemistry of the atmosphere of Mars and address the issue of the persistent, abundant CO_2 (carbon dioxide) atmosphere. The technique adopted in this work for observing Martian ozone and extracting abundances will be discussed.

Comparisons will be made to other methods of observing ozone. Different methods for probing ozone abundance will be combined to investigate altitude distribution. Measured orbital/seasonal (Fig. 1.1) and spatial variability of ozone abundance and distribution will be used to test predictions of photochemical models and investigate the current understanding of CO_2 stability on Mars. Ozone height profiles for Earth retrieved from calibration measurements will also be presented.

II. The CO_2 Stability Problem on Mars

The atmosphere of Mars is composed almost entirely of CO_2. It came as a surprise when CO_2 was found to be the major atmospheric constituent, because solar ultraviolet radiation dissociates CO_2 and it does not easily reform on its own. Although the atmospheric pressure is <1% that of Earth, this seemingly simple atmosphere has proved to be complex, and over the years a general picture of the photochemical processes taking place in the atmosphere has emerged [cf. Yung and DeMore 1999, Atreya and Gu 1995, Krasnopolsky 1986].

Carbon dioxide in the Martian atmosphere is dissociated by solar ultraviolet radiation ≤205 nm:

$$CO_2 + h\nu \rightarrow CO + O \tag{1.1}$$

The direct recombination reaction is achieved through the extremely slow, spin-forbidden, three-body reaction:

$$CO + O + M \rightarrow CO_2 + M \tag{1.2}$$

Here, M is any background gas molecule, which for the case of Mars is predominantly CO_2. The three-body reaction that combines atomic O to form O_2 is orders of magnitude faster than Eq. 1.2. Even with the subsequent photolysis of O_2, a buildup of CO and O_2 would be expected up to certain equilibrium values, with a ratio of CO to O_2 of 2:1 resulting from the net reaction:

$$2CO_2 \rightarrow 2CO + O_2 \tag{1.3}$$

Measurements of Martian CO and O_2 reveal abundances that are far lower than those expected from this pure CO_2 scheme. In addition, the ratio of CO to O_2 is found to be 1:2 rather than the expected 2:1 (Table 1.2). Solving the CO_2 stability problem involves discovering how the reformation of CO_2 on Mars is taking place at a rate much faster than expected.

Table 1.2. Atmospheric composition of Mars [Yung and DeMore 1999]

CO_2	95%	H_2O	~0.03%
N_2	2.7%	Ne	2.5 ppm
Ar	1.6%	Kr	0.3 ppm
O_2	0.13%	Xe	0.08 ppm
CO	0.07%	O_3	~0.03 ppm

A major key to the problem was put forth by Parkinson and Hunten [1972] and by McElroy and Donahue [1972], who recognized that the very small abundance of water vapor in the Martian atmosphere could be important to the CO_2 reformation process. Water is dissociated through photolysis ($\leq$243 nm):

$$H_2O + h\nu \rightarrow OH + H \tag{1.4}$$

Water is also dissociated by excited metastable atomic oxygen:

$$H_2O + O(^1D) \rightarrow 2OH \tag{1.5}$$

Saturation levels for water vapor vary from ~10-15 km at aphelion to ~30 km at perihelion [Smith 2002] and the main source of $O(^1D)$ at those altitudes is ozone photolysis. Sources of $O(^1D)$ at other altitudes are O_2 photolysis above ~60 km and CO_2 photolysis above ~80 km, where $O(^1D)$-producing photolyzing radiation can penetrate [e.g. Nair *et al.* 1994].

Species with one hydrogen atom such as H, OH, and HO_2 are referred to as "odd hydrogen" or "HO_x" and are very reactive. Hydrogen peroxide (H_2O_2) is also grouped with odd hydrogen because of its reactivity. The hydroxyl molecule OH plays the key role in a catalytic CO_2 reformation process. In addition to Eqs. 1.4 and 1.5, odd hydrogen is produced through reactions of excited metastable oxygen atoms with molecular hydrogen:

$$H_2 + O(^1D) \rightarrow H + OH \tag{1.6}$$

Atomic hydrogen provided in Eqs. 1.4 and 1.6 goes on to react with oxygen and ozone ultimately resulting from the destruction of CO_2 in (1.1) to eventually produce more OH through pathways such as:

$$H + O_2 + M \rightarrow HO_2 + M \tag{1.7}$$
$$HO_2 + O \rightarrow O_2 + OH \tag{1.8}$$

$$H + O_2 + M \rightarrow HO_2 + M \tag{1.7}$$
$$HO_2 + HO_2 \rightarrow H_2O_2 + O_2 \tag{1.9}$$
$$H_2O_2 + h\nu \rightarrow 2OH \tag{1.10}$$

$$H + O_2 + M \rightarrow HO_2 + M \tag{1.7}$$
$$HO_2 + h\nu \rightarrow OH + O \tag{1.11}$$

$$H + O_3 \rightarrow OH + O_2 \tag{1.12}$$

Although water vapor photolysis is ultimately responsible for OH production, it is not itself the fastest direct producer of OH. Examples of reaction rates for odd hydrogen production (Eqs. 1.4-1.6) as well as some reprocessing reactions are shown in Fig. 1.2.

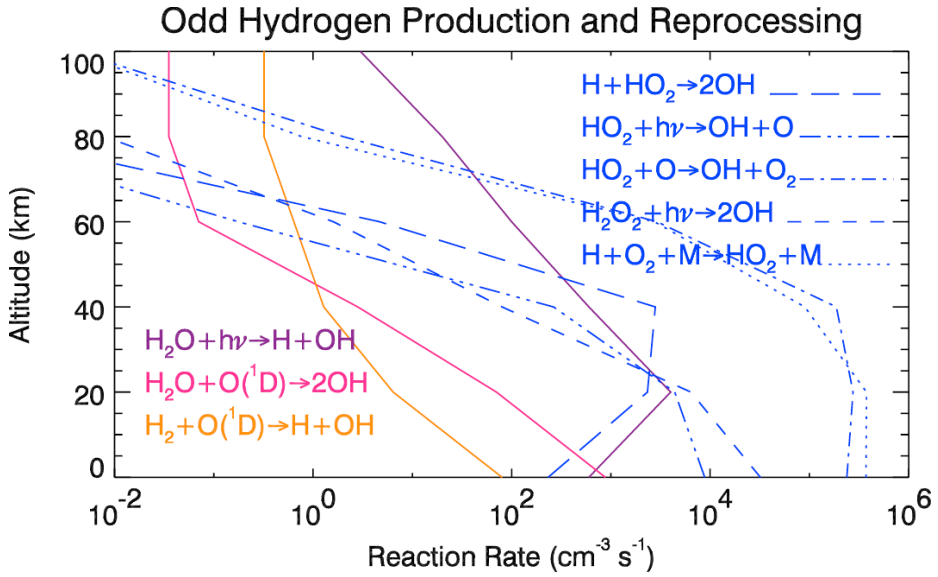


Figure 1.2. Example reaction rates for odd hydrogen production (solid) and some reprocessing reactions (blue). Rates were calculated at 20 km altitude intervals from the atmospheric model and reaction coefficients of Nair *et al.* [1994], and water photolysis rates are taken from that work.

The OH produced in the reactions above can go on to react with CO to form CO_2 at a rate that is orders of magnitude faster than the three-body recombination reaction in Eq. 1.2 (Fig. 1.3). The process involving OH is catalytic because additional reactions recycle it, and therefore the minute amount of water vapor present on Mars (~0.02%) is sufficient to support this process. One such scheme involving O_2 in OH recycling is:

$$\begin{aligned} &CO + OH \rightarrow CO_2 + H && (1.13)\\ &H + O_2 + M \rightarrow HO_2 + M && (1.7)\\ &O + HO_2 \rightarrow O_2 + OH && (1.9)\\ &\overline{CO + O \rightarrow CO_2\ (\textit{net reaction})} && (1.14) \end{aligned}$$

Another scheme involving O_3 in the recycling of OH is:

$$\begin{aligned} &CO + OH \rightarrow CO_2 + H && (1.13)\\ &H + O_3 \rightarrow OH + O_2 && (1.12)\\ &O + O_2 + M \rightarrow O_3 + M && (1.15)\\ \hline &CO + O \rightarrow CO_2 \ (net\ reaction) && (1.14) \end{aligned}$$

During warmer periods when water vapor is more abundant, an important CO_2 recycling scheme is:

$$\begin{aligned} &2(CO + OH \rightarrow CO_2 + H) && (1.13)\\ &2(H + O_2 + M \rightarrow HO_2 + M) && (1.7)\\ &HO_2 + HO_2 \rightarrow H_2O_2 + O_2 && (1.11)\\ &H_2O_2 + h\nu \rightarrow 2OH && (1.10)\\ \hline &2CO + O_2 \rightarrow 2CO_2 \ (net\ reaction) && (1.16) \end{aligned}$$

Example rates of these reactions are presented is Fig. 1.3.

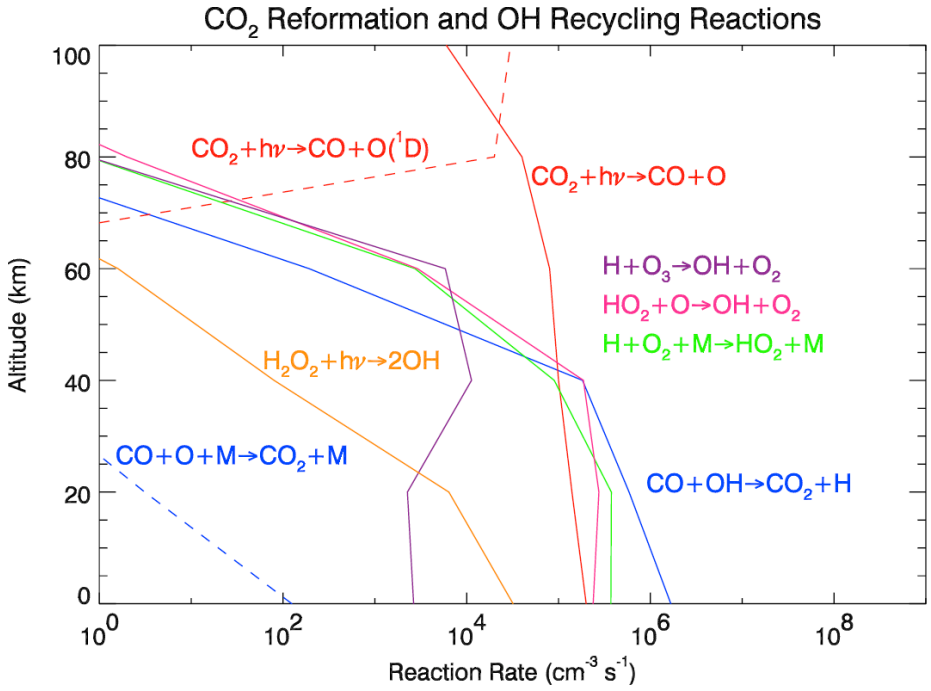


Figure 1.3. Example reaction rates for CO_2 destruction (red), CO_2 reformation (blue) and reactions important for recycling OH. Rates were calculated at 20 km altitude intervals from the atmospheric model and reaction coefficients of Nair *et al.* [1994], and CO_2 photolysis rates are taken from that work.

The sinks for odd hydrogen include:

$$H + HO_2 \rightarrow H_2 + O_2 \quad (1.17)$$

$$H + HO_2 \rightarrow H_2O + O \quad (1.18)$$

$$HO_2 + OH \rightarrow H_2O + O_2 \quad (1.19)$$

Example loss rates for odd hydrogen are given in Fig. 1.4. Odd hydrogen can also be lost onto surfaces of dust and ice particles through heterogeneous processes. Because there are not many chemical sinks for odd hydrogen, a small amount of it (or its photochemical parent, water vapor) can be very effective in sustaining the CO_2 atmosphere of Mars.

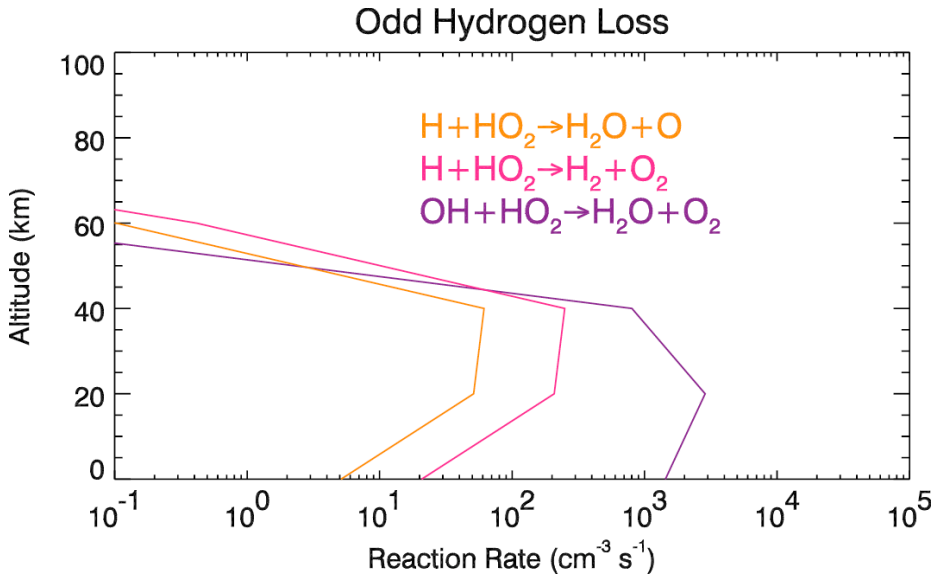


Figure 1.4. Example reaction rates for odd hydrogen destruction, showing relative importance at different altitudes. Rates were calculated at 20 km altitude intervals from the atmospheric model and reaction coefficients of Nair *et al.* [1994].

The photochemistry described is thought to be largely responsible for recycling and stabilizing CO_2 in the atmosphere, but there are other processes that increase the complexity. Molecular nitrogen can be dissociated and processed in the ionosphere

(above ~120 km), resulting in "odd nitrogen" species like NO, some of which can be transported to the lower atmosphere and participate in catalytic recycling of OH. The reaction rates are lower than the recycling schemes presented earlier (by ~5× at the surface and by increasing orders of magnitude with altitude [Nair *et al.* 1994]). Ionospheric processes result in hydrogen escape from H_2 dissociation and oxygen escape from exothermic ion chemistry. In the lower atmosphere, heterogeneous chemistry can play a role in processes such as odd hydrogen loss. The extreme seasons and topography of Mars, along with atmospheric circulation, also come into play. Photochemical modelers must consider these aspects, as well the limitations of the laboratory data they employ, when attempting to reproduce the chemistry responsible for CO_2 stability, observed atmospheric constituent abundances, and atmospheric conditions.

III. The Importance of Atmospheric Data to Photochemical Modeling

The discovery of the importance of water vapor photolysis and the subsequent odd hydrogen reactions that catalytically reform CO_2 provided an elegant general solution to the CO_2 stability problem, but the specifics are not entirely understood. There are many published photochemical models [e.g. Krasnopolsky *et al.* 1993, 1995, Nair *et al.* 1994, Clancy and Nair 1996, Lefèvre *et al.* 2004]. Earth-based and spacecraft measurements of atmospheric constituents provide the inputs for photochemical modeling and the abundances with which to compare the outputs of those models.

Until the onslaught of spacecraft missions that began with the launch of Mars Global Surveyor in 1996, much of the modeling has had to rely largely on measurements made by Mariner 7 (1969), Mariner 9 (1971-1972), and the Viking 1 and 2 landers and

orbiters (1976-1980). Other atmospheric results were obtained through the short-lived Mars 5 (1974) and Phobos 2 (1989) missions, and through ongoing ground-based campaigns. For instance, water vapor on Mars has been monitored from the Earth around opposition for many years [e.g. Rizk *et al.* 1991, Sprague *et al.* 1996, 2001, E. Barker, private communication]. Because of limited measurements, there has been a necessary tendency for modelers to utilize measurements of different constituents from different seasons and orbital periods (L_S), or from the same orbital period in different years. However, as with Earth, the seasonal patterns on Mars are varied and the need for simultaneous measurements of different constituents, as well as long term monitoring, is important for refining photochemical models.

With recent successful missions to Mars, the possibility of continuous monitoring is being realized. Mars Global Surveyor has been continuously monitoring global water vapor abundance, atmospheric temperature, and dust and haze opacity since March 1999 [e.g. M. D. Smith *et al.* 2001, M. D. Smith 2002, 2004]. Mars Express is the first spacecraft to monitor ozone since Mariner 9 [Bertaux *et al.* 2000, 2004], and will simultaneously study ozone and water abundance and distribution. Spacecraft have limited instrumentation and lifetimes, however, and the goal is not always the atmosphere, so monitoring of atmospheric constituents must be done from Earth as well.

Chemistry resulting from water vapor photolysis appears to hold the key to the so-called CO_2 stability problem. Except for recent detections of H_2O_2 [Clancy *et al.* 2004, Encrenaz *et al.* 2004], the odd hydrogen (H, OH, HO_2) that can participate in reforming CO_2 has not been observed. Ozone (O_3) is destroyed by odd hydrogen and is therefore a sensitive tracer of the photochemistry that stabilizes the CO_2 atmosphere of Mars.

Ozone is formed by the three-body reaction:

$$O + O_2 + M \rightarrow O_3 + M \quad (1.15)$$

The M is predominantly CO_2, and so ozone production is therefore sensitive to the CO_2 density, which varies with the orbit (L_S) and with the altitude of the landscape. Production is also controlled by the rate of CO_2 photolysis that provides O and ultimately O_2 (from three body reactions of O). Ozone is dissociated by solar ultraviolet radiation:

$$O_3 + h\nu \rightarrow O_2 + O(^1D) \quad (1.20)$$

Ozone and atomic oxygen are expected to interconvert during the day, therefore photolysis and other reactions that result in atomic oxygen are not considered a permanent ozone loss mechanism. Ozone is destroyed by odd hydrogen through:

$$H + O_3 \rightarrow OH + O_2. \quad (1.11)$$

$$OH + O_3 \rightarrow HO_2 + O_2 \quad (1.21)$$

$$HO_2 + O_3 \rightarrow OH + 2O_2 \quad (1.22)$$

Example ozone loss rates due to these reactions are displayed in Fig. 1.5. The reaction rate of Eq. 1.11 dominates that of Eqs. 1.21 and 1.22 by about an order of magnitude at the surface, and the three show that ozone abundance should be sensitive to odd hydrogen abundance, and therefore a good tracer of those constituents. It is expected that ozone destruction should be controlled by the abundance of the odd hydrogen photochemical parent, water. This ozone/water anticorrelation was first observed by the Mariner 9 spacecraft, which saw northern hemispheric ozone abundances rise as winter progressed and water vapor froze out of the atmosphere, as well as a similar effect in the southern hemisphere during its winter [Lane *et al.* 1973]. Additional measurements of ozone and water at the same time are important for constraining photochemical models

that predict this ozone/water anticorrelation and for understanding the behavior of the atmosphere with orbital position.

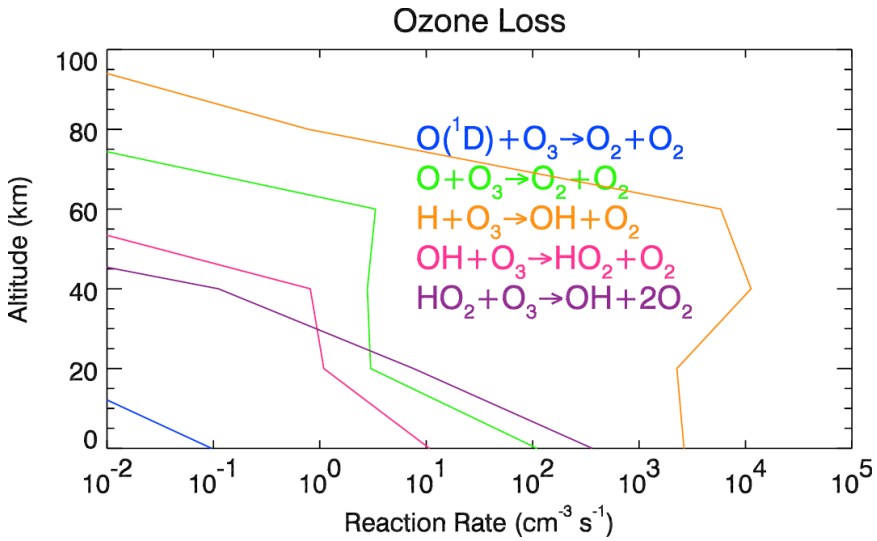


Figure 1.5. Example reaction rates for ozone destruction, showing relative importance at different altitudes. Rates were calculated at 20 km altitude intervals from the atmospheric model and reaction coefficients of Nair *et al.* [1994].

IV. Techniques for Observing Ozone on Mars

Ozone was first measured on Mars by Mariner 7 [Barth and Hord 1971] and Mariner 9 [Lane *et al.* 1973, Barth *et al*. 1973, Wehrbein *et al*.1979]. Ultraviolet (UV) absorption spectra of the Hartley bands (200-330 nm) were used to retrieve ozone abundances. The UV reflectance spectroscopy technique involves assumptions about the scattering properties of the atmosphere and ozone distribution, and may include some contribution from ozone adsorbed on surfaces. Lindner [1995], in reference to the Mariner 9 data, emphasized that the uncertainties in the scattering properties of clouds and dust may result in significant uncertainties (factor of 3) for retrieved ozone abundances. In recent years, Hubble Space Telescope UV observations using the Faint Object Spectrograph (HST-FOS) have been made [Clancy *et al*. 1996, 1999]. Mars

Express has recently begun observing ozone in the UV from orbit for the first time since Mariner 9 [Bertaux *et al.* 2000, 2004].

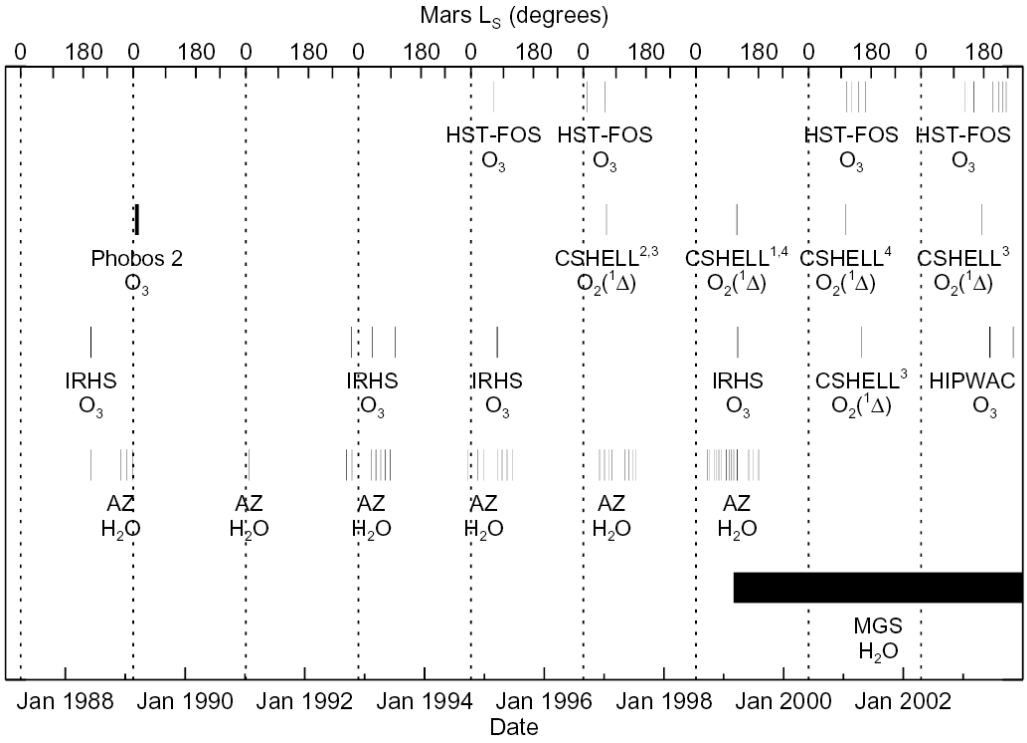


Figure 1.6. A non-comprehensive view of ozone (O_3), $O_2(^1\Delta)$ dayglow, and water vapor (H_2O) observations made since 1988. The upper axis displays Martian solar longitude corresponding to the terrestrial date on the lower axis. L_S=0° corresponds to the northern vernal equinox. Dotted lines separate Martian years. Abbreviations used refer to the following:

IRHS and HIPWAC: Infrared heterodyne observations for this project.
AZ: University of Arizona observations [Rizk *et al.* 1991, Sprague *et al.* 1996, 2001, private communication].
HST-FOS: Hubble Space Telescope Faint Object Spectrograph [Clancey *et al.* 1996, 1999, private communication].
CSHELL: $O_2(^1\Delta)$ dayglow observations [1:Krasnopolsky and Bjoraker 2000. 2:Novak et al. 2002, 3: Krasnopolsky 2003*a*, 4: R. E. Novak, private communcation].
MGS: Mars Global Surveyor spacecraft [Smith *et al.* 2002].
Phobos 2: Solar occultations with Phobos 2 spacecraft [Blamont and Chassefiére 1993]

A second, indirect, method of ozone retrieval involves measuring the intensity of the $O_2(^1\Delta)$ 1.27 μm dayglow emission on Mars and inferring the ozone abundance from

that dayglow intensity [e.g. Noxon *et al.* 1976, Krasnopolsky and Bjoraker 2000, Novak *et al*. 2002, Krasnopolsky 2003*a*]. The photolysis of ozone leads to the production of molecular oxygen in the metastable state of $^1\Delta$ that is rotationally excited. Collisional quenching dominates in the lower atmosphere, but at altitudes above ~20 km, the excited oxygen state has a higher probability of decaying radiatively and producing the dayglow emission. The emission is therefore a tracer of ozone abundance. Dayglow intensities can be compared to those predicted by photochemical models. They can also be converted to ozone column abundances, but assumptions must be made about the quenching rate and ozone distribution, and the lower boundary of the retrieved column is not well defined.

A third method, infrared heterodyne spectroscopy, is the only way to directly measure Martian ozone lines from the surface of the Earth. This is the technique that is used for the ozone measurements for this project, and it is described in detail in Ch. 2. Infrared heterodyne spectroscopy can achieve the very high resolution of $\lambda/\Delta\lambda \sim 10^6$, which is orders of magnitude greater than that of most infrared spectrometers. The spectral region between 9 and 10 μm is rich in potential Martian ozone target absorption lines, but their telluric counterparts overwhelm them. The very high resolution provided by infrared heterodyne spectroscopy allows the opportunity to observe Martain ozone features when they are Doppler shifted away from their telluric counterparts into regions of higher atmospheric transmittance. This is illustrated in Fig. 1.7, where the upper panel shows the Earth's atmospheric transmittance between 10.2 and 8.9 μm. Ozone is responsible for most of the features. The lower panel approximates the bandpass of an infrared heterodyne spectrometer at 9.7 μm, resolving the individual terrestrial ozone

absorption features and exposing regions of higher transmittance (arrow). The changing relative velocity between Earth and Mars allows opportunities for Martian ozone lines to be Doppler shifted to those regions and to be observable from the surface of the Earth.

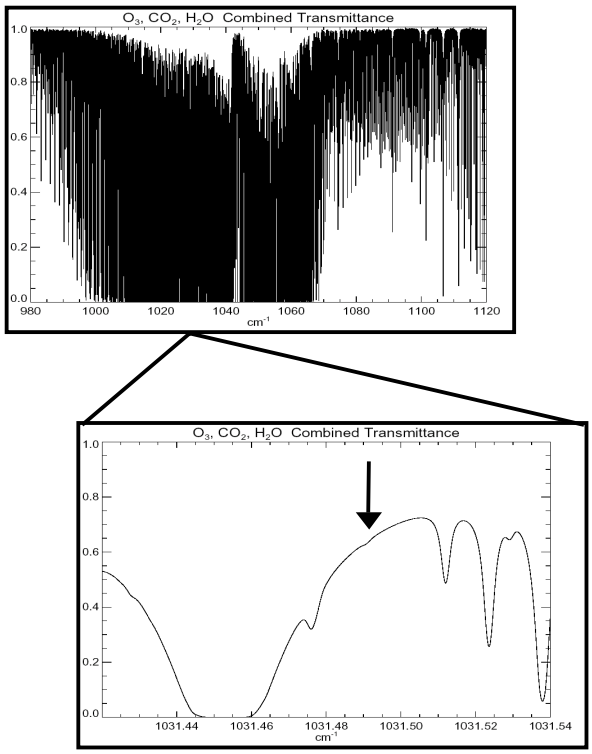


Figure 1.7. Telluric atmospheric transmittance between 10.2 and 8.9 μm (upper panel), and at 9.7 μm at heterodyne resolution (lower panel). Martian ozone features can be observed when Doppler shifted to regions of higher transmittance (arrow).

Infrared (IR) heterodyne spectra of Mars in the 9.7 μm region at the very high resolution of $\lambda/\Delta\lambda \sim 10^6$ contain fully-resolved individual lines of gaseous ozone, as well as CO_2 lines in the very same spectra that can be used to model thermal profiles (e.g. Fig 1.8). This allows for the measurement of temperature and ozone abundance at the same time and location, which is important for obtaining accurate ozone abundances. Heterodyne spectroscopy of ozone has been identified as important for the study of Martian photochemistry [Krasnopolsky 1993*a*]. In addition to providing their own ozone

abundances for comparing with photochemical models (Ch. 8), heterodyne retrievals can also be used to test and compare with retrievals made with UV reflectance spectroscopy (Ch. 7) and to investigate ozone height distribution when combined with $O_2(^1\Delta)$ dayglow measurements (Ch. 6).

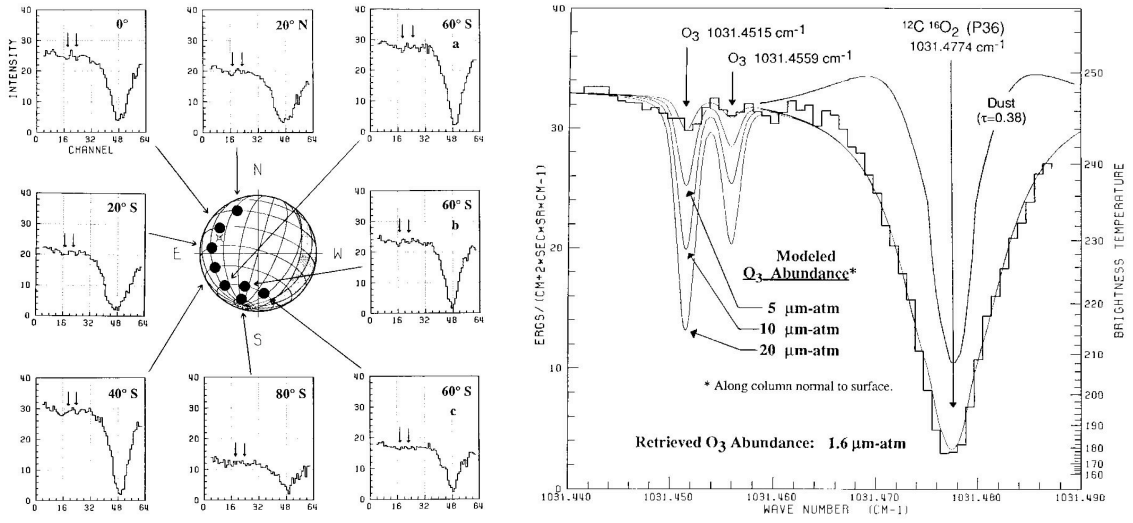


Figure 1.8. Example infrared heterodyne spectra from Espenak *et al.* 1991.

V. Goals

The infrared heterodyne technique was first applied to ozone on Mars in June of 1988 by Espenak *et al.* [1991] and an example of those results appears in Fig. 1.8. Four additional data sets were acquired between 1993 and 1999, but remained unanalyzed until this work. Two additional data sets were acquired in 2003 as part of this work. The main goal of this work is to improve the understanding of the photochemistry and CO_2 stability of the atmosphere of Mars.

Specific technical and scientific goals of this work are as follows:

- Develop and implement a technique for performing radiative transfer analysis on all heterodyne data sets and retrieving ozone abundances.

- Employ contemporaneous water vapor measurements and look for any anticorrelation between ozone and water vapor abundance.
- Compare heterodyne ozone abundances to those obtained using ultraviolet techniques and investigate differences.
- Investigate the height distribution of ozone by combining heterodyne ozone abundances with $O_2(^1\Delta)$ dayglow intensities.
- Test the understanding of CO_2 stability by comparing photochemical model predictions with measurements of orbital/seasonal and spatial distribution of ozone and explore possible sources of disagreement.

Chapter 2: Observations of Ozone on Mars and Data Reduction

I. The Infrared Heterodyne Spectrometers

The data used in this project were acquired with the NASA/Goddard Infrared Heterodyne Spectrometer (IRHS, Fig. 2.1) and the Heterodyne Instrument for Planetary Wind and Composition (HIPWAC, Fig. 2.2) at the NASA Infrared Telescope Facility (IRTF) on Mauna Kea, Hawai'i. The IRHS instrument resided at the Coudé focus of IRTF until succeeded by the Cassegrain instrument HIPWAC in January of 2000.

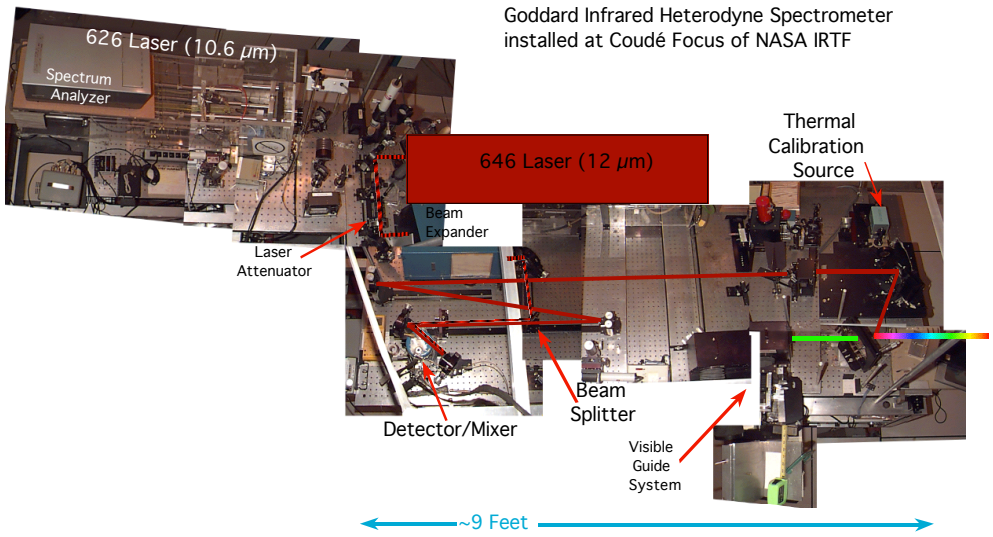


Figure 2.1. IRHS front-end optics at IRTF Coudé.

IRHS and HIPWAC utilize similar techniques. Source light from the telescope is directed into the instrument front-end. A dichroic lens allows visible light to pass through to a camera used for active tracking on the source while reflecting the infrared light further into the instrument. Optical components match both the source beam and an infrared CO_2 laser local oscillator (LO) beam and focus them onto a liquid nitrogen-cooled HgCdTe photomixer (Fig. 2.3). The signal is chopped with an in-system ("on-the-

table") chopper or the telescope's wobbling secondary mirror to provide synchronous detection of the difference (beat) frequency between the source and laser frequencies. The frequency and intensity information of the infrared spectrum are preserved in the resulting beat frequency spectrum, which is in the radio regime. A local blackbody source provides the system intensity calibration, which was compared with direct lunar measurement. The accuracy of the measured intensities is ≤3K.

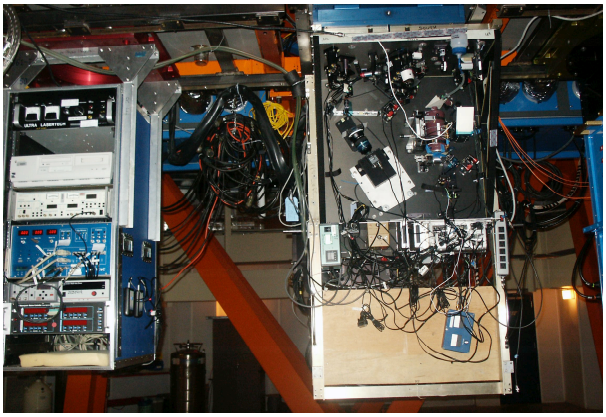


Figure 2.2. HIPWAC optics and support electronics at IRTF Cassegrain focus.

Both IRHS and HIPWAC utilized a back-end of two RF filter banks to analyze the resulting beat frequency signal. The low-resolution (LR) filter bank contains 64 filters that are 25 MHz (0.00083 cm^{-1}) in width, providing 3200 MHz of frequency range folded about the laser LO into a 1600 MHz double-sideband spectrum. The high-resolution (HR) filter bank contains 64 filters that are 5 MHz (.000166 cm^{-1}) in width. The beat frequency band is measured in the HR filter bank by using the output of a radio frequency local oscillator (RFLO) to adjust the frequency positioning of the filter bank's 320 MHz bandpass. The combination of both filter banks allows for simultaneous sampling of both the wide LR bandpass, which includes both ozone and CO_2 (for

temperature retrieval) and 5 MHz sampling of the HR filter bank across the ozone features themselves for better ozone mole fraction retrieval (Fig. 2.4). In one instance, an acousto-optic spectrometer (AOS) with a bandwidth of 1500 MHz and a spectral resolution of 1 MHz was used along with the filter banks to analyze the heterodyne signal. The output of the three radio frequency spectrometers is digitized and stored on computers capable of further analysis and display. Further discussion of the infrared heterodyne technique is given by Kostiuk [1994] and by Kostiuk and Mumma [1983].

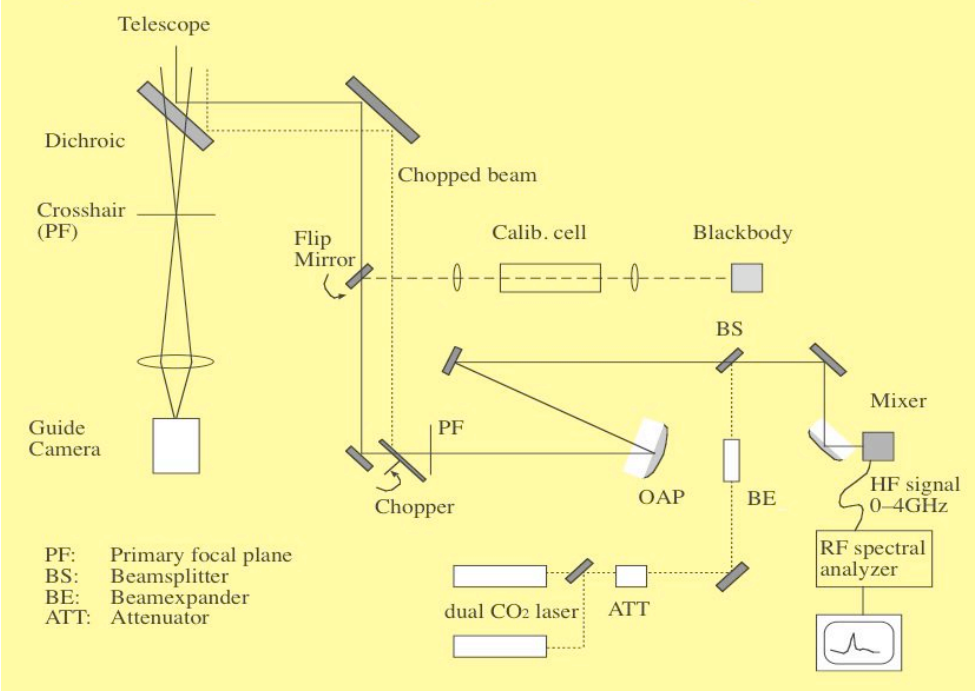


Figure 2.3. Schematic of infrared heterodyne system. In addition to the components mentioned in the text, a calibration cell containing a gas can be placed in the blackbody path and the absorption features of the gas can be measured for the purpose of calibration or laboratory spectroscopy. The flip mirror switches between the optical paths to the source via the telescope and the blackbody calibrator. The dual CO_2 laser capability means that two lasers with different isotopic mixes can be available to provide a wider array of local oscillator frequencies, targeting multiple spectral regions of interest. OAP refers to an off-axis parabolic mirror.

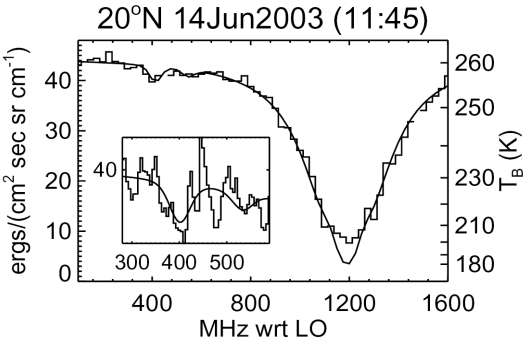


Figure 2.4. Example heterodyne spectrum of Mars. The low resolution (25 MHz) filter bank samples both a deep CO_2 absorption feature (~1200 MHz) and ozone absorption features (~400 MHz). The ozone features are simultaneously sampled by the high resolution (5 MHz) filter bank (inset).

II. Observing Campaigns

Observations of ozone on Mars are only possible when the radial velocity between Mars and Earth is such that Martain ozone features are Doppler shifted away from telluric ozone absorption features into a spectral region of higher atmospheric transmittance (Fig. 1.2). This allows for only a few opportunities per year, and even less so if a large Martian angular diameter is targeted. Therefore, good coverage of the behavior of the atmosphere over the course of the Martian year requires many years on Earth. A summary of the heterodyne data sets used in this work is given in Table 2.1. L_S refers to solar longitude, which is the position of Mars in its orbit around the sun. The northern spring equinox is L_S=0°, the northern summer solstice is L_S=90°, and so on (see Fig. 1.1).

Table 2.1. Martian Ozone Heterodyne Data Sets

Year	Dates	L_S[c]	Northern Martian Season	Visible Pole (Sub-Earth Latitude)	Martian Angular Diameter[d]
1988[a]	3-7 June	208°	Early Autumn	South (23.2°S)	10.6 arcsec
1993[a]	14-16 Feb.	40°	Mid-Spring	North (3.7°N)	11.6 arcsec
1993[a]	4-7 July	102°	Early Summer	North (24.7°N)	4.6 arcsec
1995[a]	17-23 Mar.	74°	Late Spring	North (16.8°N)	11.6 arcsec
1999[a]	24-29 Mar.	115°	Early Summer	North (15.3°N)	13.3 arcsec
2003[b]	10-16 June	202°	Early Autumn	South (21°S)	13.8 arcsec
2003[b]	1-3 Nov.	291°	Early Winter	South (23°S)	14.7 arcsec

a Instrument: IRHS
b Instrument: HIPWAC
c L_s is solar longitude, where 0° is northern spring equinox.
d Instrument field-of-view 1 arcsecond FWHM.

Included in Table 2.1 is the first successful attempt to directly observe ozone on Mars from the Earth in 1988 by Espenak *et al.* [1991]. Those data are re-reduced and re-analyzed in this work for consistency and comparison. Also included are two 2003 data sets that were acquired specifically for this work. The other data sets were reduced and analyzed for the first time in this work. All together, the data sets provide a sampling of a variety of Martian seasons and orbital positions (L_S).

III. Data Acquisition and Reduction Schemes

The local oscillator used in this work was a $^{16}O^{12}C^{16}O$ gas laser. This provided access to strong ro-vibrational ozone features around 9.7 μm. The laser was tuned to the P branch of the 9.7 μm band of CO_2, to either the P(32) transition (1035.4736 cm^{-1}) or the P(36) transition (1031.4774 cm^{-1}), depending on the Earth/Mars radial velocity at the time of the observations (Table 2.2). The spectral regions around these transitions contain strong ozone lines as well as spectral structure that allows corresponding Martian

ozone lines to be Doppler shifted into regions of higher telluric transmittance. Observations are made at various latitudes on Mars and, because in most cases the beam is small relative to the size of Mars, the beam covers ~10° of latitude. The pointing is maintained over the course of many 2-4 minute integrations, and the scans are stacked together in order to improve the signal-to-noise ratio. As a result, each spectrum covers a range of longitudes that change with the rotation of Mars, but the local time on Mars is maintained. Most observations are made close to the limb of Mars in order to maximize the available column abundance of ozone.

Table 2.2. $^{16}O^{12}C^{16}O$ laser local oscillator transitions used for observing ozone on Mars.

Year	Dates	CO_2 transition	CO_2 transition frequency (cm^{-1})	CO_2 transition wavelength (μm)
1988	3-7 June	P(36)	1031.4774	9.695
1993	14-16 Feb.	P(32)	1035.4736	9.657
1993	4-7 July	P(32)	1035.4736	9.657
1995	17-23 Mar.	P(32)	1035.4736	9.657
1999	24-29 Mar.	P(36)	1031.4774	9.695
2003	10-16 June	P(36)	1031.4774	9.695
2003	1-3 Nov.	P(32)	1035.4736	9.657

The data reduction is performed using software that I initially developed for the IRHS Titan wind analyses [Kostiuk *et al.* 2001] and further modified and improved for use with the large amount of data in this project. The individual scans are divided by blackbody calibration scans taken close in time to remove the instrumental intensity roll-off that results from the frequency response of the infrared detector. Spectra are assembled by stacking scans together according to their date of observation and position on Mars.

The resulting spectra contain contribution from both Earth and Mars, therefore the telluric components must be removed in order to retrieve Martian ozone abundances.

Observations were made of the atmosphere of Earth against the Moon in order to characterize the transmittance of Earth's atmosphere at the time of observation of Mars. The subsequent radiative transfer analysis retrieved model Earth atmospheres to be used for removing the telluric component from spectra of Mars, as well as additional Earth science [Ch. 3, Fast *et al.* 2004]. However, because the spectra are double-sideband, it is not possible to simply remove the telluric component and proceed to radiative transfer analysis of the spectra of Mars. The initial analysis of Earth ozone serves as a starting point, but the transmittance of both Earth and Mars must be modeled together, and this is detailed in Ch. 4.

Chapter 3: Modeling Earth's Atmospheric Transmittance and Ozone Profile

I. Ozone Profile Retrieval

In order to characterize the transmittance of Earth's atmosphere during the observations of Mars, absorption spectra of the Earth's atmosphere against the Moon were taken. The analyses of these spectra were extended to not only serve the Martian ozone project, but to investigate infrared heterodyne spectroscopy as a technique for passive retrieval of ozone abundance height profiles for Earth. This work is also described in Fast *et al.* [2004].

Ozone plays an important role in Earth's atmosphere as an absorber of ultraviolet radiation and in maintaining radiative balance. Long term monitoring of ozone is important for understanding and quantifying variability due to natural influences (solar activity, season, chemistry, circulation) and to anthropogenic influence. Active and passive remote techniques such as lidar, microwave, and Umkehr (Dobson measurements at different viewing angles) and in situ probes (ozonesonde) are routinely employed to measure the vertical profile of ozone, and total column abundance is acquired through Dobson spectrophotometry [e.g. McPeters *et al*. 1999]. Infrared heterodyne spectroscopy has also been utilized to study height profiles of terrestrial stratospheric constituents such as ozone [e.g. Frerking and Muehlner 1977, Abbas *et al.* 1979, Fukunishi *et al.* 1990, McElroy *et al.* 1990, Sonnabend *et al.* 2002] and methane [Koide *et al.* 1995]. The work presented here represents the most extensive application of heterodyne spectroscopy to the study of ozone on Earth to date, with data sets sampling six different periods between 1988 and 2003 (Table 2.1).

Infrared heterodyne spectra of Earth's atmosphere were taken against the Moon. Over the spectral range of these measurements (.001 μm), the Moon's thermal continuum is essentially flat. The contribution of the reflected solar spectrum at 9.7 μm is negligible (see Appendix 1). Features in the spectrum represent the variation of the Earth's atmospheric transmittance due to absorption by ozone and by carbon dioxide (which is weak in this interval). Spectra were acquired at multiple values of airmass. Individual integrations lasting 3-6 minutes each were averaged into bins of 0.1 airmass for comparison to model spectra (Figs. 3.1, 3.3).

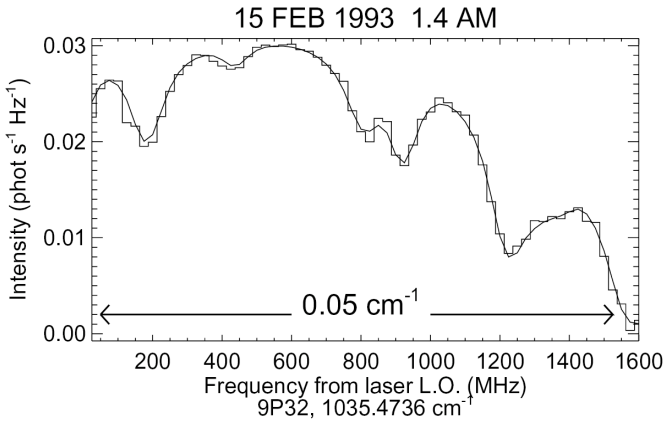


Figure 3.1. Example heterodyne double-sideband spectrum at 25 MHz spectral resolution against the Moon (histogram) showing individual absorption features that are matched by a radiative transfer model (solid line). Except for a weak CO_2 feature at 0 MHz, all structure is due to Earth's atmospheric ozone.

The transmittance of the terrestrial atmosphere is modeled using the line-by-line radiative transfer package GENLN2 [Edwards 1992]. The radiance of the atmosphere is also modeled and, although minor, is taken into account in this analysis. A standard atmospheric model is modified to produce radiative transfer model spectra consistent with the data. The starting-point temperature and molecular mole fraction profiles are from the AFGL tropical (15°N) atmospheric model [Anderson *et al.* 1986] consistent

with the ~20°N latitude of Mauna Kea. The profiles and the regions of greatest contribution to the spectra are shown and explained in Fig. 3.2.

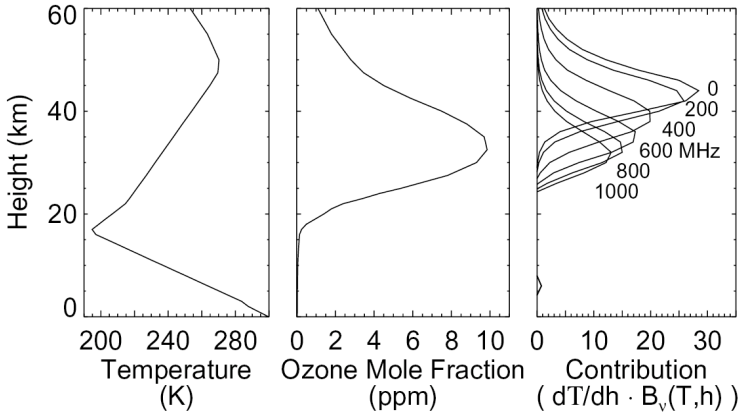


Figure 3.2. AFGL tropical (15°N) thermal and ozone mole fraction profiles. Contribution functions are shown for the center (uppermost profile) and wings (lower profiles, 200 MHz increments) for one of the target ozone absorption features, indicating that line wing contribution originates at altitudes below (i.e. pressures above) that of the line center. Contribution is calculated by multiplying the change in atmospheric transmittance with height by the Planck function at a particular frequency and altitude. This is an indication of the formation region of the modeled absorption feature at line center and along the wing at different frequencies (every 200 MHz) from line center.

The infrared heterodyne spectra are most sensitive to the 25-50 km region with an altitude resolution of ~8 km. The stratospheric portions of the ozone mole fraction profile and the temperature profile are modified by scale factors and corresponding GENLN2 radiative transfer models of the emergent spectrum are generated, resulting in a library of candidate model spectra corresponding to a grid of model parameters. A similar library of model spectra is generated for each 0.1 airmass bin required by the data. When a grid of models is compared to one of the heterodyne spectra, a grid of RMS values results. The Fisher F-statistic (also known as the ratio-of-variances method) is used to determine the region around the best-fit stratospheric ozone mole fraction and temperature profile scale factors (Fig. 3.3) that meets a 1σ confidence criterion. The

best-fit parameters from multiple spectra were combined statistically according to the estimated variance of each retrieved parameter, resulting in retrieved profiles and error bars (Figs. 3.4, 3.5).

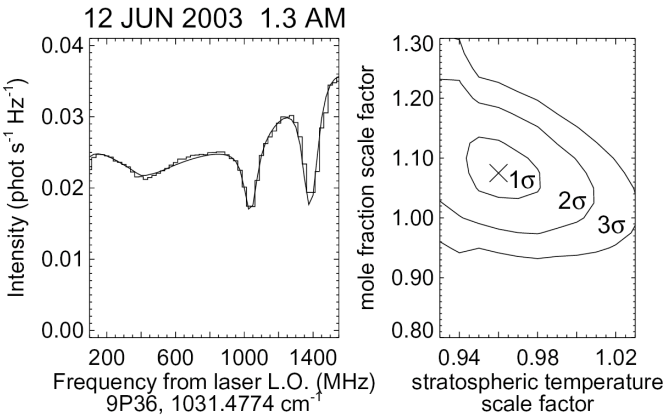


Figure 3.3. The contour plot indicates how well radiative transfer models using different scalings of the thermal and ozone mole fraction profiles fit the spectrum at left. The "X" marks the best-fit parameters, which produce the model spectrum shown at left.

Although the altitude of the ozone peak is not highly variable at this latitude, the range of variation was explored in order to introduce reasonable profiles into the radiative transfer modeling. The stratospheric part of the AFGL ozone profile was fit to Mauna Loa Observatory (MLO) lidar ozone profiles [McDermid *et al.* 1995] from many years by applying a scaling factor and by shifting the stratospheric ozone in altitude. In many cases, the AFGL profile had to be shifted down 1 km in altitude in order to fit the lidar data. Therefore, in addition to the GENLN2 models described earlier, model spectra were generated with the stratospheric portion of the ozone profile shifted down 1 km in altitude. Both sets of model spectra were compared to the heterodyne data and the best fits of the two altitude cases to a heterodyne spectrum were usually statistically indistinguishable from each other. There was no evident correlation between the two

altitude cases and the precision of the fit. However, the MLO Dobson total ozone column density measurements [Komhyr *et al.* 1997] can provide an additional constraint, pointing to one of the two models. It was found that this method produced model ozone profiles consistent with those measured through active and in situ means (lidar, ozonesonde).

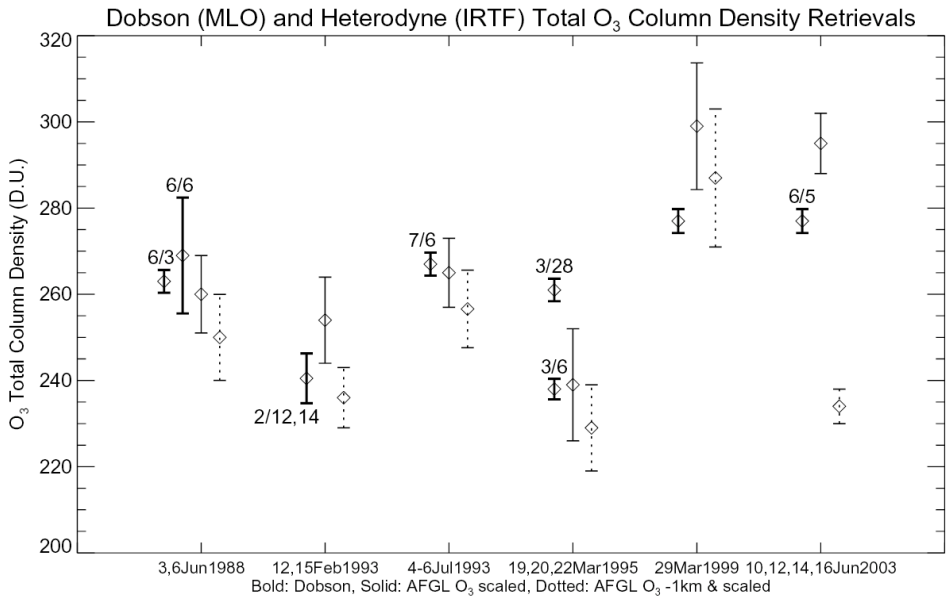


Figure 3.4. Ozone total column density retrievals. Bold indicates Dobson measurements (dates displayed). Other error bars indicate retrievals from radiative transfer analysis of heterodyne spectra using a scaled, unshifted AFLG ozone profile (solid), and a scaled profile shifted down 1 km in altitude (dotted).

II. Results and Comparison to Other Methods

Column densities retrieved from the best-fit models are presented in Table 3.1 and Fig. 3.4. The Dobson measurements are compared to radiative transfer fits obtained using a scaled AFGL profile, as well as that same profile shifted down 1 km before scaling. In choosing between these two cases, the preferred case is the one in which the Dobson measurements agree with the heterodyne retrieval, and the corresponding

abundance profile and temperature profile scale parameters are chosen. This is checked in Fig. 3.5, where the retrieved model ozone profiles themselves are compared to nearby ozonesonde [Johnson *et al.* 2002] and lidar [McDermid *et al*. 1995] profiles. The bold profiles are those chosen based on their consistency with Dobson column density measurements as just described. The dotted profiles were rejected because of inconsistency with the column densities retrieved from Dobson spectrophotometer measurements. The model profiles chosen using this column density criterion are consistent with available ozonesonde and lidar measurements.

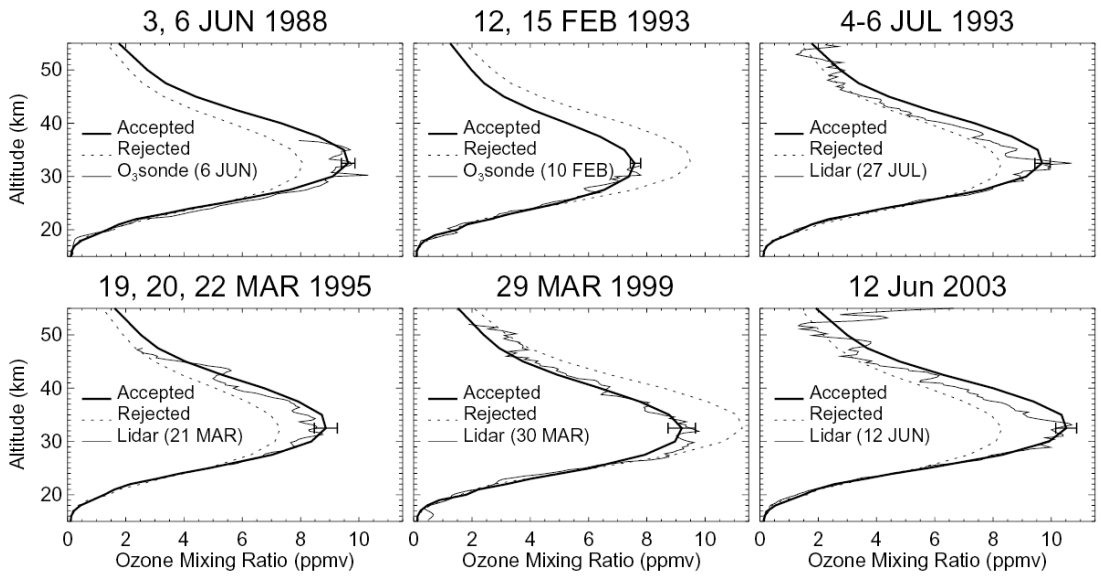


Figure 3.5. Model ozone profiles and 1σ uncertainties retrieved from heterodyne spectra compared to available nearby lidar [McDermid *et al*. 1995] or ozonesonde [Johnson *et al.* 2002] profiles. The bold profiles indicate those chosen according to their consistency with Dobson column densities. Dotted profiles were rejected because their resulting column densities differed from the Dobson measurements. The error bar indicates the range of statistically acceptable (1σ) scaled ozone profiles.

For the three summer measurements, the unshifted ozone profile provided satisfactory fits to the heterodyne spectra and column densities consistent with Dobson

measurements, with high ozone abundances as expected in summer. The winter measurements show less similarity in their ozone profile retrievals. Sources of long-term and short-term variability (e.g. transport, solar activity, chemistry, tropospheric activity) need to be further investigated. The 2/93 and 3/99 measurements required that the model ozone profile be shifted down 1 km in altitude and scaled in order to both fit the spectra and agree with Dobson column densities. The 3/99 measurement made during the strong La Niña of '98-'00, however, had a much higher stratospheric ozone mole fraction and total column density. The 3/95 measurement made near solar minimum did not require an altitude shift in the mole fraction profile like the other winter measurements and was similar in column density to that of 2/93, but with a higher mole fraction due to the slightly higher altitude distribution. Day to day variations due to transport phenomena can also be responsible for the observed profile differences in the winter measurements.

Table 3.1. Total ozone column density retrievals for Earth

Date (UT)	IRHS retrieval (D.U.) using scaled AFGL profile…		MLO retrieval from Dobson Spectrophotometer Instrument No. 76 (D.U.)
	…not shifted in altitude	…shifted –1 km in altitude	
1988 June 3, 6	**260±9** [a]	250±10	263±1% (6/3/88), 269±5% (6/6/88)
1993 February 12, 15	254±10	**236±7** [a]	240±2.4% (2/12,14/93)
1993 July 4-6	**265±8** [a]	257±9	267±1% (7/6/93)
1995 March 19, 20, 22	**235±13** [a]	229±10	261±1% (3/6/95), 238±1% (3/28/95)
1999 March 29	299±15	**287±16** [a]	277±1%
2003 June 12	**280±14** [a]	227±10	279±1%

[a] Preferred model according to Dobson measurements.

The altitude shift applied to the ozone peak is slight and is consistent with adjustments to bring the standard AFGL profile into agreement with individual lidar scans, and may represent variability in particular altitude regions rather than an actual vertical shift of the ozone peak. For instance, Leblanc and McDermid [2000] examined lidar ozone profiles over a 6-year period at Mauna Loa and did not note any significant altitude shift of the ozone peak, but they did note some seasonal variation in the 30 km region and high variability in the 18 km region in addition to the seasonal variation of the overall ozone profile. The behavior in the 18 km region was attributed to high tropopause altitude and variability, and may be responsible for the variety of winter model ozone altitude distributions more so than solar activity.

III. Conclusions

The shape of the spectra of Earth need only be fit in order to provide a model atmosphere that can be used to remove the telluric contribution from Martian ozone spectra. However, detailed analysis results in the needed spectral shapes as well as accurate ozone profiles that compare well to those retrieved through active and in situ means. It has been shown here that a standard ozone profile can be shifted and scaled to produce radiative transfer spectra consistent with heterodyne measurements and total ozone column densities consistent with Dobson measurements. The scaling of a standard ozone profile to obtain total ozone column densities from heterodyne spectra has been done elsewhere [e.g. Mouanda *et al.* 1996]. It has been demonstrated here that slightly shifting a standard profile in altitude and scaling it can also produce an acceptable fit to a spectrum, yet result in different column abundance.

The combination of heterodyne spectroscopy and Dobson spectrophotometry provides ozone abundance and general distribution that is consistent with contemporaneous lidar and ozonesonde measurements, and is therefore a passive alternative to active and in situ techniques. Other species of interest such as water and ClO [e.g. Mumma et al 1983] are also accessible through heterodyne spectroscopy, enabling the passive monitoring of constituents important to ozone chemistry.

Chapter 4: Modeling Martian Ozone and Thermal Profiles

The heterodyne spectra are double-sideband spectra because of the nature of the instrument (Ch. 2). Contributions from lower and upper sidebands are included in the resulting double-sideband spectrum, which is essentially a normal (single-sideband) spectrum folded about the laser local oscillator frequency. A spectrum of Mars includes contribution from both Earth and Mars (Fig. 4.1), and the spectral shapes of both sources vary across the lower and upper sidebands due to the CO_2 and multiple ozone absorption features present in the instrument bandpass. Therefore, it is not possible to first remove the telluric contribution from a double-sideband spectrum before modeling the contribution from Mars. The contributions from both Earth and Mars to a double-sideband spectrum must be modeled together before extracting a Mars-only spectrum.

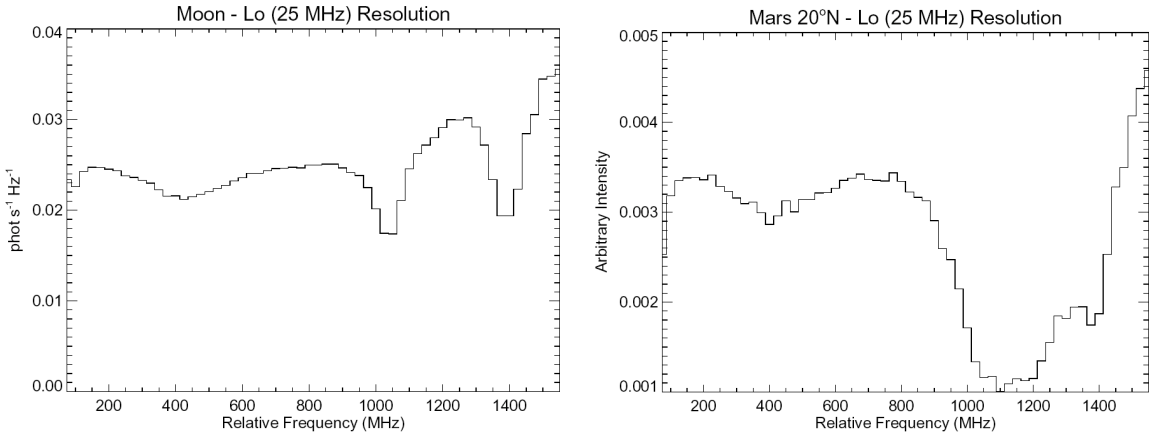


Figure 4.1. Double sideband spectra of telluric transmittance against the Moon (left) and Martian and telluric transmittance against Mars (right). The shape of the right spectrum is that of the telluric transmittance at left along with Martian ozone absorption at ~400 MHz and Martian CO_2 absorption at ~1200 MHz.

The Martian components of the spectra are modeled using the radiative transfer package BEAMINT [Hewagama *et al.* 2005], developed at NASA's Goddard Space Flight Center. BEAMINT combines a layer-by-layer radiative transfer modeling engine with an algorithm for modeling the contribution of the different parts of the instrument beam to the overall spectrum. This can be a noticeable improvement over a single point mean viewing angle model, especially when the viewing geometry is such that the 1" FWHM beam sees contribution from a wide range of planetary longitudes. When Mars was very large (10-15 arcsec.) relative to the size of the beam (1 arcsec.), the capability to model multi-element beam contribution did not produce significantly different line shapes compared to those modeled using a single-element beam. In the case of July 1993 where the disk of Mars was small (4.6 arcsec.), a multiple-element beam was tested to see if it produced significantly different line shapes from that of a single-element beam, and it did not. Single- and multi-element beams were also used to test the effect of poor seeing on the resulting line shapes, and the variation was found to be below the noise level of the observed spectra. Therefore a single-element model for the beam was used in the analysis of Martian spectra.

BEAMINT accepts planetary parameters, observation circumstances, molecular and thermal height profiles, and a molecular line atlas. Atmospheric and other parameters can be iterated until a best fit of a model spectrum to an observed spectrum is achieved. Standard formal 1σ uncertainties based on the number of free parameters and the variance between the observed and model spectra are returned.

The telluric components of the spectra are modeled using GENLN2 [Edwards 1992], which was used in the analysis of the transmittance of Earth's atmosphere (Ch. 3).

After that analysis was completed, BEAMINT was modified to either read in an existing GENLN2 model transmittance spectrum or iterate on terrestrial atmospheric parameters through repeated launches of GENLN2. BEAMINT applies the single-sideband GENLN2 transmittance to the single-sideband model spectrum of Mars before folding it about the laser local oscillator frequency and comparing it to an observed double-sideband spectrum. Initial models of telluric transmittance for the Martian ozone analysis were taken from the analysis of ozone on Earth described in Ch. 3, but in most cases the fitting capability was utilized in order to adjust ozone and CO_2 abundance for Earth to fine-tune the telluric transmittance model for particular spectra of Mars.

The Martian atmospheric parameters that must be either varied or constrained in the fitting process include a scale factor applied to the initial ozone height profile, an additive adjustment to the initial thermal profile, atmospheric pressure at the surface, and surface temperature. The Martian CO_2 absorption feature present in the instrument bandpass is the pathway to all of the parameters (except ozone) and is very important for constraining the thermal profile so that the ozone abundance retrieval is accurate. The CO_2 line shape is sensitive to the combination of surface temperature, atmospheric temperature, and surface pressure. The line shape would also indicate the presence of large amounts of dust. For example, heterodyne observations (outside of this work) of 10.5 μm non-LTE CO_2 emission at ~40 km were made during the global dust storm of 2001. The high altitude non-LTE emission was present, but the corresponding absorption feature due to CO_2 lower in the atmosphere was very shallow, indicating that the measurement did not probe all the way to the surface. However, these measurements at 9.7 μm are not nearly as sensitive to normal amounts of dust as observations at shorter

wavelengths, such as ultraviolet measurements. Also, dust storms tend to occur during warmer perihelion periods (L_S~180-360°), and most of the data sets in this work were acquired during aphelion periods. Extinction by large amounts of dust was not evident in any of the ozone heterodyne data sets of Mars.

Contamination from Earth's atmosphere and insufficient signal-to-noise prevent direct inversion of the CO_2 line to retrieve an accurate thermal profile. Instead, the surface temperature and initial thermal profile are varied until a best fit to the CO_2 line is achieved. The atmospheric surface pressure requires an external constraint. Information on atmospheric temperature, surface pressure, and surface temperature are contained in the CO_2 line shape, but the simultaneous fitting of all three parameters, along with the other atmospheric parameters, resulted in retrievals for some parameters that fell outside the range of observed values for Mars. Also, calculated 1σ uncertainties for each parameter take into account correlations with the other fit parameters, and the combination of parameters resulted in very large uncertainties (~100 K and ~9 mbar). Constraining the surface pressure reduced the uncertainties in the other fit parameters considerably (over an order of magnitude for temperature). Doing so is reasonable because surface vehicle data such as those from Viking [Zurek *et al.* 1992] show that surface pressure varies consistently from year to year (barring disruptions such as large scale dust storms). For example, Tillman *et al.* [1993] developed an orbital pressure model based on the Viking lander data, and after the removal of their model from Viking 1 pressure data from two different years, the variances of the remaining residuals were 0.35% and 0.69% of the variances of the original data. That model was updated according to additional pressure information from the Mars Pathfinder mission and

incorporated into software[1] developed at NASA's Goddard Space Flight Center. This software generates a surface pressure for a particular latitude and longitude based on the corresponding altitude and orbital position (L_S). The altitude information comes from the Mars Global Surveyor (MGS) Mars Orbiter Laser Altimeter (MOLA) [D. E. Smith *et al.* 2001]. Modeled surface pressures are used as a constraint during the radiative transfer analysis of the Mars spectra.

Initial thermal profiles used in the analysis are those retrieved from MGS Thermal Emission Spectrometer (TES) observations (e.g. Fig. 4.2) [M. D. Smith *et al.* 2001, private communication]. MGS TES began observing in March of 1999, and the data utilized here were taken either around the same time as an ozone data set, or at the same orbital position (L_S) as a pre-MGS ozone data set. MGS samples 14:00 local time and the ozone spectra analyzed here sample roughly between 10:00 and 15:00. The entire MGS thermal profile is modified by incremental amounts of temperature in the fitting process (Fig. 4.2). The Mars Exploration Rover mini-TES observations over the course of a day show that this is a reasonable way to modify the profile during the local times considered [M. D. Smith, private communication]. Initial surface temperatures are also taken from MGS TES observations and are allowed to vary in the fitting process along with the thermal profile additive term in order to best fit the CO_2 absorption line shape. Although the final fit parameters ultimately deviate somewhat from the MGS data because of local time and pointing variations, the data are useful for identifying unreasonable fits and for constraining parameters when warranted.

[1] The original code was written by Hugh Kieffer. Modifications were made by Monte Kaelberer, Alex Mekelburg, John Pearl and Eric Winter.

The CO_2 line cores proved to be difficult to fit at times, and it was recognized that high altitude non-LTE emission was filling in the line core. Limb observations tend to show this filling of the line core to a greater degree, further indicating contamination from high altitude. Therefore, channels at the core of the CO_2 line were masked and not considered in the fitting process. That is reasonable for this analysis because the CO_2 wing shapes are sensitive to the lower altitude temperatures where the bulk of the ozone contribution to the spectra originates (below ~10-20 km).

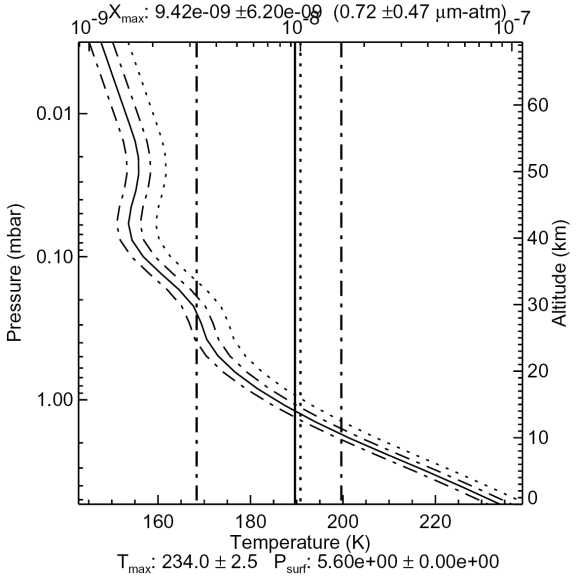


Figure 4.2. Example thermal profile from Mars Global Surveyor [M. D. Smith *et al*. 2001, private communication] and constant-with-height ozone mole fraction profile. Dotted curves are initial profiles, solid curves are post-analysis profiles, and dot-dash curves represent 1σ uncertainties in a radiative transfer fit. They illustrate how the profiles are modified in the fitting process.

A constant-with-height ozone mole fraction is assumed in the model, and is modified by a multiplicative factor in the fitting process (Fig. 4.2). An investigation into the altitude distribution of ozone is presented in Ch. 6. An additional parameter, a scale factor applied to the data, is also required. Although the data have been absolutely calibrated, a scale factor is still required to take into account calibration uncertainty,

pointing uncertainty due to differential refraction, tracking errors and seeing, as well as the variation in transmittance, humidity, and thin clouds at the observing location. Allowing a scale factor to vary in the fitting process causes the fully-resolved CO_2 line shape itself to drive the fit of the atmospheric temperature and surface temperature combination. The column densities that are ultimately retrieved are relative to the local surface on Mars.

There are two spectra for each position (Ch. 2). A 25 MHz resolution spectrum covers 1600 MHz (double sideband) and contains both the Martian ozone and CO_2 absorption features, and the spectrum is modeled according to the described technique. A simultaneous 5 MHz resolution spectrum covers 320 MHz (double sideband) across the ozone absorption features. The thermal information in the CO_2 absorption feature is important for retrieving ozone abundance, and so the 5 MHz spectrum is inserted into the 25 MHz spectrum before modeling. The retrieved parameters from that combined spectrum are for the most part consistent with the 25 MHz-only fit, and the uncertainty on the ozone abundance tends to be smaller because of the denser sampling across the ozone features.

Once a best fit is achieved to a double sideband spectrum of the combined atmospheric transmittance of Earth and Mars, and assuming that the model is accurate, a Mars-only spectrum can be retrieved. The model transmittance in the sideband opposite the target Martian absorption features is first subtracted from the double-sideband data. This creates a single-sideband spectrum of Mars and Earth. The spectrum is then divided by the model transmittance of Earth in that sideband. This results in a single-sideband Mars-only "data" spectrum, and those from this work are displayed in Ch. 5.

The standard formal 1σ uncertainties on each of the fit parameters that are returned in the radiative transfer analysis take into account the correlations with other parameters as well as the variance between the observed and model spectra. The ozone column abundance uncertainties listed and displayed in Ch. 5 reflect correlations with the other parameters (atmospheric and surface temperature, scale factor, telluric ozone and CO_2) and are therefore better representations of the accuracies of the retrievals than uncertainties in ozone abundance when the other parameters are held fixed.

Chapter 5: Ozone Abundances from Infrared Heterodyne Spectra of Mars

I. Atmospheric Contribution to Absorption Features

Infrared heterodyne measurements of ozone and CO_2 on Mars resolve the shapes of individual absorption features and therefore include contribution from the different heights (pressure levels) that influence the line shapes. Example contribution is shown in Fig. 5.1. Contribution is calculated by multiplying the change in atmospheric transmittance with height, dT/dh, by the Planck function, $B_\nu(T)$, at a particular frequency and altitude (i.e. temperature). This is an indication of the region of formation of the modeled absorption feature at line center and along the wing at different frequencies from line center. Higher altitudes are probed by the CO_2 line core while the wings probe lower altitudes (higher pressures), as shown in the left panels. The right panels show how the bulk of the contribution to the ozone feature is from altitudes below ~20 km for this constant-with-height ozone mole fraction model. In Ch. 6, ozone distributions with scale heights different from the overall atmosphere as well as with excess ozone at high altitudes will be explored. If ozone scale height is less (greater) than that of the overall atmosphere (i.e. CO_2), then the contribution function would show a relative increase (decrease) at low altitudes and a relative decrease (increase) at high altitudes compared to the constant-with-height mole fraction case. If there is excess ozone at high altitudes (>20 km), then contribution in excess of that of the constant-with-height case will show up at those altitudes.

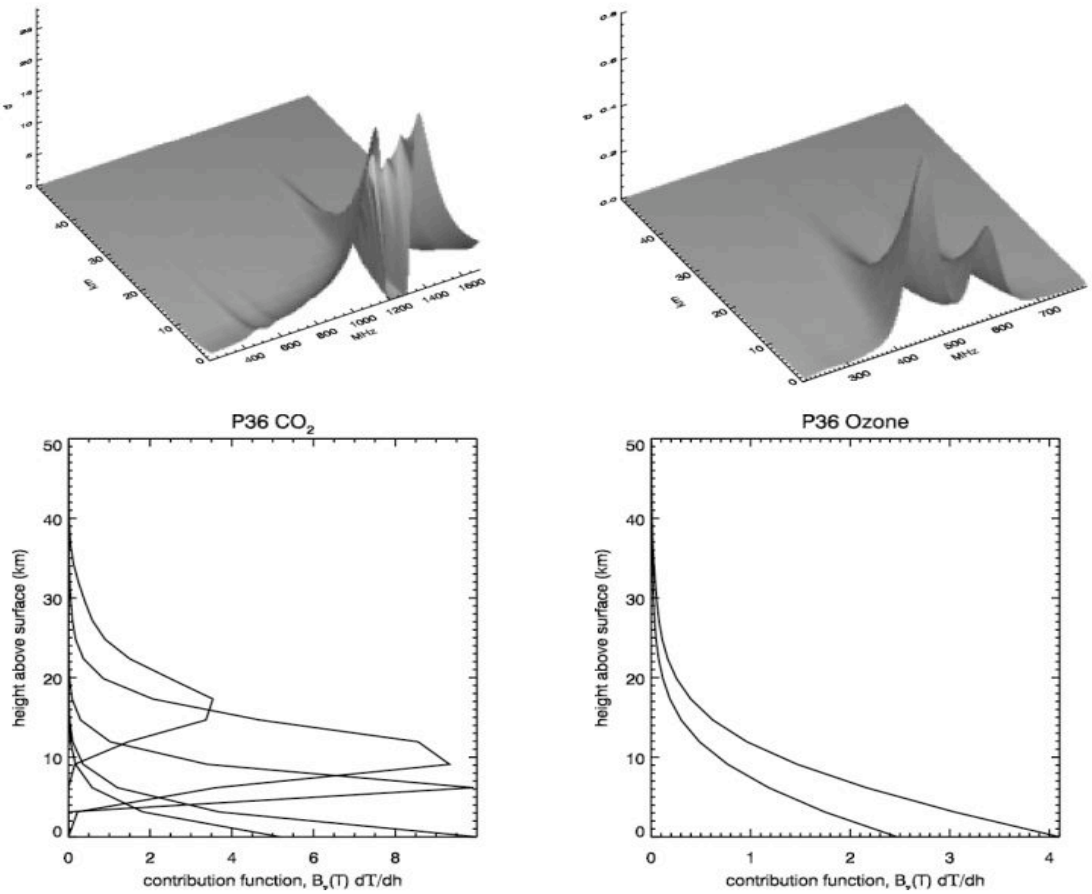


Figure 5.1. Example contribution functions. The upper panels show contribution to the line intensities (z-axis) as a function of frequency (x-axis) and height (y-axis). The large feature on the upper left panel is CO_2, while the smaller feature to its left is ozone, which is displayed on its own in the upper right panel. The lower panels show slices of the contribution functions at different frequencies.

II. Seasonal and Solar Cycle Information

Sub-solar and sub-Earth latitudes, along with seasonal information, are given in Table 5.1. Additional specifics about the different data sets were presented in Ch. 2. It should be noted that the obliquity of both Mars and Earth is ~24°, resulting in similar variations in sub-solar latitude over the course of their respective years. The higher

eccentricity of the orbit of Mars and the fact that perihelion and aphelion fall near the solstices enhance the seasons on Mars (e.g. longer southern winter).

Table 5.1. Seasonal coverage and sub-solar latitudes of observations of Mars ozone

L_S[a]	Year	Dates	Northern Martian Season	Sub-Solar Latitude	Sub-Earth Latitude
40°	1993	14-16 Feb.	Mid-Spring	16.3°N	3.7°N
74°	1995	17-23 Mar.	Late Spring	24.4°N	16.8°N
102°	1993	4-7 July	Early Summer	24.8°N	24.7°N
115°	1999	24-29 Mar.	Early Summer	23.0°N	15.3°N
202°	2003	10-16 June	Early Autumn	8.8°S	21°S
208°	1988	3-7 June	Early Autumn	11.9°S	23.2°S
291°	2003	1-3 Nov.	Early Winter	23.7°S	23°S

a L_S is solar longitude or orbital position of Mars. 0° is the northern spring equinox.

Although the effect of solar activity on lower atmospheres is not well-studied, changing upper atmospheric temperature, density, and photolysis rates could possibly impact lower atmospheric composition and chemistry. Because the ozone observations sample many Martian years, it is important to note the state of solar activity during the observational period. This is particularly important for the observations made in June 1988 (L_S=208°) and June 2003 (L_S=202°), at essentially the same orbital position in different years. Dates of ozone observations are noted on a plot of sunspot numbers given in Fig. 5.2. None of the data sets were taken during a particularly strong period of solar activity, and the L_S=208° and 202° data sets were taken during periods of comparable solar activity.

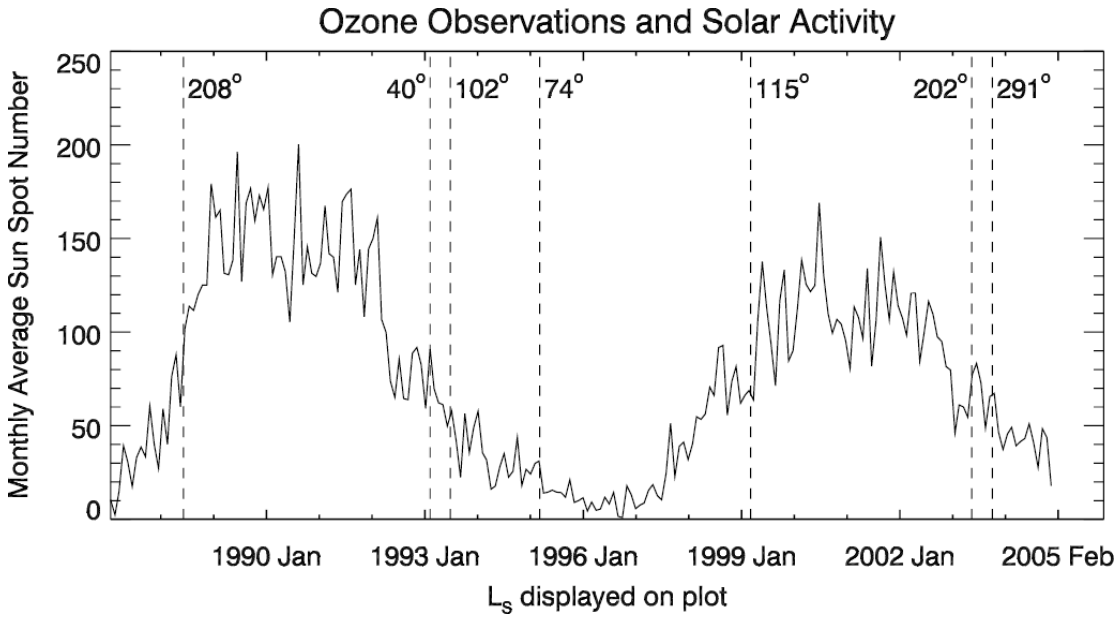


Figure 5.2. Dates and L_S values for IR Heterodyne ozone observations of Mars are noted on this plot of monthly average International Sunspot Numbers compiled by the Sunspot Index Data Center in Belgium.

III. Retrievals of Ozone on Mars

The results of the radiative transfer analysis of the heterodyne data sets of ozone on Mars are shown in the figures that follow. All retrieved ozone column densities (as well as accompanying water vapor column abundances from other investigators) are relative to the local surface on Mars. The error bars displayed on the filled diamond data points are standard formal 1σ uncertainties that are calculated during the radiative transfer fitting and include the effect of uncertainties in the other fit parameters (Ch. 4). The results are displayed in order of increasing L_S (40°, 74°, 102°, 115°, 202°, 208°, 291°), and the following is displayed for each of the orbital positions:

- A data summary figure showing the aspect geometry of Mars with field-of-view positions and the corresponding single-sideband spectra and models that resulted

from the radiative transfer analysis (Ch. 4). The 5 MHz resolution spectra are shown as insets on the corresponding 25 MHz resolution spectra.

- A map of Mars from Mars Orbiter Laser Altimeter (MOLA) data [D. E. Smith *et al*. 2001] from Mars Global Surveyor (MGS) showing the coverage of the observations in that data set. The coverage is determined by the size of the field-of-view on Mars combined with rotation over the course of an observation at a particular latitude and local time (offset from the central meridian longitude).
- Summary plots showing retrieved ozone column density and 1σ uncertainties for 25 MHz and 5 MHz resolution spectra. Numbers displayed with the retrievals indicate the day of the month. Contemporaneous measurements of total water column density (open diamonds or dotted curves) are also shown for investigating possible anticorrelation of ozone and water vapor abundance. (Ozone/water anticorrelation is addressed in Section IV of this chapter).
- A table with the retrieved ozone column densities and 1σ uncertainties from the 25 MHz and 5 MHz resolution spectra.

Plots of the 25 MHz resolution spectra for the observing runs using the P(32) transition of the heterodyne laser local oscillator (Table 2.2) will show a discontinuity, with the two components labeled USB and LSB. In these cases, the target ozone features were present in the upper sideband (USB) of the double-sideband spectrum, and the CO_2 feature was present in the lower sideband (LSB). In order to display all features in the single-sideband plot, the portions of the single-sideband spectrum retrieved after modeling that contain the features of interest are plotted together. Data sets taken at the

P(36) transition (Table 2.2) contain all features in the same (upper) sideband, and so only the one sideband is displayed.

In many of the spectra, the observed CO_2 line core has greater intensity than the modeled core, and occasionally an obvious emission feature appears. As mentioned in Ch. 4, this is attributed to high altitude non-LTE CO_2 emission filling in the line core. The bulk of the ozone contribution is from altitudes below 20 km, which is probed by the CO_2 line wings, and so the channels around the core were not used in the fitting process. It should also be noted that the heterodyne detector sensitivity decreases with frequency from the laser local oscillator frequency, and therefore the noise on the spectrum increases toward the high frequency end of the bandpass. The transmittance of the Earth's atmosphere also affects the signal-to-noise ratio along the bandpass, which was shown in Fig. 3.1 for the P(32) laser local oscillator transition and in Fig. 3.3 for the P(36) transition.

Ozone retrievals are presented from both the 25 MHz and 5 MHz resolution spectra, which agree for the most part. Occasional differences may be attributed to poorly placed noise, especially on the 25 MHz resolution spectra that do not sample the ozone features as densely. The uncertainties tend to be lower on the 5 MHz resolution spectra because of the denser sampling of the features, and those retrievals are applied to the science issues in this work. Apparent day-to-day variation at one latitude outside of the quoted uncertainties may also be due to poorly placed noise, or the behavior may be real (topographical, meridional, day-to-day). Further observations are required to study day-to-day behavior.

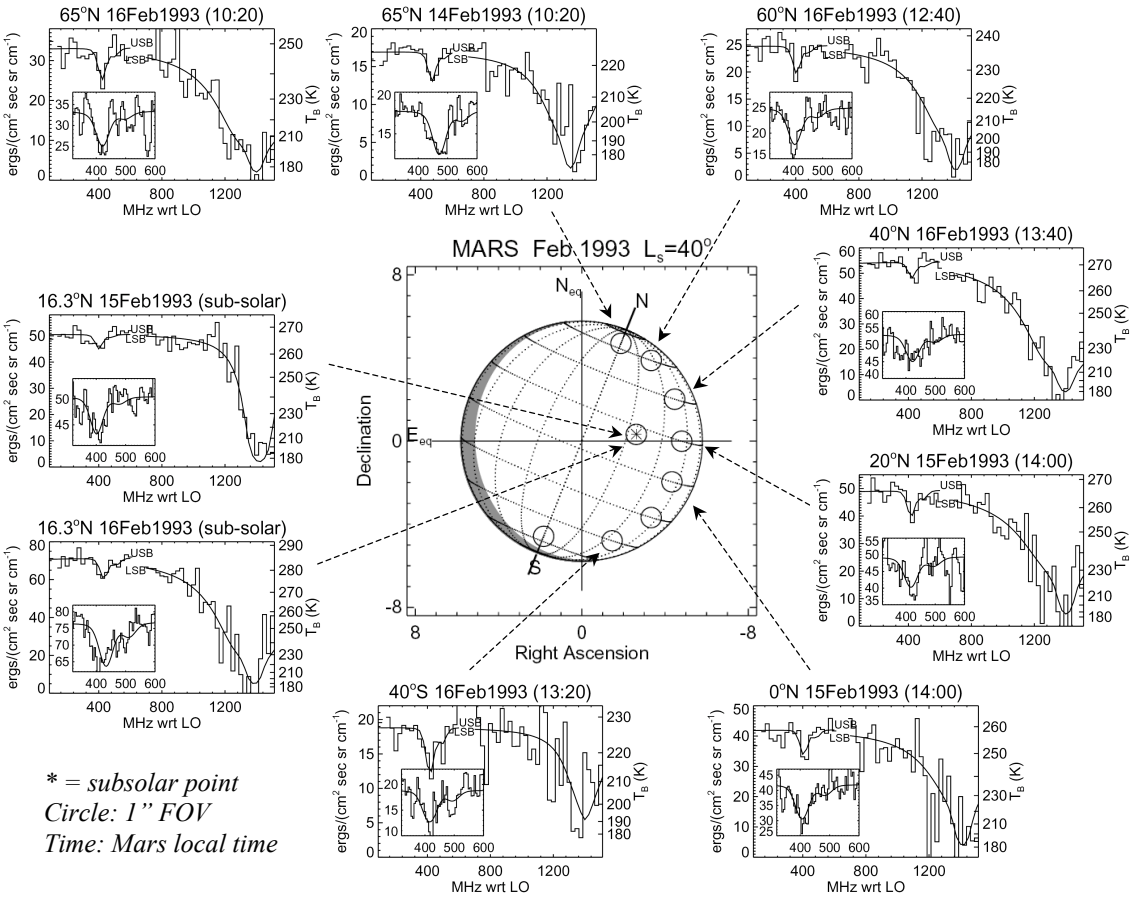
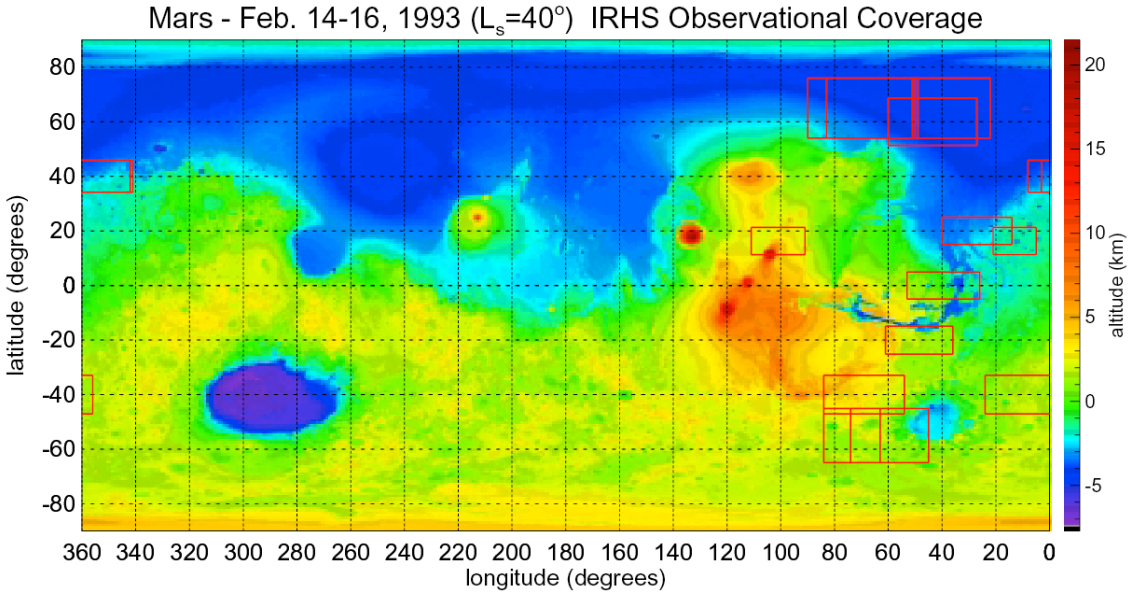


Figure 5.3. Martian observing geometry and heterodyne spectra (above) and observational coverage (below) from 14-16 February 1993, L_S=40°.



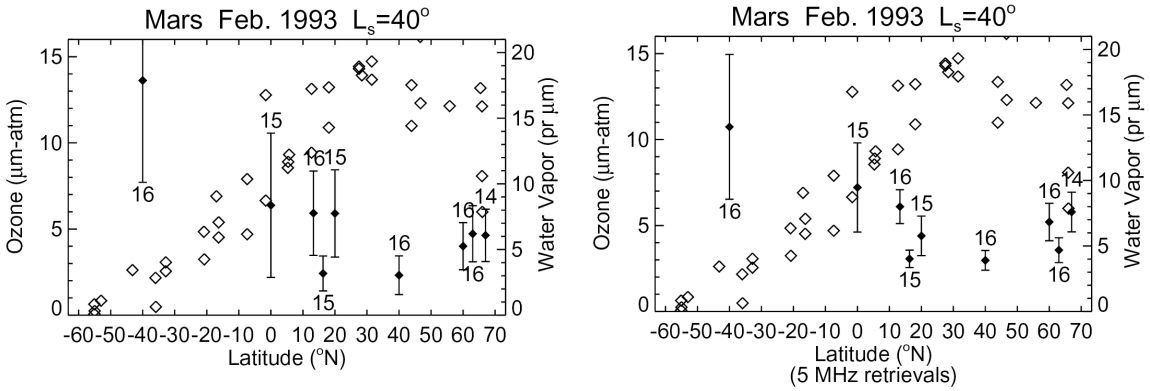


Figure 5.4. Total ozone column densities and 1σ uncertainties retrieved from 25 MHz (left) and 5 MHz (right) resolution infrared heterodyne spectra taken during 14-16 February 1993 at Ls=40°. Water vapor column densities from 9-11 March 1993 [Sprague *et al.* 1996, private communication] are shown as open diamonds.

Table 5.2. Total ozone column densities and 1σ uncertainties retrieved from infrared heterodyne spectra taken during 14-16 Feburary 1993 at Ls=40°.

Latitude (°N)	[O3] cm^{-2} (5 MHz[a])	1σ uncertainty	[O3] cm^{-2} (25 MHz[b])	1σ uncertainty	Day of Month
-40	10.7	4.2	13.6	5.9	16
0	7.2	2.6	6.4	4.2	15
16	6.1	1.0	5.9	2.4	16
16	3.1	0.5	2.4	1.0	15
20	4.4	1.1	5.9	2.5	15
40	3.0	0.6	2.3	1.1	16
60	5.2	1.1	4.0	1.4	16
65	3.6	0.7	4.7	1.6	16
65	5.8	1.2	4.6	1.5	14

a Retrieval from 5 MHz resolution spectrum.

b Retrieval from 25 MHz resolution spectrum.

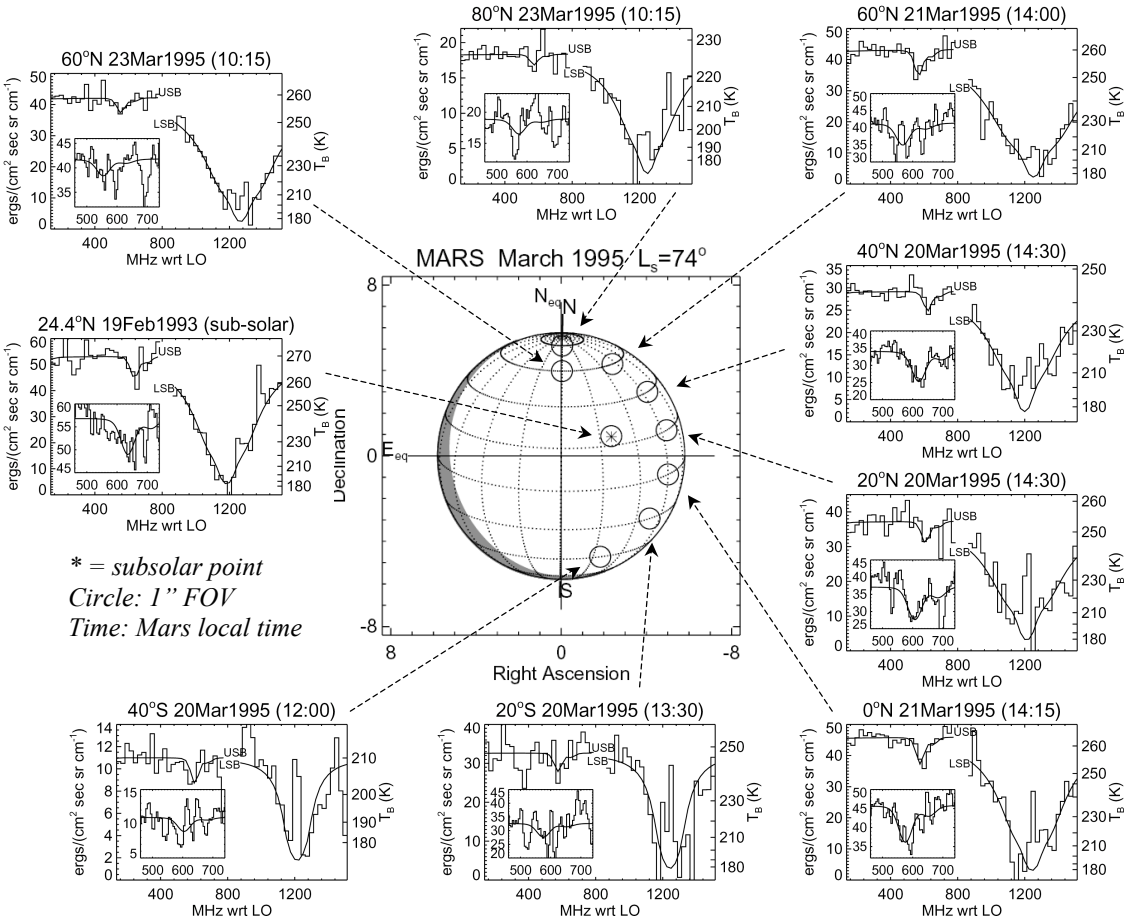
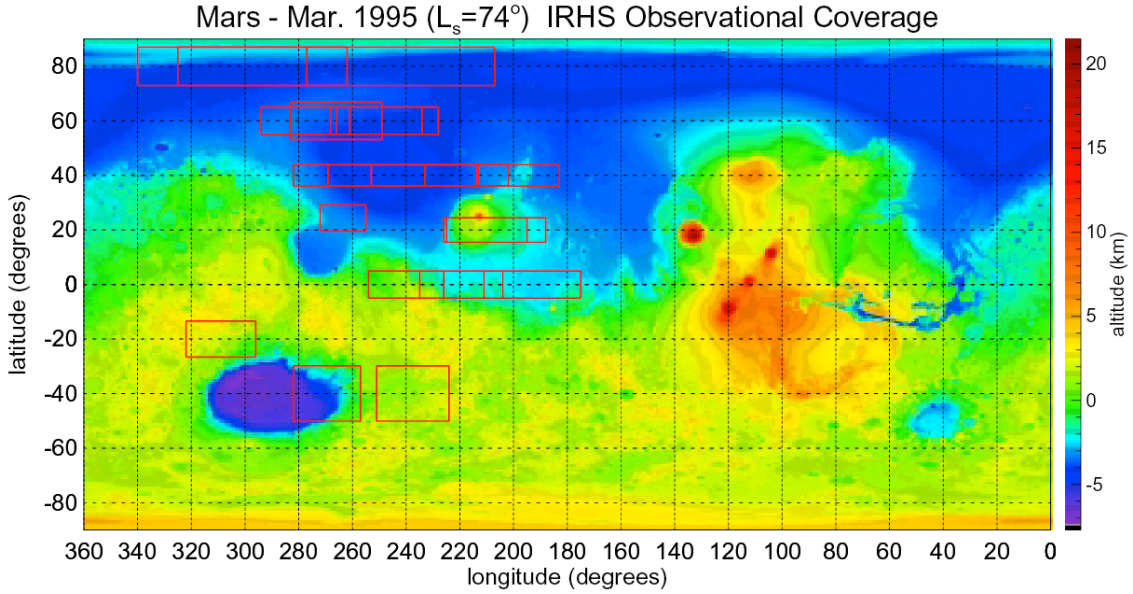


Figure 5.5. Martian observing geometry and heterodyne spectra (above) and observational coverage (below) from 17-23 March 1995, L_S=74°.



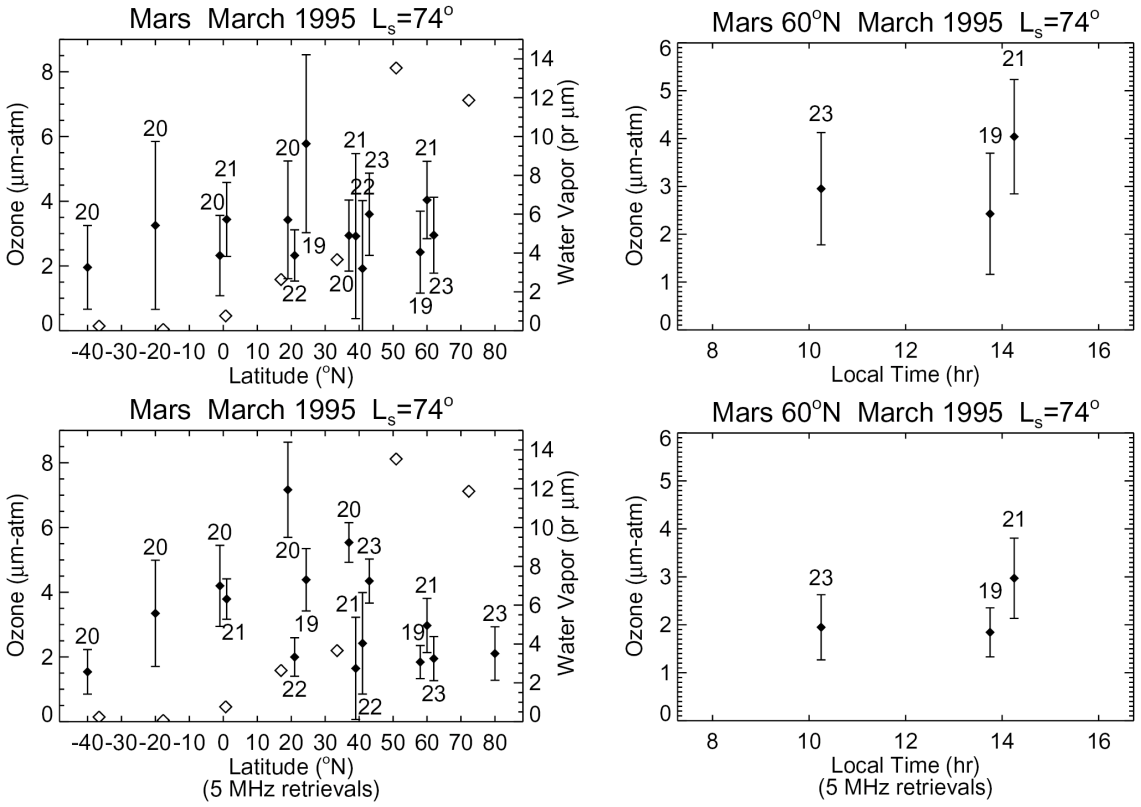


Figure 5.6. Total ozone column densities and 1σ uncertainties retrieved from 25 MHz (top left) and 5 MHz (bottom left) resolution infrared heterodyne spectra taken during 17-23 March 1995 at Ls=74°. Water vapor column densities from 20 March 1995 [Sprague *et al.* 1996, private communication] are shown as open diamonds. Ozone column densities retrieved at 60°N are displayed as a function of local time from 25 MHz (top right) and 5 MHz (bottom right) resolution spectra. No significant variation in ozone column density is seen over the local times sampled (~4 hours).

Table 5.3. Total ozone column densities and 1σ uncertainties retrieved from infrared heterodyne spectra taken during 17-23 March 1995 at Ls=74°.

Latitude (°N)	[O3] cm^{-2} (5 MHz[a])	1σ uncertainty	[O3] cm^{-2} (25 MHz[b])	1σ uncertainty	Day of Month
-40	1.5	0.7	2.0	1.3	20
-20	3.3	1.6	3.3	2.6	20
0	4.2	1.3	2.3	1.2	20
0	3.8	0.6	3.4	1.1	21
20	7.2	1.5	3.4	1.8	20
20	2.0	0.6	2.3	0.8	22
24	4.4	1.0	5.8	2.8	19
40	5.5	0.6	2.9	1.1	20
40	1.6	1.6	2.9	2.5	21
40	2.4	1.6	1.9	2.1	22
40	4.3	0.7	3.6	1.3	23
60	1.8	0.5	2.4	1.3	19
60	3.0	0.8	4.0	1.2	21
60	1.9	0.7	3.0	1.2	23
80	2.1	0.8	-	-	23

a Retrieval from 5 MHz resolution spectrum.

b Retrieval from 25 MHz resolution spectrum.

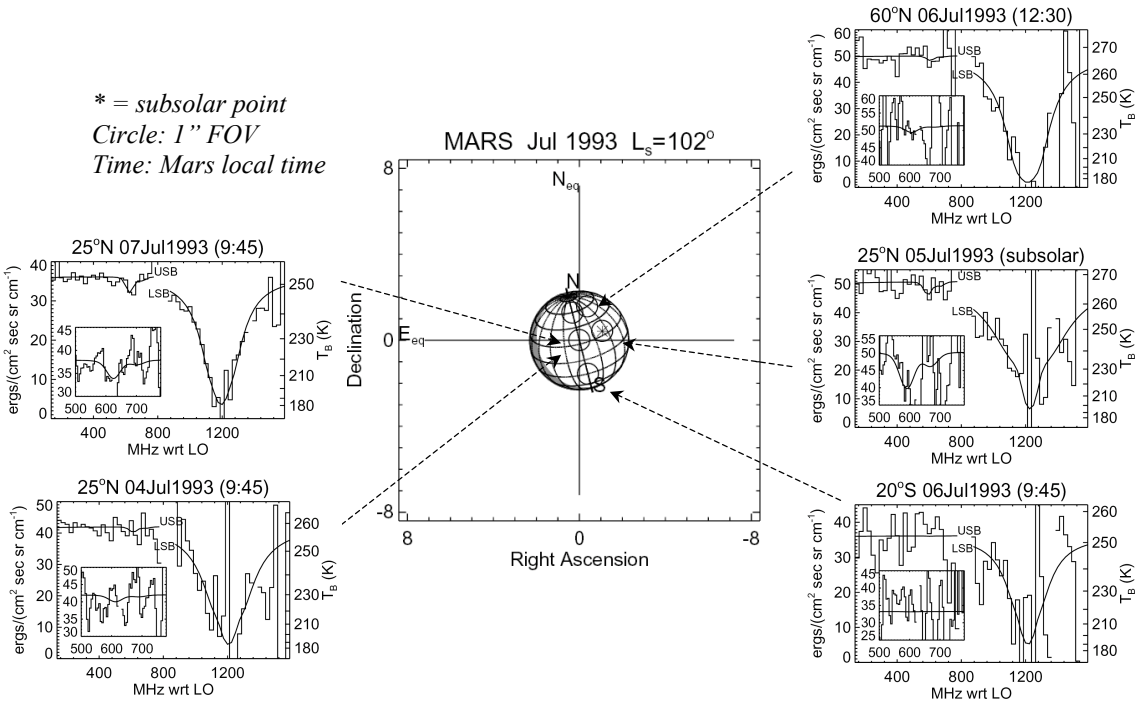
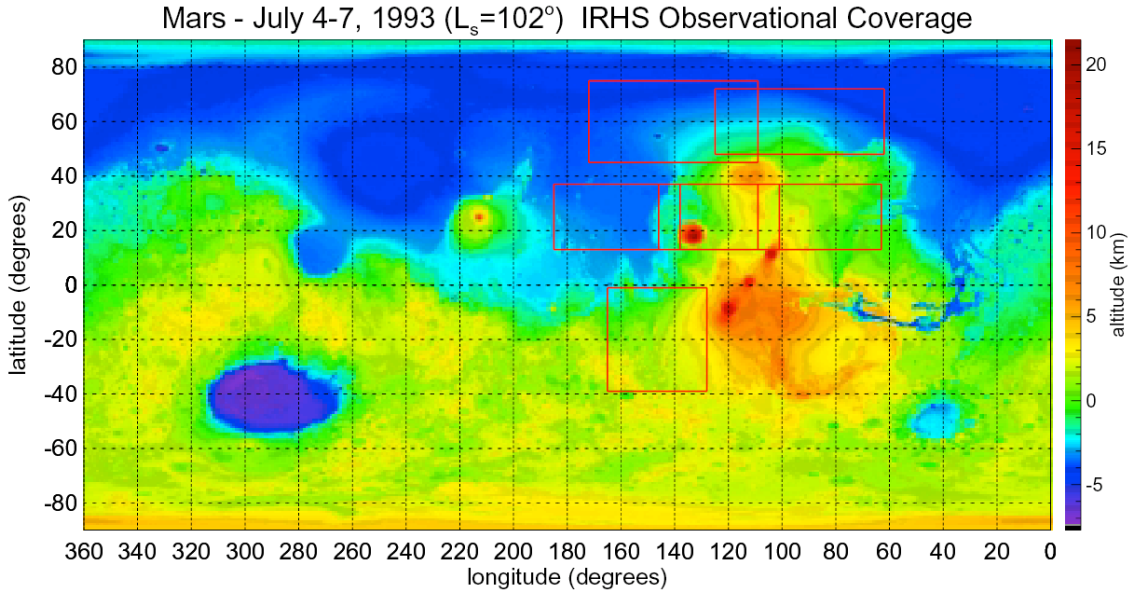


Figure 5.7. Martian observing geometry and heterodyne spectra (above) and observational coverage (below) from 4-7 July 1993, L_S=102°.



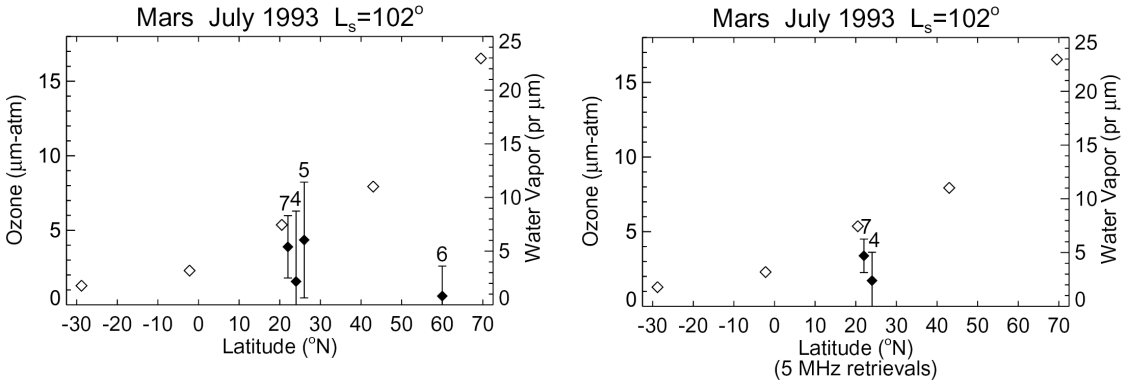


Figure 5.8. Total ozone column densities and 1σ uncertainties retrieved from 25 MHz (left) and 5 MHz (right) resolution infrared heterodyne spectra taken during 4-7 July 1993 at Ls=102°. Water vapor column densities from 3 June 1993 [Sprague *et al.* 1996, private communication] are shown as open diamonds. The limited data do not allow the study of behavior with latitude.

Table 5.4. Total ozone column densities and 1σ uncertainties retrieved from infrared heterodyne spectra taken during 4-7 July 1993 at Ls=102°.

Latitude (°N)	[O3] cm^{-2} (5 MHz)[a]	1σ uncertainty	[O3] cm^{-2} (25 MHz)[b]	1σ uncertainty	Day of Month
25	3.4	1.1	3.9	2.1	7
25	1.7	1.9	1.6	4.7	4
25	-	-	4.3	3.9	5
60	-	-	0.6	2.0	6

a Retrieval from 5 MHz resolution spectrum.
b Retrieval from 25 MHz resolution spectrum.

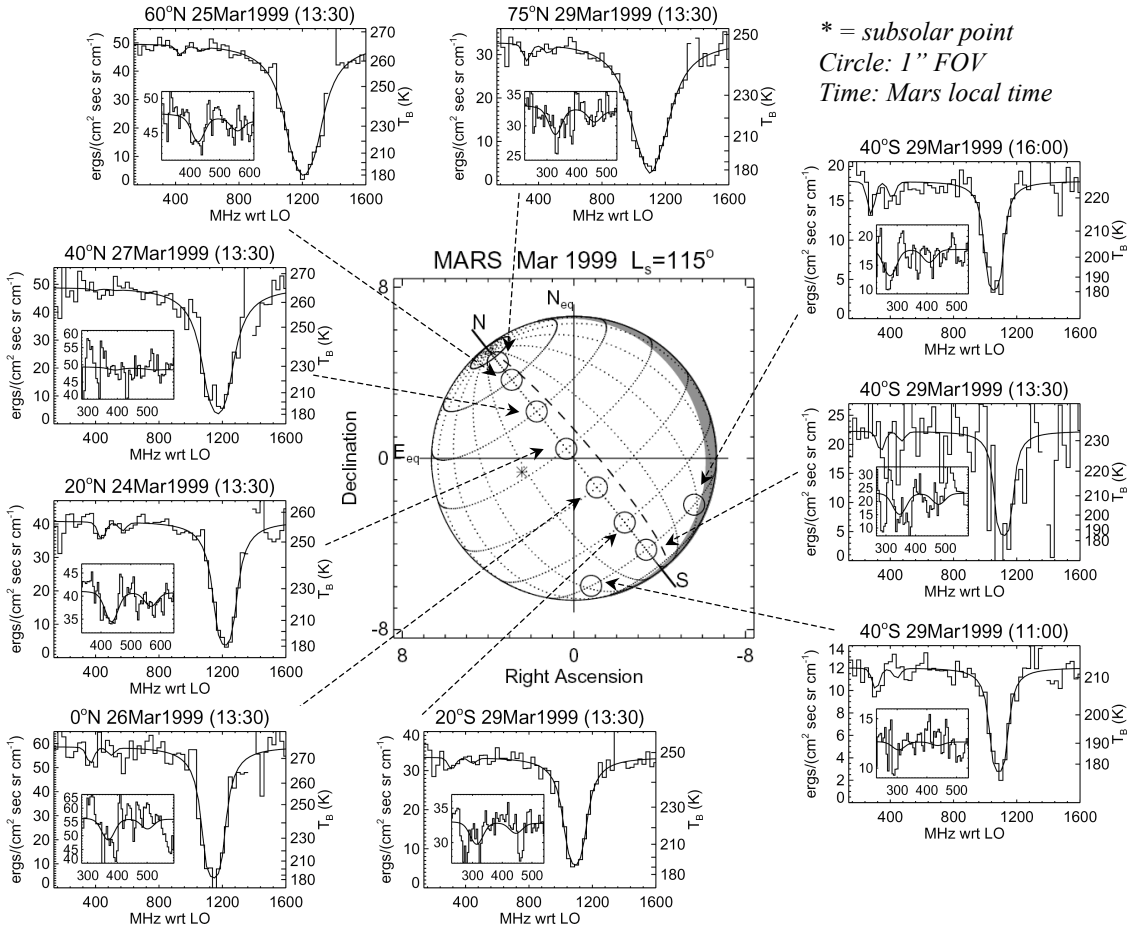
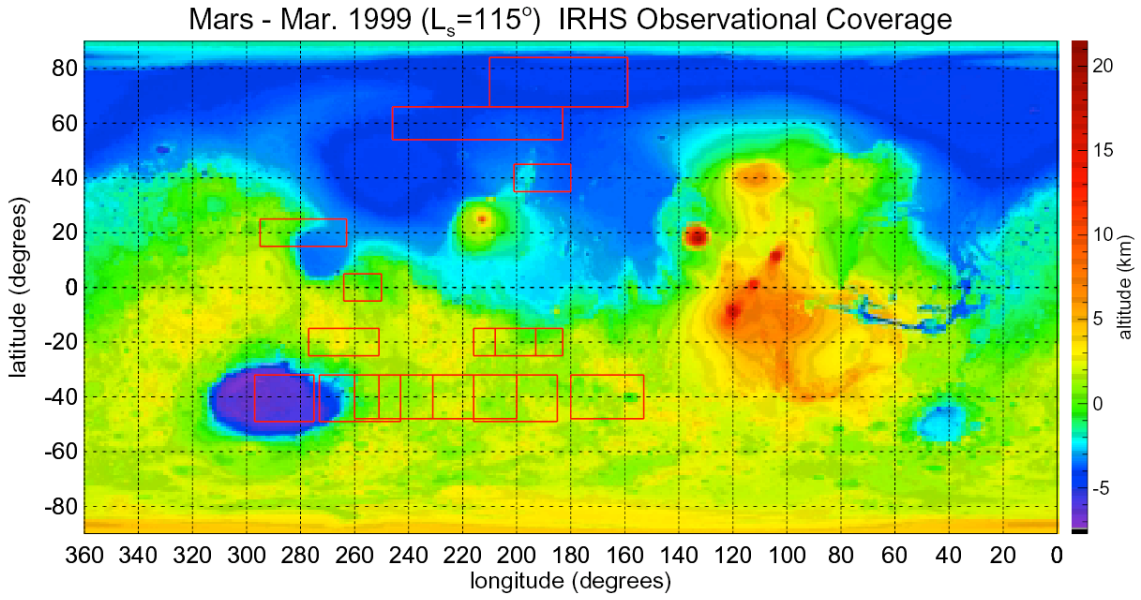


Figure 5.9. Martian observing geometry and heterodyne spectra (above) and observational coverage (below) from 24-29 March 1999, L_S=115°.



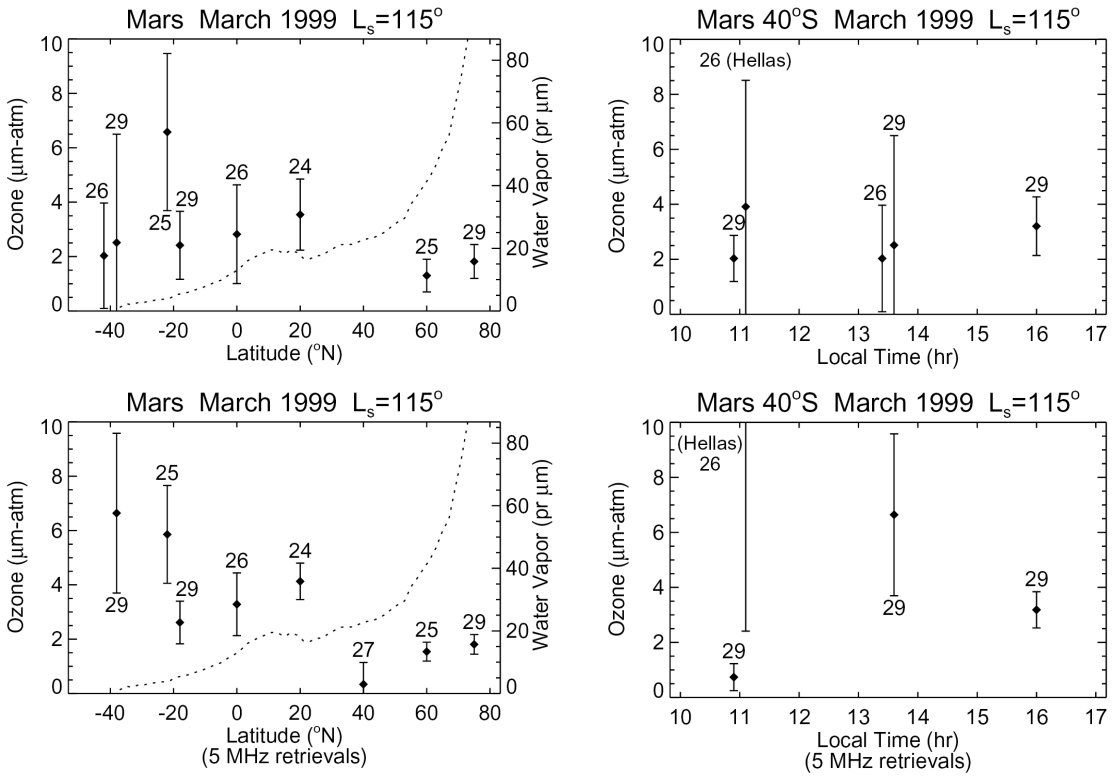


Figure 5.10. Total ozone column densities and 1σ uncertainties retrieved from 25 MHz (top left) and 5 MHz (bottom left) resolution infrared heterodyne spectra taken during 24-29 March 1999 at Ls=115°. The dotted curve indicates contemporaneous measurement of total water vapor column density [MGS-TES, Smith *et al.* 2004, private communication]. Ozone column densities retrieved at 40°S are displayed as a function of local time from 25 MHz (top right) and 5 MHz (bottom right) resolution spectra. No significant variation in ozone column density can be reliably inferred from the local times sampled (~5 hours).

Table 5.5. Total ozone column densities and 1σ uncertainties retrieved from infrared heterodyne spectra taken during 24-29 March 1999 at Ls=115°.

Latitude (°N)	[O3] cm^{-2} (5 MHz[a])	1σ uncertainty	[O3] cm^{-2} (25 MHz[b])	1σ uncertainty	Day of Month
-40	-	-	2.0	1.9	26
-40	6.6	2.9	2.5	4.0	29
-20	5.9	1.8	6.6	2.9	25
-20	2.6	0.8	2.4	1.2	29
0	3.3	1.2	2.8	1.8	26
20	4.1	0.7	3.5	1.3	24
40	0.3	0.8	-	-	27
60	1.5	0.3	1.3	0.6	25
75	1.8	0.4	1.8	0.6	29

a Retrieval from 5 MHz resolution spectrum.
b Retrieval from 25 MHz resolution spectrum.

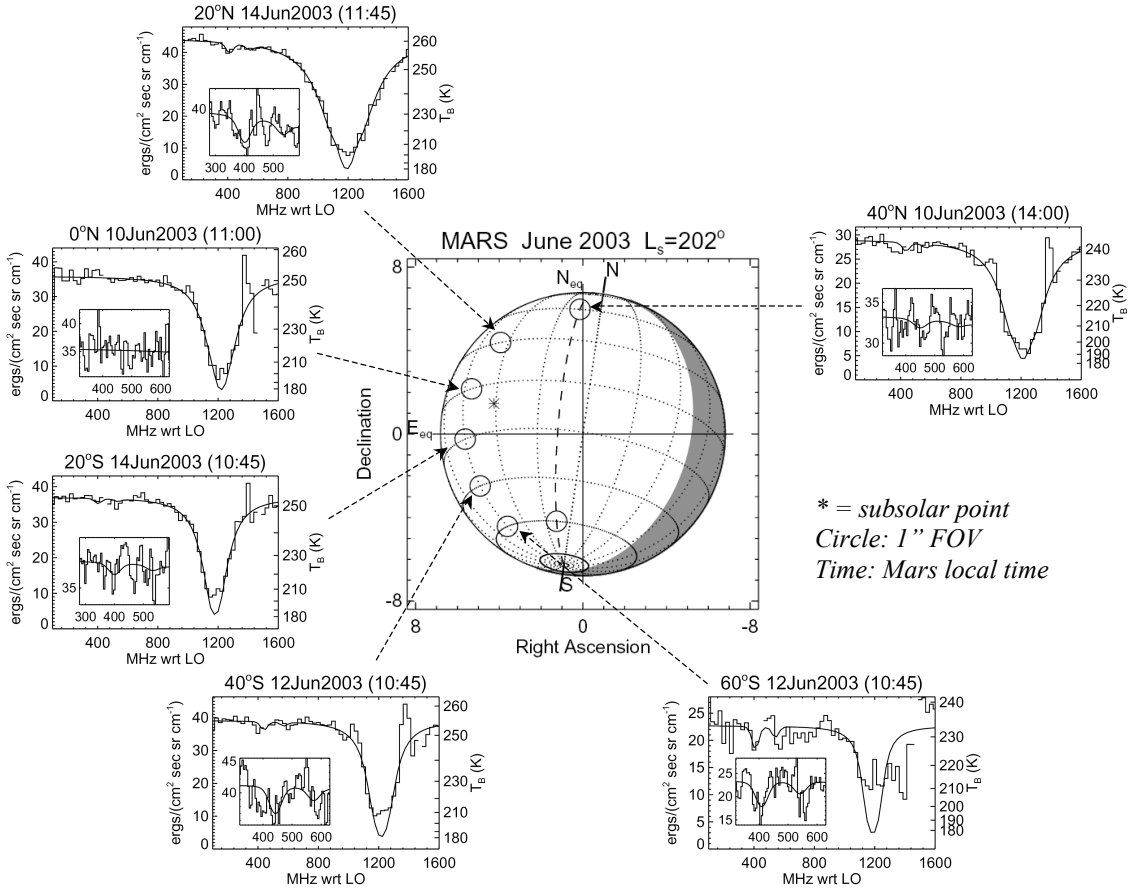
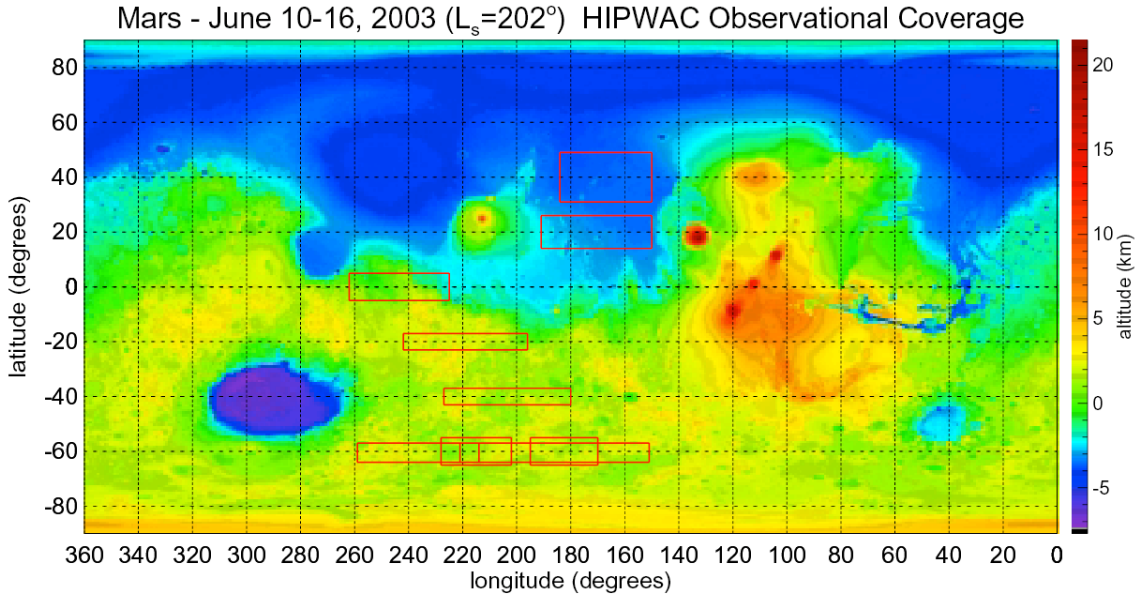


Figure 5.11. Martian observing geometry and heterodyne spectra (above) and observational coverage (below) from 10-16 June 2003, L_S=202°.



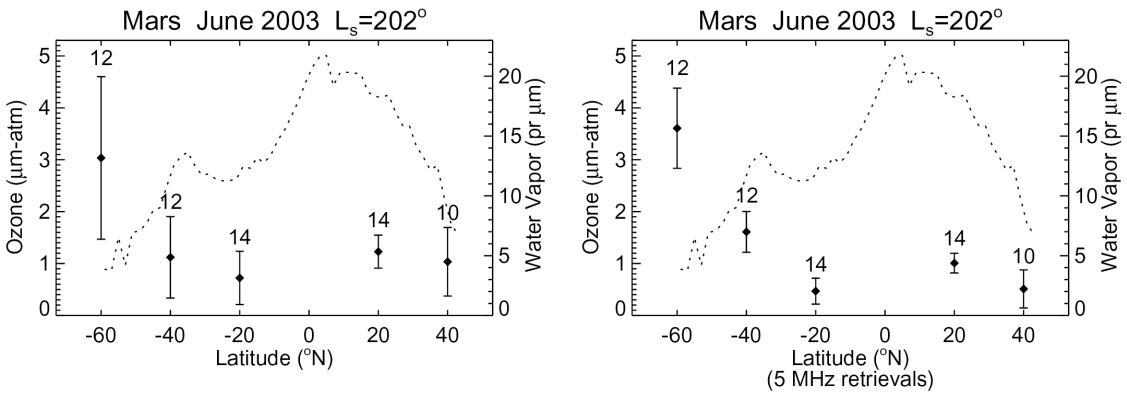


Figure 5.12. Total ozone column densities and 1σ uncertainties retrieved from 25 MHz (left) and 5 MHz (right) resolution infrared heterodyne spectra taken during 10-16 June 2003 at Ls=202°. The dotted curve indicates contemporaneous measurement of total water vapor column density [MGS-TES, Smith *et al.* 2004, private communication].

Table 5.6. Total ozone column densities and 1σ uncertainties retrieved from infrared heterodyne spectra taken during 10-16 June 2003 at Ls=202°.

Latitude (°N)	[O3] cm^{-2} (5 MHz[a])	1σ uncertainty	[O3] cm^{-2} (25 MHz[b])	1σ uncertainty	Day of Month
-60	3.6	0.8	3.0	1.6	12
-40	1.6	0.4	1.1	0.8	12
-20	0.5	0.3	0.7	0.5	14
20	1.0	0.2	1.2	0.3	14
40	0.5	0.4	1.0	0.7	10

a Retrieval from 5 MHz resolution spectrum.
b Retrieval from 25 MHz resolution spectrum.

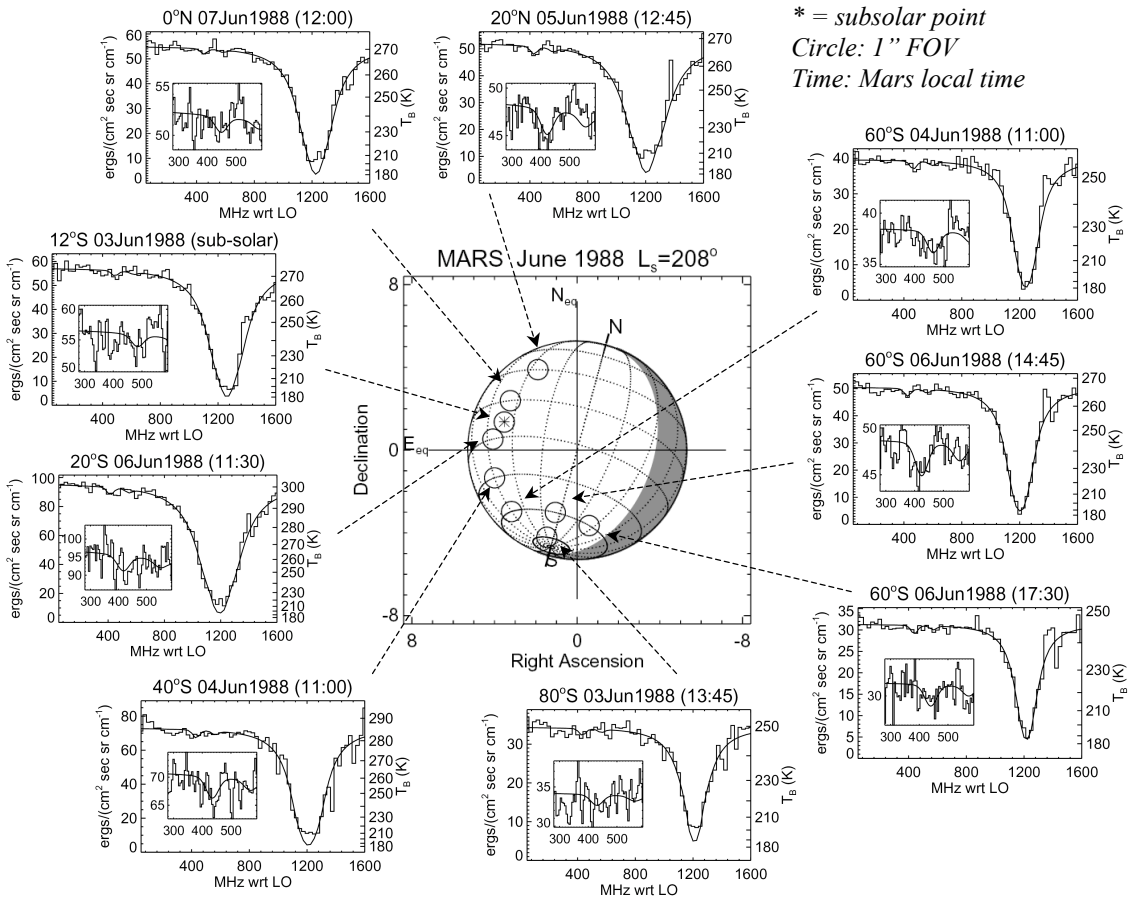
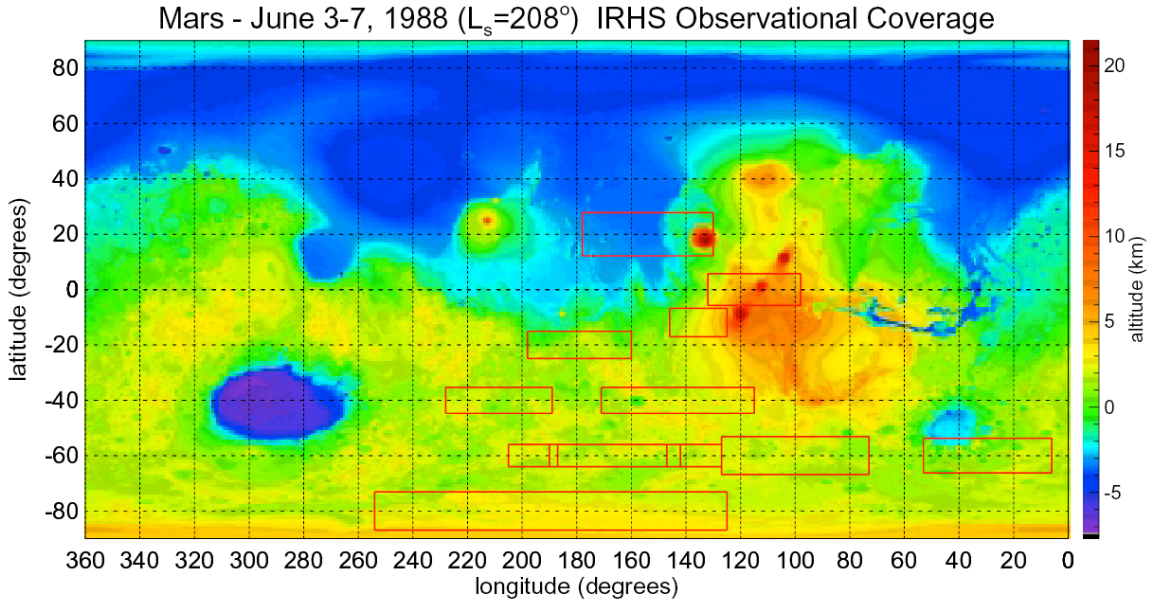


Figure 5.13. Martian observing geometry and heterodyne spectra (above) and observational coverage (below) from 3-6 June 1988, L_S=208°.



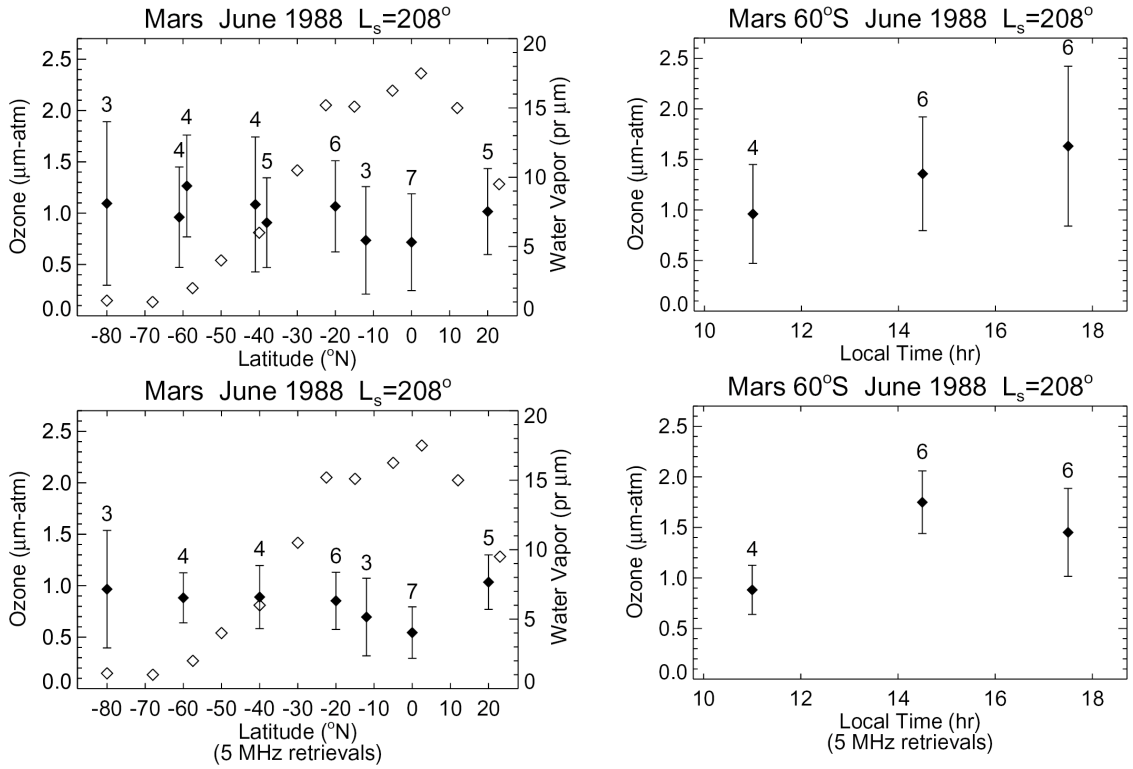


Figure 5.14. Total ozone column densities and 1σ uncertainties retrieved from 25 MHz (left) and 5 MHz (right) resolution infrared heterodyne spectra taken during 3-6 June 1988 at Ls=208°. Water vapor column densities from 04 June 1988 [Rizk *et al.* 1991] are shown as open diamonds. Ozone column densities retrieved at 60°S are displayed as a function of local time from 25 MHz (top right) and 5 MHz (bottom right) resolution spectra. No significant variation in ozone column density can be reliably inferred from the local times sampled (~7 hours).

Table 5.7. Total ozone column densities and 1σ uncertainties retrieved from infrared heterodyne spectra taken during 3-6 June 1988 at Ls=208°. Retrieved column densities are ~30% smaller than those from the analysis of Espenak *et al.* [1991]. This is due to warmer temperatures retrieved through an updated analysis technique more extensive than was available at that time of the earlier analysis.

Latitude (°N)	[O3] cm^{-2} (5 MHz)[a]	1σ uncertainty	[O3] cm^{-2} (25 MHz)[b]	1σ uncertainty	Day of Month
-80	1.0	0.6	1.1	0.8	3
-60	0.9	0.2	1.0	0.5	4
-60	-	-	1.3	0.5	4
-40	0.9	0.3	1.1	0.7	4
-40	-	-	0.9	0.4	5
-20	0.9	0.3	1.1	0.4	6
-12	0.7	0.4	0.7	0.5	3
0	0.5	0.3	0.7	0.5	7
20	1.0	0.3	1.0	0.4	5

a Retrieval from 5 MHz resolution spectrum.

b Retrieval from 25 MHz resolution spectrum.

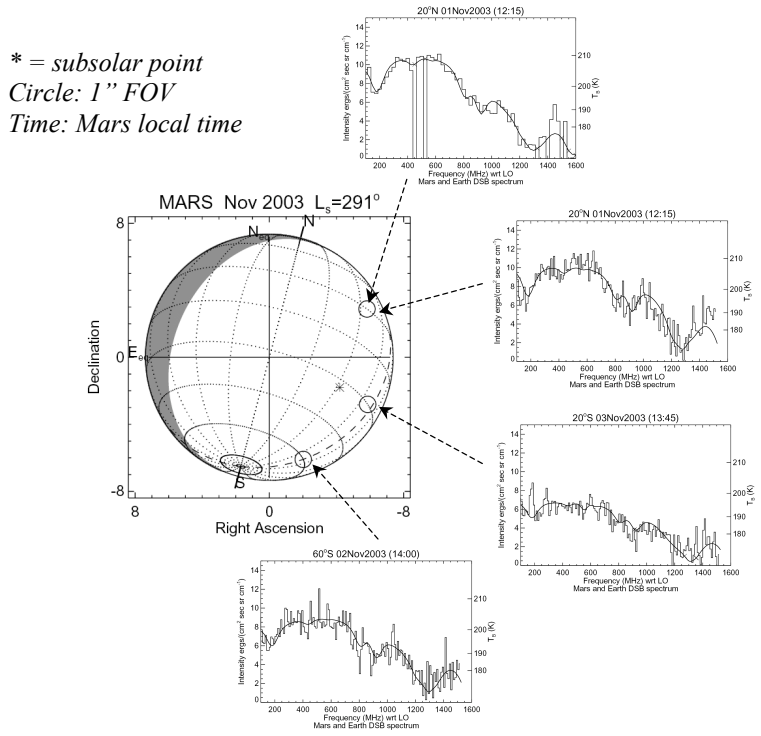
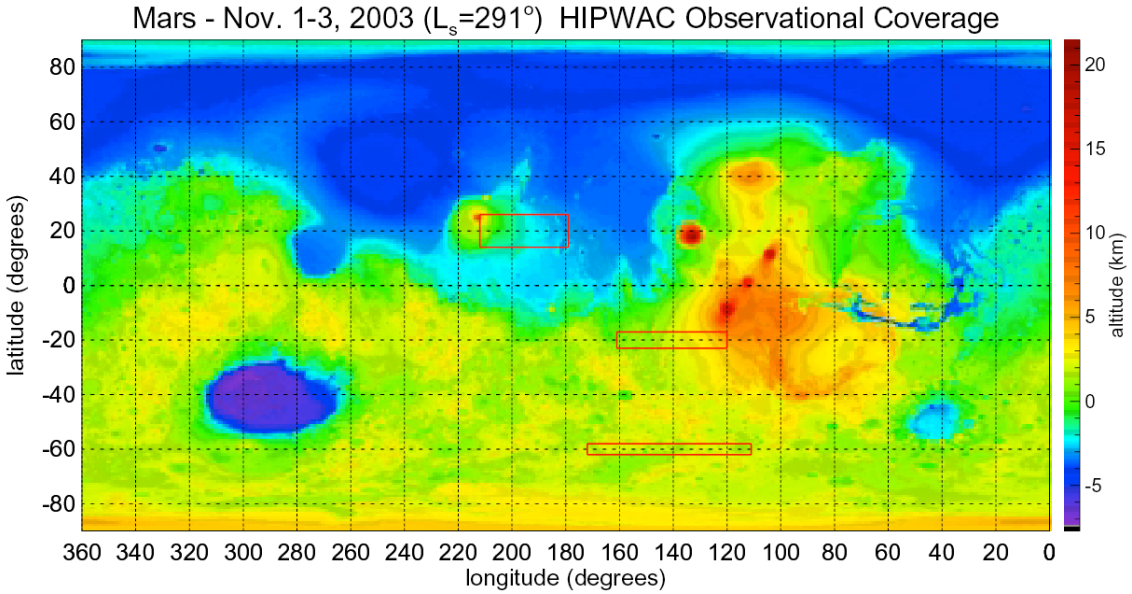


Figure 5.15. Martian observing geometry and heterodyne spectra (above) and observational coverage (below) from 1-3 November 2003, L_S=291°. Displayed spectra show contribution from both Earth and Mars, and only an upper limit retrieval for the ozone abundance was possible (~0.5 μm-atm).



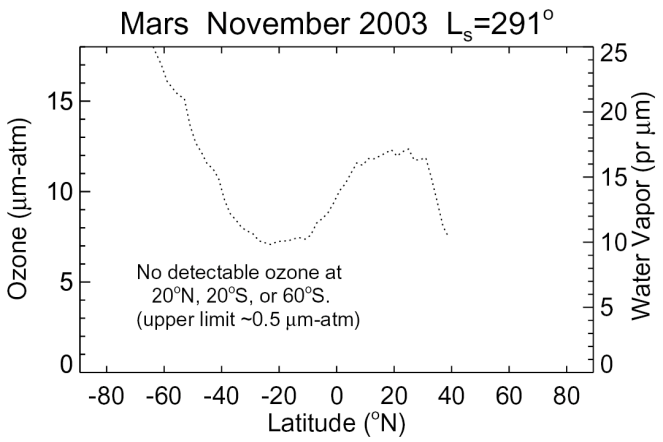


Figure 5.16. No ozone was detected in the infrared heterodyne spectra taken at 20°N, 20°S, and 60°S during 1-2 November 2003 at Ls=291°. An upper limit of ~0.5 μm-atm was inferred from the noise level. The dotted curve indicates contemporaneous measurement of total water vapor column density [MGS-TES, Smith *et al.* 2004, private communication].

IV. Spatial and Seasonal/Orbital Behavior of Ozone on Mars and the Anticorrelation of Total Ozone and Water Vapor Column Abundance

The ozone data sets range from pre-aphelion to post-perihelion (Fig. 1.1). The retrieved total ozone column densities show a general decline between L_S=40°-291° (preceding figures and tables). A decline in ozone abundance is expected from the photochemistry detailed in Ch. 1, which predicts that it should be anticorrelated with water vapor abundance. During the warmer perihelion seasons, more water vapor would be available as a source of odd hydrogen, which destroys ozone. During the colder aphelion seasons, water vapor would freeze out of the atmosphere and decrease odd hydrogen production.

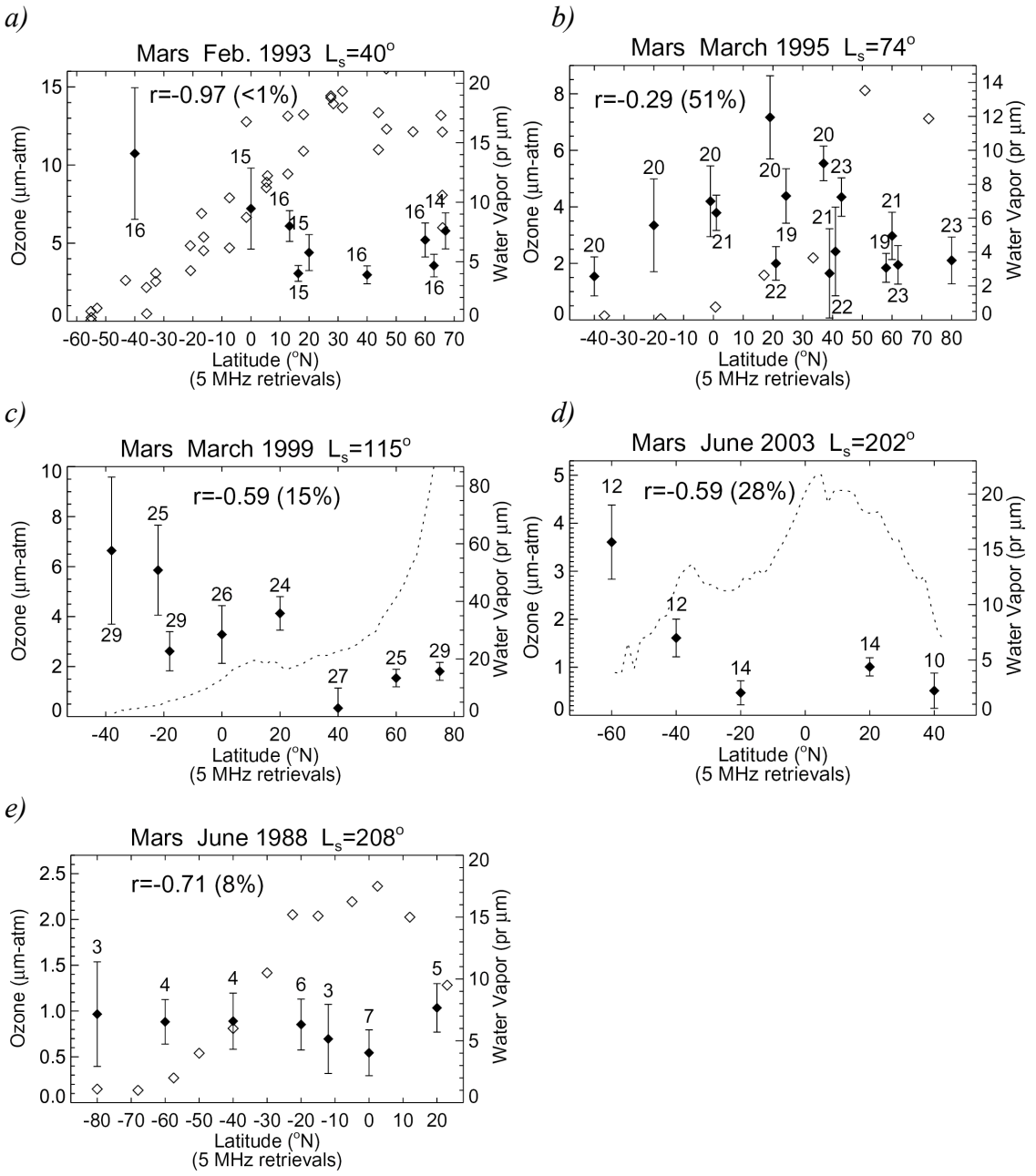


Figure 5.17. Ozone abundances and 1σ uncertainties retrieved from 5 MHz resolution infrared heterodyne spectra are displayed for periods with sufficient spatial coverage for investigating anticorrelation with water vapor abundance. Water vapor column densities are from Sprague *et al.* [1996, private communication] (panels *a* and *b*), MGS-TES, Smith *et al.* [2004, private communication] (panels *c* and *d*), and Rizk *et al.* [1991] (panel *e*). The correlation coefficient, r, between the ozone and water vapor column densities is indicated, along with the percent probability that uncorrelated values could produce that particular r value. The correlation coefficients between the total column densities are consistently negative, indicating anticorrelation, but are not all close to -1, indicating the need to consider the distribution of species within the column.

The decline in ozone column density between L_S=40° and 291° confirms in general the anticorrelation of ozone and water vapor predicted by photochemistry. However, a strict antcorrelation of total ozone and water vapor column density is not observed spatially. Figure 5.17 displays the 5 MHz resolution ozone retrievals shown in previous figures, along with water vapor column abundance, for periods with sufficient spatial coverage for investigating ozone/water anticorrelation. Correlation coefficients, r, between the ozone and water vapor column densities are noted on the plots, along with the percent probabilities that uncorrelated values could produce those correlation coefficients. The correlation coefficients between the total column densities are consistently negative, indicating anticorrelation. Not all of the correlation coefficients are close to -1, however, and an investigation of the altitude distribution of the species would help to understand the lack of strict anticorrelation of total column abundance.

Another way to investigate ozone/water anticorrelation is to look at the variation in the two constituents with orbital position (L_S) at particular latitudes. Ozone column densities from the latitudes investigated more than once in this work are displayed as functions of L_S in Fig. 5.18, along with orbital water vapor column densities from MGS-TES [Smith *et al*. 2004, private communication] and correlation coefficients. Again, the consistently negative correlation coefficients between the total column densities point to an anticorrelation of ozone and water vapor abundance. The correlation coefficients were not consistently close to -1, indicating the need to consider the distribution of the species within the column when investigating their chemistry.

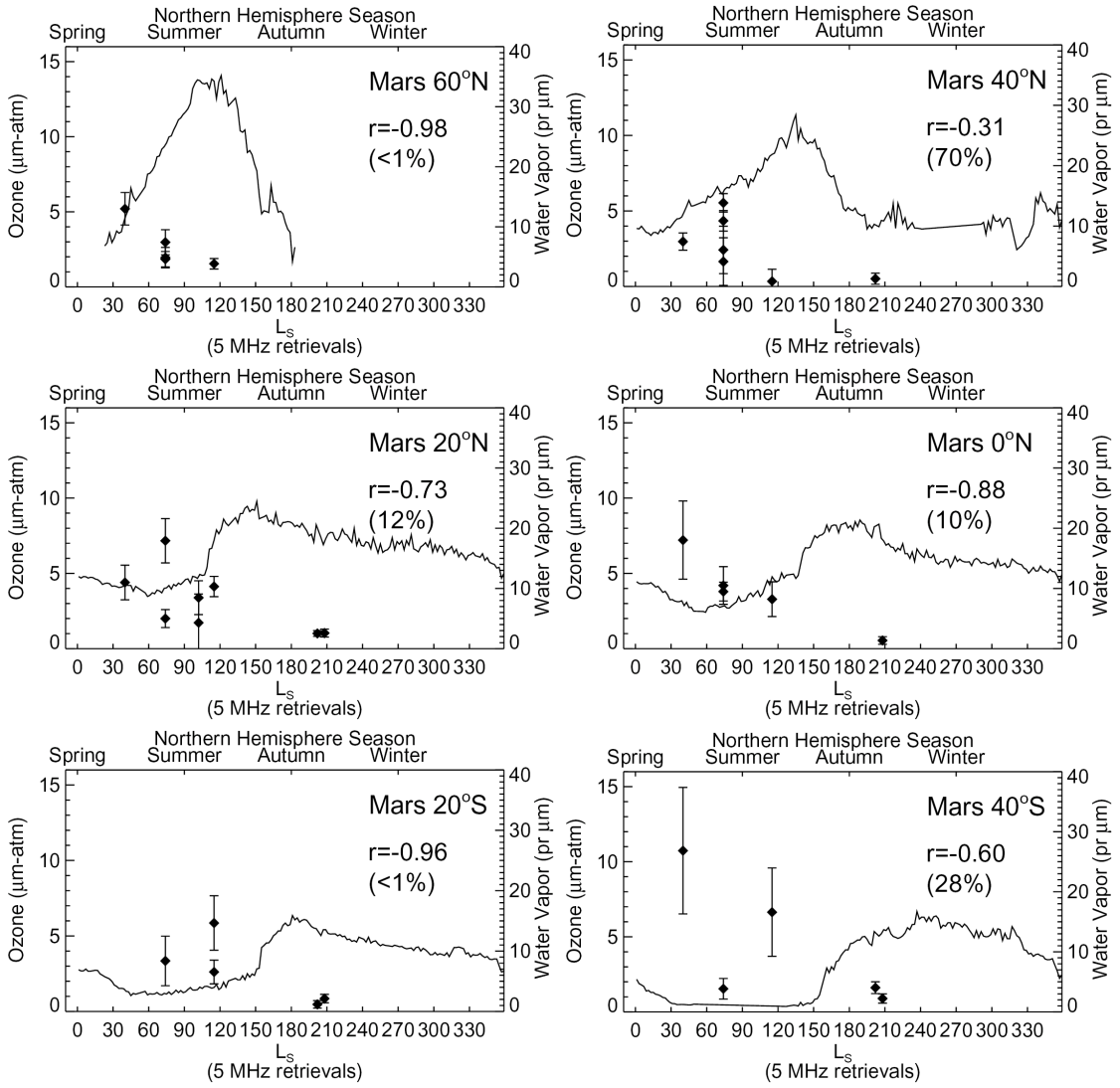


Figure 5.18. Total ozone column densities from this work at the latitudes indicated, as a function of L_S. The curve indicates measurement of total water vapor column density [MGS-TES, Smith *et al.* 2004, private communication] for Mars Year 26, which ran from mid-2002 to early 2004. This period was chosen because it is the only complete year (L_S=0°-360°) measured by MGS-TES without a global dust storm. The correlation coefficient, r, between the ozone and water vapor column densities is indicated, along with the percent probability that uncorrelated values could produce that particular r value. The correlation coefficients between the total column densities are consistently negative, indicating anticorrelation, but are not always close to -1, indicating the need to consider the distribution of species within the column.

The diurnal behavior of ozone was investigated on a few occasions (L_S=74° at 60°N in Fig. 5.6, L_S=115° at 40°S in Fig. 5.10, and L_S=208° at 60°S in Fig. 5.13). The interval of daytime local times ranged from 4 to 7.5 hours, and no significant variation in ozone abundance was seen over those periods.

Here, total column densities were compared in order to investigate orbital/seasonal variation and the ozone/water anticorrelation predicted by photochemistry. Some orbital and spatial anticorrelation is observed, but the ozone column density variations observed do not reflect the large variations seen in water vapor column density. Clancy & Nair [1996] used a seasonal photochemical model to investigate ozone abundance at 20 and 40 km altitude. They found that the modeled variation in ozone number density at those altitudes is much greater than that of the total ozone column. This is attributed to the variation the altitude of the water vapor saturation altitude, or "hygropause". During cooler aphelion seasons, the hygropause is lower (10-15 km), and therefore ozone abundance at the higher altitudes can increase in the absence of large amounts of odd hydrogen. During warmer perihelion seasons, the hygropause rises, (~40 km) providing a source of odd hydrogen that can destroy ozone at the higher altitudes. Therefore, the altitude distribution of water vapor must be considered when explaining ozone behavior, and this issue will be further discussed in the context of photochemical modeling in Ch. 8. The altitude distribution of ozone will be explored observationally in Ch. 6.

Chapter 6: Investigating the Altitude Distribution of Ozone on Mars Using Total Ozone Column Abundance and $O_2(^1\Delta)$ Dayglow Intensities

I. $O_2(^1\Delta)$ Dayglow Intensity and Ozone Abundance and Distribution

An indirect probe of high altitude ozone (>20 km) is emission from excited molecular oxygen resulting from ozone photolysis. Ozone is dissociated by solar UV radiation:

$$O_3 + h\nu = O_2(^1\Delta) + O(^1D) \tag{6.1}$$

The excited metastable oxygen molecule will emit a 1.27 μm photon ($^1\Delta_g \rightarrow {}^3\Sigma_g^-$) if it not first "quenched" by colliding with another molecule. This dayglow emission can be used as a tracer of its ozone parent for altitudes above ~20 km where collisional de-excitation is no longer dominant.

The $O_2(^1\Delta)$ dayglow emission was first directly observed by Noxon *et al.* [1976]. Dayglow mapping studies have been conducted in recent years [Krasnopolsky and Bjoraker 2000, Novak *et al.* 2002, Krasnopolsky 2003*a*]. Observations of the emission are important for studying the seasonal/orbital behavior of high altitude ozone and, combined with total ozone column densities, can probe the altitude distribution of ozone in the atmosphere of Mars.

The amount of photolyzed ozone can be related to the amount of the resulting excited molecular oxygen that either radiates 1.27 μm photons or is quenched by collisions ($cm^{-2}\ s^{-1}$):

$$J[O_3] = [O_2(^1\Delta)]\left(\tau^{-1} + k_C[CO_2]\right) \tag{6.2}$$

The bracketed quantities are the column densities of the species. The ozone photolysis rate is J (which changes with heliocentric distance), τ is the lifetime of the resulting $O_2(^1\Delta)$ state, and k_C is the rate of collisional de-excitation of $O_2(^1\Delta)$ on CO_2 (other molecules are negligible). Rearranging the terms results in an expression relating the dayglow intensity to the total ozone column density:

$$4\pi I(MR) = \frac{10^{-12}[O_2(^1\Delta)]}{\tau} = \frac{10^{-12} J[O_3]}{\left(1 + k_C \tau [CO_2]\right)} \tag{6.3}$$

The 10^{-12} and 4π terms provide the conversion from photons cm^{-2} s^{-1} $(4\pi \text{ ster})^{-1}$ to MegaRayleighs (MR or $10^{12}/4\pi$ photons cm^{-2} s^{-1} $ster^{-1}$). If the density is such that the collisional component can be neglected ($k_C \sim 0$), then the amount of ozone whose $O_2(^1\Delta)$ daughters survive to emit 1.27 μm photons can be related to dayglow intensity by:

$$4\pi I(\text{MR}) = 10^{-12} J[O_{3h}] \tag{6.4}$$

where $[O_{3h}]$ (notation from Krasnopolsky [2003*a*]) is the column of that high altitude ozone that is probed by the dayglow. Krasnopolsky [2003*a*] used updated ozone photolysis rate and quantum yield to determine a value of 0.0077 s^{-1} for J at 1 AU. His expression relating dayglow intensity to high altitude ozone column abundance (scaling J at 1 AU by r^2, where r is the heliocentric distance in AU, and multiplying by 2.7×10^{15} to convert from cm^{-2} to μm-atm) is:

$$4\pi I(\text{MR}) = \frac{20.8[O_{3h}]}{r^2} \tag{6.5}$$

Because the boundary where collisions can be neglected is not well defined and because it is not clear as to what percentage of the total column abundance $[O_{3h}]$ represents, it is useful to relate the dayglow intensity directly to the total ozone column

density. Krasnopolsky [2003*a*] integrated different ozone distributions through the atmosphere to relate dayglow intensity to ozone column density:

$$4\pi I(\mathrm{MR}) = \frac{10^{-12} J}{r^2} \int_0^\infty \frac{[\mathrm{O}_3]dx}{1 + k_C \tau [\mathrm{CO}_2]} \tag{6.6}$$

The equation was numerically integrated assuming a constant ratio of ozone scale height to that of the rest of the atmosphere to yield an expression relating that scale height ratio to the dayglow intensity for that possible ozone distribution:

$$4\pi I(\mathrm{MR}) = 5.2[\mathrm{O}_3](\mathrm{H}_{\mathrm{O}_3}/\mathrm{H})^{0.63} r^{-2} \tag{6.7}$$

Unlike Eq. 6.5, this expression takes into account collisions and relates the dayglow intensity to the total column density of ozone. Another possible atmospheric model was integrated assuming a constant-with-height ozone mole fraction distribution at lower altitudes ($[O_{3l}]$) and an excess component of ozone at high altitudes ($[O_{3e}]$):

$$4\pi I(\mathrm{MR}) = (5.2[\mathrm{O}_{3l}] + 20.8[\mathrm{O}_{3e}])r^{-2} \tag{6.8}$$

The first, low altitude (<20 km) term is essentially Eq. 6.7 ($H_{O3}/H=1$) where collisional quenching was included in the integration. The second, high altitude (>20 km) term is Eq. 6.5, where collisions were neglected.

The total ozone column in Eq. 6.7 can be supplied by that obtained from the radiative transfer analysis of a heterodyne ozone spectrum. Using a dayglow intensity from the same Martian orbital period (L_S), a scale height ratio can be retrieved (Eq. 6.7), which can be converted to an ozone mole fraction profile.

Hydrostatic equilibrium relates pressure (P) and height (z):

$$\frac{dP}{dz} = -\rho g = -\mu m_{\mathrm{H}} n g \tag{6.9}$$

where ρ is mass density, g is acceleration due to gravity, μ is the mean molecular weight of the atmosphere in atomic mass units, m_{H} is the mass of the hydrogen atom, and n is number density. The ideal gas law relates pressure, temperature (T) and number density:

$$P = nkT \tag{6.10}$$

where k is Boltzmann's constant. Combining these two equations, assuming an isothermal atmosphere and integrating yields:

$$P = P_0 e^{-\frac{z-z_0}{\mathrm{H}}} \tag{6.11}$$

or

$$n = n_0 e^{-\frac{z-z_0}{\mathrm{H}}} \tag{6.12}$$

which relates pressure (or number density) and height in terms of the scale height of the atmosphere:

$$\mathrm{H} = \frac{kT}{\mu m_{\mathrm{H}} g} \tag{6.13}$$

This expression applies to the total atmosphere, not to an individual atmospheric component such as ozone. The scale height is a function of temperature and the mean molecular weight in a particular altitude region. Over regions where those values do not vary greatly, the scale height is assumed to be constant. The typical scale height (lower atmosphere) for Mars is 11 km and for Earth is 8.5 km.

The assumption of different scale heights for ozone and the total atmosphere and the ratio of their two number densities (using Eq. 6.12) yield an expression for the ozone mole fraction profile in terms of the scale height ratio:

$$x_{\mathrm{O_3}}(z) = x_{\mathrm{O_3}}(z_0) e^{-\frac{(z-z_0)}{\mathrm{H}}\left(\frac{\mathrm{H}}{\mathrm{H_{O_3}}}-1\right)} \tag{6.14}$$

Applying the ozone mole fraction profile (Eq. 6.14) to the total number density profile (Eq. 6.12) and integrating over all altitudes yields an expression for total ozone column density:

$$[O_3] = \frac{P_0 x_{O_{3_0}} \frac{H_{O_3}}{H}}{\mu m_H g} \tag{6.15}$$

Column densities retrieved in this manner are based on the assumption of a particular ozone distribution (scale height ratio and ozone mole fraction).

II. Retrievals of Ozone Altitude Distribution Using Heterodyne Ozone Retrievals and $O_2(^1\Delta)$ Dayglow Measurments

The methods of Krasnopolsky [2003*a*] for retrieving information on ozone distribution (Eqs. 6.7 and 6.8) are applied using ozone column abundances from this work and measurements of $O_2(^1\Delta)$ dayglow intensity.

The scale height ratio model of Eq. 6.7 is applied by combining a total ozone column density from a heterodyne measurement with a measured dayglow intensity and then retrieving a scale height ratio. A new mole fraction profile is constructed (Eq. 6.14) and then scaled in a new radiative transfer fit of the spectrum. This yields a new column density (Eq. 6.15) that is combined with the dayglow intensity to yield a new scale height ratio. These steps are iterated until convergence.

The high altitude excess model of Eq. 6.8 can also be applied by combining heterodyne and dayglow measurements. The retrieved ozone column density from heterodyne measurements, $[O_3]$, probes both components of that model distribution:

$$[O_3] = [O_{3l}] + [O_{3e}] \tag{6.16}$$

With two equations (Eqs. 6.8 and 6.16) and two unknowns, the heterodyne column densities and the dayglow intensities can be combined to test this possible distribution.

$$[O_{31}] = \tfrac{4}{3}[O_3] - 0.0641 \cdot 4\pi I(\mathrm{MR}) r^2 \tag{6.17}$$

$$[O_{3e}] = 0.0641 \cdot 4\pi I(\mathrm{MR}) r^2 - \tfrac{1}{3}[O_3] \tag{6.18}$$

These two altitude distribution models were tested using the heterodyne data sets that were taken either close in time to a dayglow data set or during a similar orbital period (L_S). As with the ozone measurements in this work, $O_2(^1\Delta)$ dayglow intensity measurements were made at the NASA Infrared Telescope Facility on Mauna Kea. The facility echelle spectrometer CSHELL was used, and details about observations made with this instrument can be found in Krasnopolsky and Bjoraker [2000] and Novak *et al*. [2002]. The results of the ozone altitude analysis are presented here, and they are discussed further in the context of expectations from photochemical models in Ch. 8.

A. Investigating Ozone Altitude Distribution During Late Northern Spring

An ozone altitude distribution analysis was performed for the Martian season of late northern spring, near aphelion. In this case, ozone and $O_2(^1\Delta)$ measurements were made in different years (Table 6.1). The results are presented in Table 6.2. This heterodyne data set contained many spectra, but the integrations times were relatively short, resulting in lower signal-to-noise and scattered abundance retrievals. The altitude retrievals are also scattered, but in general they agree with the presence of a high altitude excess of ozone, and the retrieved scale height ratios (H_{O3}/H) tend to be greater than unity. As with the Earth's stratosphere, variations from a scale height ratio of 1 are due

to the local production (and destruction) of ozone resulting from photolyzing radiation and the abundances of participating species (e.g. atomic oxygen, odd hydrogen, see Ch.1).

Table 6.1. Observations during late northern spring on Mars.

Measurement	Ls	Date (UT)	Reference
$O_2(^1\Delta)$	67°	20 January 1997	Krasnopolsky 2003*a*
O_3	74°	19-23 March 1995	this work

Table 6.2. Ozone altitude distribution results (late northern spring)

Latitude	$[O_3]^a$ (μm-atm)	$O_2(^1\Delta)$ $4\pi I^b$ (MR)	inferred $[O_3]^c$ (μm-atm)	High Altitude Excess Model[d] $[O_{3l}]$ (μm-atm)	$[O_{3e}]$ (μm-atm)	Scale Height Ratio Model[e] H_{O3}/H	$[O_3]$ (μm-atm)
40°S	1.5±0.7	7.5	4.0	0.7±0.9	0.8±0.2	6.2	1.1±0.5
20°S	3.3±1.6	7.5	4.0	3.1±2.1	0.2±0.5	2.1	2.4±1.3
0°	4.2±1.2	8.0	4.3	4.2±1.7	0.0±0.4	0.6	5.4±1.9
0°	3.8±0.6	8.0	4,3	3.6±0.8	0.2±0.2	1.2	3.6±0.5
24°N	4.4±1.0	7.0	3.7	4.6±1.3	-0.2±0.3	0.4	6.5±1.2
40°N	1.6±1.6	5.5	2.9	1.2±2.1	0.4±0.5	6.4	0.8±1.0
40°N	4.3±0.7	5.5	2.9	4.8±0.9	-0.5±0.2	0.3	6.3±1.0
60°N	1.8±0.5	6.0	3.2	1.4±0.7	0.4±0.2	4.7	1.2±0.3
60°N	1.9±0.7	6.0	3.2	1.5±0.9	0.4±0.2	5.5	1.1±0.4
80°N	2.1±0.8	6.5	3.5	1.6±1.1	0.5±0.3	3.6	1.5±0.5

a This work, 19-23 March 1995, L_S=74°
b Krasnopolsky [2003*a*], 20 January 1997, L_S=67°
c Eq. 6.7, H_{O3}/H=1
d Eq. 6.17 and 6.18
e Eq 6.7 and 6.15

An altitude analysis was performed by Krasnopolsky [2003*a*] using these same dayglow intensities (i.e. Table 6.2) and total ozone column abundances from ultraviolet measurements at L_S=61° and 64° made by Clancy et al. [1999]. The column abundances from ultraviolet measurements are consistent with those from this work at L_S=74° (Ch. 7). The altitude analysis was performed using an average column density from

ultraviolet measurements between 0° and 40°N. The results show a small high altitude excess ($[O_l]$=2.1 μm-atm and $[O_e]$=0.4 μm-atm) as well as H_{O3}/H=1.1. This is consistent with results in Table 6.5, which were treated individually and not averaged over latitude. Krasnopolsky [2003*a*] also derives a scale height ratio of H_{O3}/H=0.6 for Mariner 9 ozone data around 80°N at L_S=67°, which was seen as a dramatic change from the lower latitude and interpreted to indicate different photochemistry and dynamics in the polar region. This is generally not seen in Table 6.5, where most scale height ratios are greater unity, although the values and uncertainties are high. In the three-dimensional photochemical model of Lefèvre *et al.* [2004], dynamical effects at polar latitudes are large due to the polar vortex, and large variation in ozone abundance is expected at those latitudes.

B. Investigating Ozone Altitude Distribution During Early Northern Summer

The preferred situation is listed in Table 6.3, where $O_2(^1\Delta)$ dayglow measurements were contemporaneous with the heterodyne ozone measurements during early northern summer on Mars. The investigation of altitude distribution was performed with dayglow intensities taken from Fig. 8 in Krasnopolsky [2003*a*], and the results are presented in Table 6.4.

Table 6.3. Observations during early northern summer on Mars.

Measurement	Ls	Date (UT)	Reference
$O_2(^1\Delta)$	112°	20 March 1999	Krasnopolsky 2003*a*
$O_2(^1\Delta)$	113°	23 March 1999	R. E. Novak *private communication*
O_3	115°	24-27, 29 March 1999	this work

The high altitude excess model was applied as explained earlier (Eqs. 6.17 and 6.18). Uncertainties are calculated from those of the retrieved total ozone column densities. The uncertainties on the retrievals of $[O_{3e}]$ are not insignificant, but all of the results consistently yield negative abundances, indicating the absence of a layer of excess ozone at high altitude. The scale height ratio iterative analysis was applied as described earlier. The fits to the spectra consistently yielded $H_{O3}/H<1$, meaning that ozone abundance falling off quicker with height than the rest of the atmosphere is an acceptable model as far as the heterodyne data are concerned, which also points away from the presence of a high altitude ozone layer. The best signal-to-noise on the ozone features was found at 60°N and 75°N.

Table 6.4. Ozone altitude distribution results (early northern summer)

Latitude	$[O_3]^a$ (μm-atm)	$O_2(^1\Delta)$ $4\pi I^b$ (MR)	inferred $[O_3]^c$ (μm-atm)	High Altitude Excess Model[d] $[O_{3l}]$ (μm-atm)	$[O_{3e}]$ (μm-atm)	Scale Height Ratio Model[e] H_{O3}/H	$[O_3]$ (μm-atm)
20°S	5.9±2.8	3.0	1.5	7.3±2.4	-1.4±0.6	0.09	7.3±3.3
20°S	2.6±0.8	3.0	1.5	3.0±1.0	-0.4±0.3	0.32	3.3±0.9
0°	3.3±1.1	4.0	2.0	3.7±1.5	-0.4±0.4	0.34	4.0±1.5
20°N	4.1±0.7	3.5	1.8	4.9±0.9	-0.8±0.2	0.19	5.2±0.9
60°N	1.5±0.3	2.5	1.3	1.6±0.5	-0.1±0.1	0.58	1.7±0.4
75°N	1.8±0.4	2.0	1.0	2.1±0.5	-0.3±0.1	0.48	2.0±0.4

a This work, 24-27, 29 March 1999, $L_S=115°$
b Krasnopolsky [2003*a*], 20 March 1999, $L_S=112°$
c Eq. 6.7, $H_{O3}/H=1$
d Eq. 6.17 and 6.18
e Eq 6.7 and 6.15

After this analysis was completed, the dayglow intensities from the other contemporaneous observing run became available [R. E. Novak, private communication]. They are displayed in Table 6.5, and they are quite low compared to those taken a few days earlier (Table 6.4). When dayglow emission is strong, extraction of dayglow

intensity from the oxygen spectra are consistent between the investigators, but during periods of reduced dayglow emission (L_S > 100°), intensity retrieval becomes difficult and sensitive to the extraction method used [V. A. Krasnopolsky, private communication]. The low intensities in Table 6.5 are still consistent with the lack of a high altitude excess shown in Table 6.4.

Table 6.5. Dayglow intensities from L_S=113°

Latitude	$[O_3]^a$ (μm-atm)	$O_2(^1\Delta)$ $4\pi I^b$ (MR)	inferred $[O_3]^c$ (μm-atm)
20°S	5.9±2.8	0.7±0.4	0.4±0.2
20°S	2.6±0.8	0.7±0.4	0.4±0.2
0°	3.3±1.1	≤0.5	≤0.2
20°N	4.1±0.7	≤0.5	≤0.2
60°N	1.5±0.3	1.4±0.4	0.7±0.2
75°N	1.8±0.4	1.5±0.2	0.8±0.1

a This work, 24-27, 29 March 1999, L_S=115°
b R. E. Novak [private communication], 23 March 1999, L_S=113°
c Eq. 6.7, H_{O3}/H=1

An ozone profile (Fig. 6.1) was calculated for this period (L_S=112°) at 20°N by V. A. Krasnopolsky [private communication] taking into account MGS TES temperature, water, and dust opacity data for March 20, 1999 (water = 18.6 pr. μm, dust opacity =0.1) [Smith 2004]. The photochemical model assumed a heterogeneous sink of H_2O_2 onto ice particles (probability of 0.002). The total ozone column abundance is 2 μm-atm (about half that measured in this work), the modeled dayglow intensity is 3.9 MR (consistent with measurement in Table 6.2), and H_2O_2 abundance is 5 ppb (consistent with the upper limit at the same orbital period from Encrenaz *et al*. [2004]). Additional background on photochemical modeling is presented in Ch. 8.

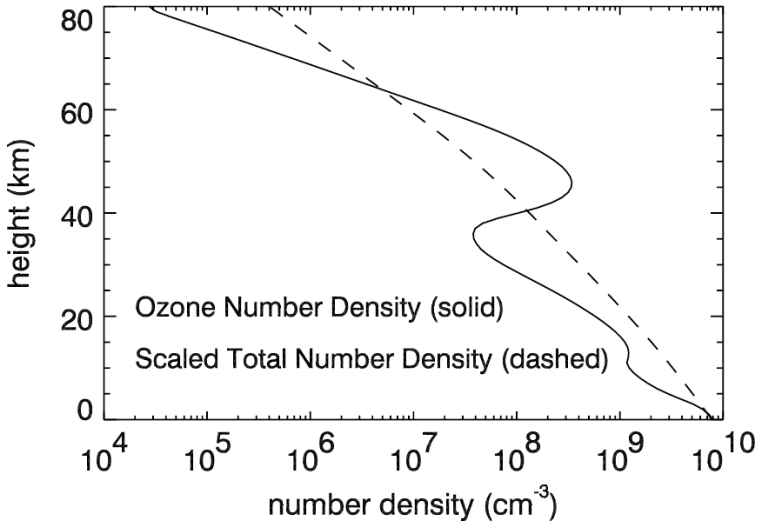


Figure 6.1. Ozone profile (solid) for L_S=112° from Krasnopolsky [private communication]. Additional information on the model is given in the text. The overlay of the scaled total atmosphere number density profile (dashed) illustrates that ozone has a smaller scale height in this model (i.e. number density falls off at a faster rate than that of the rest of the atmosphere), except between 40 and 60 km where excess abundance appears.

The modeled ozone profile in Fig. 6.1 falls off in number density below ~40 km quicker than that of the rest of the atmosphere, meaning that H_{O3}/H is less than unity, as was found in the scale height study for this period (Table 6.2). However, the high altitude excess study in Table 6.2 did not indicate the presence of a layer, and one does appear in Fig. 6.1. The high altitude excess model assumes that $H_{O3}/H=1$ at low altitudes and that an excess appears at high altitudes. The model in Fig. 6.1 shows a low altitude component where $H_{O3}/H<1$ as well as the high altitude excess. It is possible that the assumptions of the high altitude excess study did not yield a layer because the measured total column density and dayglow intensity could be matched just as well by an ozone distribution with $H_{O3}/H=1$ and no excess, as with a distribution like Fig. 6.1. The consistent negative excesses retrieved in the study may be indicating the need for a distribution with $H_{O3}/H<1$, rather than the absence of a high altitude excess altogether.

Also, the measured ozone column density was about twice that of the modeled profile in Fig. 6.1, while the measured dayglow intensity matched that of the model. Therefore, the high altitude ozone probed by the dayglow intensity is less significant relative to the observed column density than to the modeled column density, still supporting no excess of high altitude ozone.

An early northern summer period that preceded the one just discussed by ~10° in L_S was investigated using the heterodyne ozone measurements from July 1993. Because of the small Martian diameter and limited observations, only one spectrum was suited to an altitude distribution study (Table 6.6). The results (Table 6.7) do not appear to support a high altitude excess of ozone, but the uncertainties do not exclude the possibility, and the amount of data is not sufficient to properly address the question.

Table 6.6. Observations during early northern summer on Mars.

Measurement	Ls	Date (UT)	Reference
$O_2(^1\Delta)$	103°	14 January 2001	R. E. Novak *private communication*
O_3	102°	7 July 1993	this work

Table 6.7. Ozone altitude distribution results (early northern summer)

Latitude	$[O_3]^a$ (μm-atm)	$O_2(^1\Delta)$ $4\pi I^b$ (MR)	inferred $[O_3]^c$ (μm-atm)	High Altitude Excess Model[d] $[O_{3l}]$ (μm-atm)	$[O_{3e}]$ (μm-atm)	Scale Height Ratio Model[e] H_{O3}/H	$[O_3]$ (μm-atm)
25°N	3.4±1.1	5.6±0.5	2.9±0.3	3.6±1.5	-0.2±0.4	0.7	3.8±1.3

a This work, 7 July 1993, L_S=102°
b R. E. Novak [private communication], 14 January 2001, L_S=103°
c Eq. 6.7, H_{O3}/H=1
d Eq. 6.17 and 6.18
e Eq 6.7 and 6.15

C. Investigating Ozone Altitude Distribution During Early Northern Winter

A final comparison can be made by noting that during early northern winter at L_S=291° (Nov. 2003) in this work, no ozone absorption was detected (upper limit ~0.5 μm-atm). At Ls=306° (Jan. 2002), no $O_2(^1\Delta)$ dayglow emission was detected [R. E. Novak, private communication]. Low ozone abundance as well as very low abundance at high altitudes is consistent with the abundance and distribution of ozone expected by photochemistry at this perihelion period at latitudes visible from Earth, and this will be further discussed later in this chapter and in Ch. 8.

D. Solar Activity During Observations

Observations from the same orbital periods in different years are compared here, so it is important to note if they were made during periods of dramatically different solar activity. Average sunspot numbers are plotted in Fig. 6.2 for the period of interest, and the dates and L_S values of the observations are noted. The only pair of observations taken during different levels of solar activity are those at L_S=102°, 103°. There was only one IR heterodyne spectrum suitable for the altitude analysis and the uncertainty is such that it is not possible to determine if solar activity played a role. Also, ultraviolet observations of ozone made around the same time as the dayglow measurement are very consistent with the IR heterodyne ozone retrieval (Ch. 7).

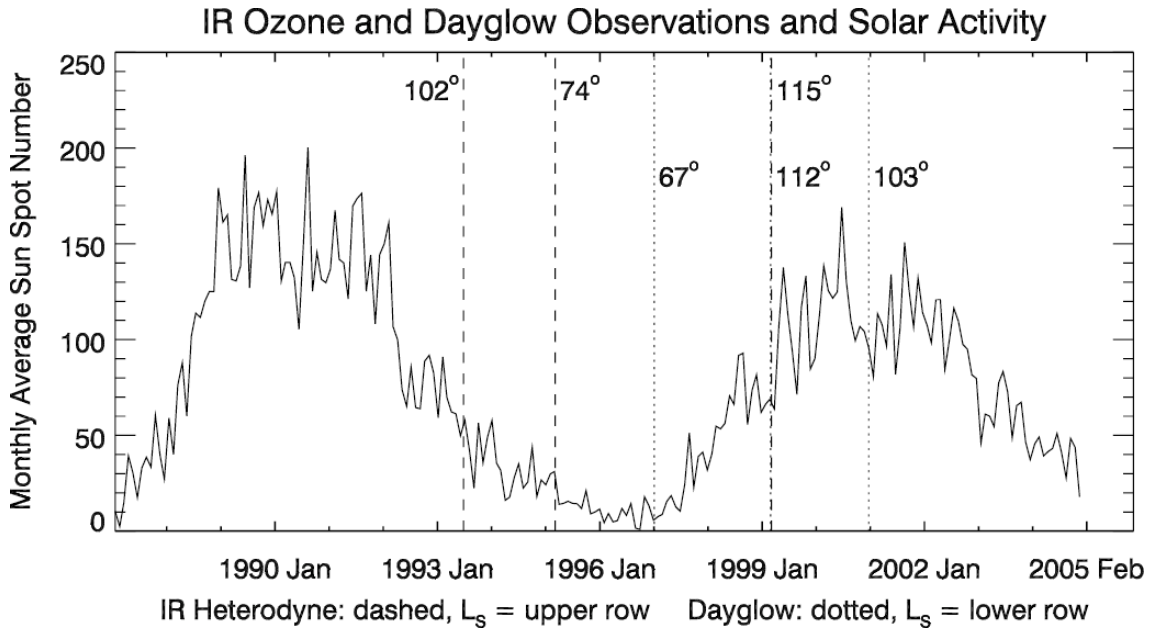


Figure 6.2. Dates for IR Heterodyne ozone observations (dashed, L_S=upper row) and corresponding $O_2(^1\Delta)$ observations (dotted, L_S=lower row) are noted on this plot of monthly average International Sunspot Numbers compiled by the Sunspot Index Data Center in Belgium.

III. Conclusions

Techniques for retrieving altitude information using total ozone column densities from infrared heterodyne spectroscopy and $O_2(^1\Delta)$ dayglow intensities were explored. One technique tested whether the observations indicated different scale heights for ozone and the background atmosphere ($H_{O3}/H \neq 1$). The other tested whether the observations indicated a high altitude excess of ozone, with $H_{O3}/H=1$ at lower altitudes. The results were as follows:

- Late Northern Spring: Results indicate $H_{O3}/H>1$ or a high altitude excess of ozone.
- Early Northern Summer: Results at $L_S=115°$ indicate $H_{O3}/H<1$ or no high altitude excess of ozone. The result at $L_S=102°$ is similar, but the uncertainty does not exclude the possibility of an excess.
- Early Northern Winter: Lack of dayglow emission and a low upper limit for total ozone column density are consistent with the lack of an excess of high altitude ozone.

Photochemical models predict the formation of a high altitude excess of ozone during aphelion seasons due to cooler temperatures resulting in a lower water vapor saturation altitude [e.g. Clancy and Nair 1996, Lefévre 2004]. During warmer perihelion seasons, water vapor can rise to higher altitudes, resulting in odd hydrogen formation and destruction of high altitude ozone. Photochemical models are further discussed in Ch. 8. The late northern spring results (around aphelion) and the qualitative result for early northern winter (around perihelion) are consistent with this predicted behavior. The early northern summer results are contrary to photochemical models, which still predict the presence of a high altitude excess of ozone even by this post-aphelion season. Additional measurements will be important for confirming this behavior and for constraining photochemical models.

Although heterodyne spectroscopy fully resolves Martian ozone features and allows the possibility of retrieving ozone altitude distribution from the line shape, it is evident that high signal-to-noise spectra are important for precise retrieval of altitude

information. The measurements in this work targeted the behavior of ozone abundance with latitude rather than altitude distribution. In combination with $O_2(^1\Delta)$ measurements, they yielded general information about ozone height distribution, but some uncertainties were high. Future measurements could target ozone altitude distribution by increasing the signal-to-noise ratio through longer integrations at fewer positions on Mars. This would help to further discriminate between possible ozone altitude distributions in an analysis incorporating $O_2(^1\Delta)$ dayglow measurements. It may also make it possible to retrieve altitude distribution information from the fully-resolved ozone line shapes themselves.

Chapter 7: Infrared Heterodyne and Ultraviolet Ozone Measurements

I. Ultraviolet Spectroscopy of Ozone on Mars

Ultraviolet techniques have been employed beyond the Earth's atmosphere to directly observe spectral absorption features of ozone on Mars. Ozone absorption was first measured on Mars by Mariner 7 in 1969 [Barth and Hord 1971]. Soon after, Mariner 9 measured ozone mainly at the poles from Mars orbit for close to half of a Martian year (Barth *et al*. 1973, Lane *et al*. 1973, Wehrbein *et al*.1979). High altitude ozone layers (~40 km) were observed by the short-lived Mars 5 [Krasnopolsky *et al*. 1980] and Phobos 2 [Blamont and Chassefiére 1993] spacecraft. The Hubble Space Telescope Faint Object Spectrograph (HST-FOS) has been used to observe and map ozone during a number of Martian orbital periods from Earth orbit [Clancy *et al*. 1996, 1999]. The Mars Express instrument SPICAM has recently begun mapping ozone abundance and altitude distribution from Mars orbit [Bertaux *et al*. 2000, 2004].

The target region for observing ozone on Mars in the ultraviolet (UV) is the 200-330 nm region, or Hartley bands, brought about by electronic excitation of ozone ($^1B_2 \leftarrow X^1A_1$). The band manifests itself as a broad absorption feature centered around 255 nm. Rayleigh scattering contributes continuum brightness in the spectral region, and the wavelength dependence of the scattering puts a slope under the band. There is a small surface reflectance contribution (more so over a polar ice cap). Water ice clouds and dust are additional sources of scattering that can add significant opacity (τ~0.25), decreasing the effective path length through the ozone.

The modeling of UV spectra yields ozone column densities, as well as height information in the case of occultations of the sun or stars by the limb atmosphere. Spectral modeling involves assumptions about the height distributions of the scattering components, which modify the effective path length of incoming and reflected solar UV radiation through the ozone. Lindner [1995], in reference to the Mariner 9 UV data, emphasized that the uncertainties in the scattering properties of clouds and dust may result in significant uncertainties (factor of 3) for retrieved ozone abundances. The ozone measurements in this work made at longer infrared wavelengths are far less sensitive to scattering. Infrared (IR) heterodyne spectra sample the entire ozone column because they detect thermal emission from the surface that is modified by CO_2 and ozone opacity as it travels upward. If there is indeed opacity significant enough to affect the longer infrared wavelengths (due to a dust storm, for instance), the continuum temperature and the CO_2 line shape can serve to indicate an inability to sample the entire column. The ozone IR line shape samples the altitude distribution of ozone and temperature. The UV band samples the column of ozone traversed by the UV radiation, which may not reflect contribution from the entire ozone column.

II. Infrared Heterodyne and Ultraviolet Ozone Retrievals Compared

The analysis in this work provides an excellent opportunity to test abundance retrieval of the same constituent (ozone) by two very different methods (IR heterodyne and UV). Contemporaneous measurements of ozone column density, as well as those made during similar orbital periods (L_S) in different years can be compared and the differences explored in terms of the nature of the measurements and the assumptions

made in retrieving abundances. Such a comparison is made between the ozone abundances from this work and from measurements made by HST-FOS [Clancy *et al.* 1996, 1999, R. T. Clancy, private communication].

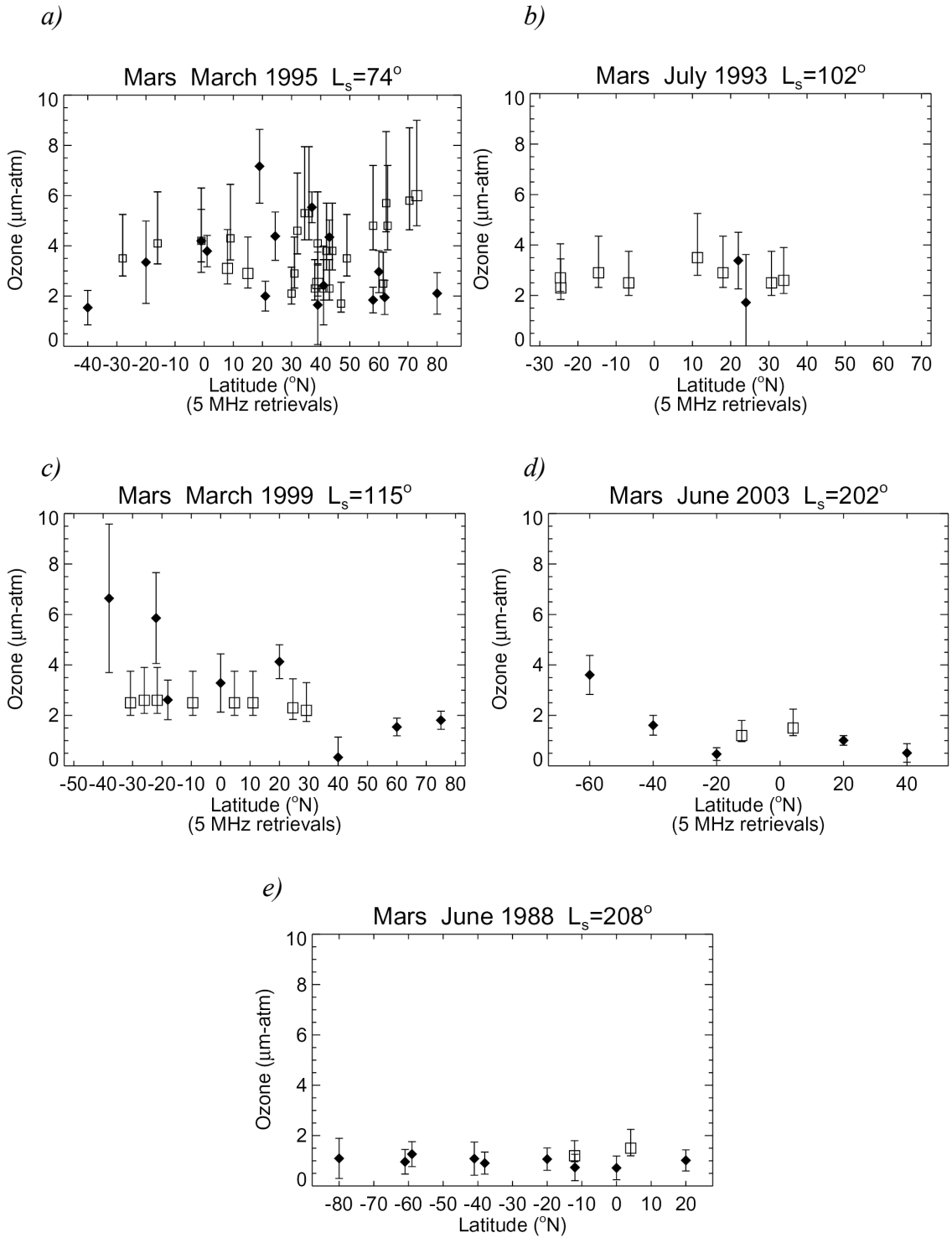
Ozone abundance retrieval from the IR heterodyne spectra in this work was detailed in Ch. 4. The modeling of HST-FOS UV spectra is detailed in Clancy *et al.* [1996]. They employ three atmospheric layers, distributing cloud opacity among the lower two layers and constraining water condensation level and Rayleigh scattering distribution according to the thermal profile. They assume a uniform ozone distribution between 0-40 km. The atmospheric scattering properties may or may not allow the entire ozone column to be probed by the measurements themselves, but the assumption of ozone and scattering distributions in the modeling process allows the retrieval of total ozone column abundance (down to the surface). Therefore, different assumed distributions of ozone and scattering can result in different total ozone column abundance retrievals due to different modeled path lengths. The uncertainty in the accuracy of the ozone retrievals is given in Clancy *et al.* [1999] as +50%, -20%, and those uncertainties are displayed in Fig. 7.1. However, as mentioned earlier, Lindner [1995] postulated even larger uncertainties (factor of 3) in the retrieval of ozone abundance from UV Mariner 9 measurements. The IR heterodyne retrievals tend to have accuracy uncertainties in the range of ±15-35% (Ch, 5), which are calculated for each individual measurement.

The IR and UV measurements are detailed in Table 7.1 and the column abundances are plotted in Fig. 7.1 when measurements were available at similar orbital positions (L_S).

Table 7.1. Hubble Space Telescope observations corresponding to those from this work.

Fig. 7.1 panel	Infrared Heterodyne		HST-FOS		
	L_S	Date	L_S	Date	Reference
a	74°	1995 Mar. 17-23	63°	1995 Feb. 25	Clancy *et al.* 1996
			61°	1997 Jan. 4	Clancy *et al*. 1999
b	102°	1993 July 4-7	104°	2001 Jan. 17	
c	115°	1999 Mar. 24-29	118°	2001 Feb. 16	R. T. Clancy, *priv. comm.* 2004
d	202°	2003 June 10-16	212°	2003 June 28	
e	208°	1988 June 3-7			

Figure 7.1. (following page) Ozone retrievals from infrared heterodyne spectroscopy (diamonds with 1σ uncertainties) compared to those from ultraviolet measurements made by the Hubble Space Telescope Faint Object Spectrograph [Clancy *et al.* 1996, 1999, R. T. Clancy, private communication]. The dates and orbital positions (L_S) of the UV measurements (open squares) are detailed in Table 7.1. (In panel *a,* large squares are from the same year as this work, and small squares are from a different year, and the UV measurements were earlier than IR measurements by ~10° in L_S.) The error bars on the UV measurements represent the uncertainty in the accuracy as quoted in Clancy *et al.* [1999], which was +50%, -20%. The error bars on the infrared heterodyne measurements reflect the uncertainty in the accuracy and were calculated for each individual measurement.


a)
Mars March 1995 L_s=74°
Ozone (µm-atm)
Latitude (°N)
(5 MHz retrievals)
b)
Mars July 1993 L_s=102°
Ozone (µm-atm)
Latitude (°N)
(5 MHz retrievals)
c)
Mars March 1999 L_s=115°
Ozone (µm-atm)
Latitude (°N)
(5 MHz retrievals)
d)
Mars June 2003 L_s=202°
Ozone (µm-atm)
Latitude (°N)
(5 MHz retrievals)
e)
Mars June 1988 L_s=208°
Ozone (µm-atm)
Latitude (°N)

Orbital periods from aphelion to approaching perihelion are sampled by the two methods. Overall, the UV ozone (open squares) and IR heterodyne retrievals in Fig. 7.1 show consistent behavior:

- There is generally good agreement in the variation of ozone at low to mid-latitudes, from high around aphelion (Fig. 7.1*a*) to low approaching perihelion (Figs. 7.1*d, e*).
- Both data sets show much more short-scale variability in late northern spring (Fig. 7.1*a*) than at the other periods.
- There is disagreement in the variation with latitude at 60°-80°N in late northern spring (Fig. 7.1*a*) and in the opposite sense at 20°-40°S at early northern summer (Fig. 7.1*c*).

This disagreement at 60°-80°N in late northern spring will be addressed first. In Fig 7.1*a*, the large squares represent UV measurements from the same year as this work, and the small squares are from a different year. Both data sets show the same departure from the IR measurements. The simplest explanation is that both sets of UV measurements are ~10° earlier in L_S than those from this work (Table 7.1). Heterodyne measurements made at mid-spring (L_S=40°, Fig. 5.4) show increased ozone abundance by a factor of ~2 at 60°N over those measured here in late spring (L_S=74°). This behavior is also seen in photochemical models to be presented in Ch. 8 (Fig. 8.1). It is possible that the UV measurements at L_S=61° and 63° are simply sampling high latitude ozone on its way down in abundance between mid- and late spring.

These high latitudes coincide roughly with the seasonal north polar ice cap, and so the effect of the cap on the UV observations and on the chemistry they may probe must be considered as an alternative explanation. The winter maximum extent of the north polar ice cap is ~60°N, but by this late spring season the sublimation of CO_2 and water ice would have caused it to retreat to ~70°N [James *et al*. 1997]. Still, the observing geometry places those northern latitudes close to the limb and a wider range of latitudes would contribute to a UV observation. The albedo of the cap is taken into account in the UV ozone retrievals. Clancy *et al.* [1996] note that more of the backscattered UV is from reflection because of the bright cap. Therefore the UV has traveled through the ozone column in both directions, causing the uncertainty in the vertical distribution of ozone to contribute less to the uncertainty in the derived total column abundance. They also note that cloud opacity cannot be measured over the bright cap. Their retrievals assume a certain cloud opacity, but in the absence of opacity, their derived column abundance would decrease by ~35%, which would bring the UV and IR measurements into slightly closer agreement at the high northern latitudes.

The presence of the polar cap may have an effect on the ozone chemistry. Ozone adsorbed onto the polar cap or suspended ice particle surfaces would be detected by UV observations but not by the IR heterodyne measurements that are sensitive only to the gaseous ozone that absorbs thermal emission from the surface of Mars. In the case of Earth, laboratory measurements determined that the loss of ozone onto stratospheric ice particles was insignificant [Dlugokencky and Ravishankara 1992], however similar studies do not exist for CO_2 ice because it is not important for Earth's stratospheric chemistry. Ozone has been detected within the icy surface of Ganymede [Noll *et al.*

1996], but its presence is most likely due to reactions within the ice induced by the charged particle flux in Jupiter's strong magnetosphere, which would not be applicable to Mars. Also, the seasonality of the polar cap would prevent any long-term buildup of ozone originating within ice. Hydrogen peroxide (H_2O_2) has also been detected in the atmosphere of Mars [Clancy *et al*. 2004, Encrenaz *et al*. 2004] and would be expected to freeze out onto the cap at times, along with water. Laboratory data on the interaction of ozone with ices under the conditions expected on Mars are important for understanding both ozone retrievals and atmospheric chemistry at polar latitudes.

It must be considered whether the problem may lie with the IR retrievals. If the surface temperature is not warmer than the atmosphere, insufficient contrast may cause the retrievals to underestimate the amount of ozone. However, thermal profiles at this orbital period from Mars Global Surveyor (MGS) [M. D. Smith *et al.* 2001, private communication] and the temperature-sensitive shapes of the CO_2 absorption measured by the heterodyne measurements do not show that behavior at 60-80°N.

The disagreement at 20°-40°S at early northern summer (southern winter, Fig. 7.1*c*) will now be addressed. The uncertainties in the 25 MHz resolution retrievals at 40°S (Fig 5.6) are larger than those from the 5 MHz resolution spectra and leave open the possibility for agreement between the IR and UV measurements. The 40°S IR measurements were on the southern limb of the observable disk of Mars as seen from Earth and may contain contribution from even higher latitudes due to the wider coverage of the beam at that position, as well as any potential tracking errors. Then, the measurements may probe cooler latitudes that contain more ozone. However,

temperature information retrieved from the CO_2 line shapes are consistent with those from MGS for 20°-40°S [M. D. Smith *et al.* 2001, private communication].

Unlike the late spring case just discussed, these measurements are outside the polar region, so issues of chemistry or assumed cloud opacity over the polar cap that may affect UV retrievals do not apply. The UV retrievals are sensitive to dust opacity, and ozone abundances will be underestimated if the assumed opacity is too low. UV spectra only sample part of the ozone column (depending on the atmospheric scattering properties), but in these retrievals an ozone distribution was assumed in order to retrieve total column abundances. It was shown in Ch. 6 for this period that the IR retrievals combined with $O_2(^1\Delta)$ dayglow measurements indicate low ozone at high altitudes and possibly an ozone scale height less than that of the rest of the atmosphere (Table 6.2). The column densities from the UV measurements were calculated assuming an ozone profile continuous up to 40 km. If the ozone distribution is confined to lower altitudes in the modeling of the UV absorption, the total ozone column density retrievals would increase and perhaps resolve the some of the difference between the two methods.

A final consideration when comparing ozone retrievals from the same orbital position in different years is the change in solar flux due to the 11-year solar activity cycle. Sunspot numbers are displayed in Fig. 7.2, and the dates and L_S values for the different observations are indicated. When comparing observations made at similar values of L_S, the only pair made during significantly different periods of solar activity were those at L_S=102° and 104° during early northern summer. Figure 7.1*b* did not show any disagreement between the limited IR retrievals and those from UV observations.

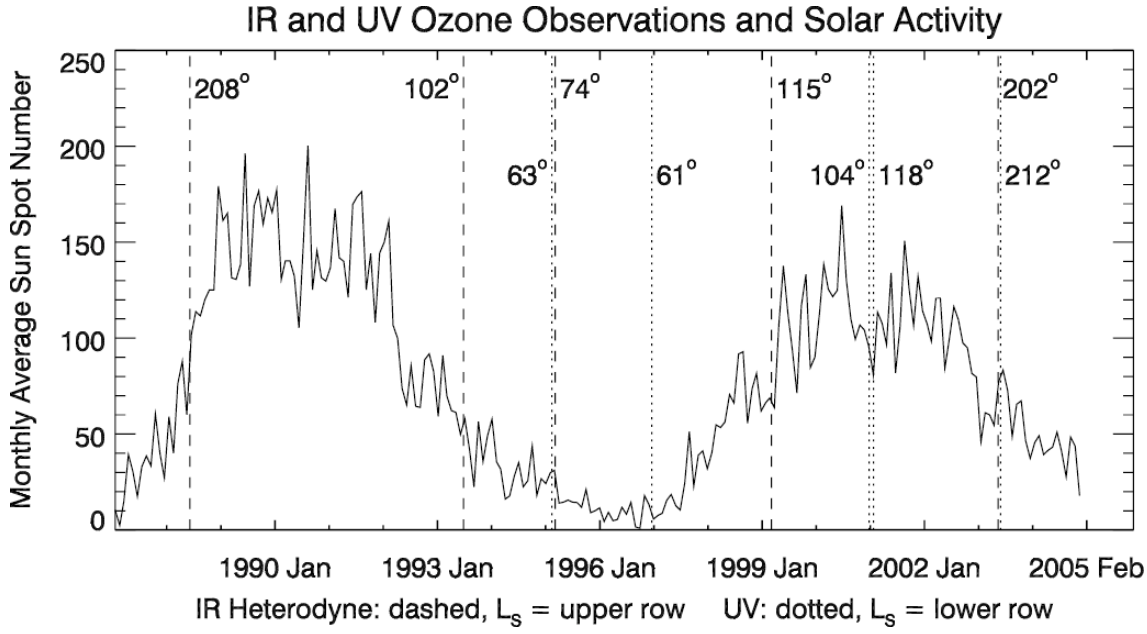


Figure 7.2. Dates for IR Heterodyne ozone observations (dashed, L_S=upper row) and UV ozone observations (dotted, L_S=lower row) are noted on this plot of monthly average International Sunspot Numbers compiled by the Sunspot Index Data Center in Belgium.

III. Discussion

The use of two very different techniques to measure the same constituent is important for testing the accuracy of both methods. Other than the one published IR heterodyne ozone analysis [Espenak *et al*. 1991], only ultraviolet measurements of the total column abundance of ozone on Mars have been available. This work provides an opportunity to compare ozone abundance retrievals from both methods for variety of conditions on Mars.

Contemporaneous and orbital comparison of ozone retrievals from this work and from Hubble Space Telescope UV observations show very good agreement, from aphelion to near perihelion. The drop in ozone seen in the IR heterodyne retrievals over

that period is reflected in the behavior of the UV retrievals. Ozone abundances from the two techniques at low latitudes agree quite well overall. The discrepancy noted at high northern latitudes during late spring (L_S=74°) could possibly be attributed to one of the following:

- UV measurements were made ~10° earlier in L_S in the spring, possibly sampling higher polar ozone abundance on its way down after northern winter.
- UV retrievals of ozone assume a level of cloud opacity, and retrievals would be larger in the absence of cloud opacity, bringing them into closer agreement with the IR measurements.
- The IR technique only measures gaseous ozone, but UV measurements would see contribution of ozone on the surface of the polar cap, if the chemistry of ozone with polar ices allows its presence.

The discrepancy noted at the southernmost observable latitudes (20°-40°S) around early northern summer (southern winter, L_S=115°) could possibly be attributed to one of the following:

- IR measurements were made close to the southern edge of the visible disk of Mars, and pointing uncertainty may cause spectra to include contribution from higher southern latitudes.
- If the modeled dust opacity is too high, then UV retrievals will underestimate ozone column abundance.
- The total column abundance retrieved from UV measurements is sensitive to the assumed ozone distribution. Confining ozone to lower altitudes (as

indicated in Ch. 6) would increase the retrieved column abundance and bring UV and IR retrievals into closer agreement.

The comparison presented here is much more extensive than previously possible. The general consistency between both techniques lends weight to the accuracy of both for retrieving ozone column density. However, the inability to conclusively address the discrepancies points to both the need for more observations and the need for better laboratory data. Coordinated observations, especially at northernmost and southernmost accessible latitudes, would identify the repeatability of the measurement discrepancies and narrow down the possible sources. Results will soon be available from the Mars Express instrument SPICAM [Bertaux *et al.* 2001, 2004], which is conducting the first long-term study of ozone from orbit since Mariner 9. IR heterodyne spectroscopy can provide an important test of those results and, as with the HST-FOS observations, discrepancies may highlight observational and retrieval issues for either technique, or issues of photochemistry on Mars.

Laboratory measurements of the chemistry of ozone with water, CO_2, and H_2O_2 ices under the conditions of the Martian polar regions could possibly resolve the difference at 60°N during late northern spring and provide information important to photochemical modeling. If the retrieval discrepancies have their source in chemistry, then the IR heterodyne and UV ozone measurement techniques would be not only complementary but synergistic and essential for understanding atmospheric photochemistry on Mars.

Chapter 8: Using Observations of Ozone on Mars to Test Photochemical Models

I. Ozone and Photochemistry

Ozone is the most chemically active constituent that is currently observed on Mars, and photochemistry predicts it to be an excellent tracer of odd hydrogen species (Ch. 1). During the daytime, ozone is considered to be in photochemical equilibrium because its photochemical lifetime of less than a day is much shorter than the time scale for transport. Transport time scale is defined as H^2/K where H is the atmospheric scale height (see Ch. 6) and K is the coefficient of eddy diffusion ($cm^2\ s^{-1}$). Using a typical scale height for Mars of 11 km and $K \sim 10^6\ cm^2\ s^{-1}$ [e.g. Nair *et al*. 1994, Krasnopolsky 1995], the transport time scale is on the order of weeks in the lower atmosphere, much longer than the photochemical lifetime of ozone. At night, photolysis stops and atomic oxygen, abundant at higher altitudes, is converted to ozone. If odd hydrogen is not abundant at those altitudes (e.g. during aphelion periods when the water saturation altitude is low [Clancy and Nair 1996]) an increase in total ozone column density of as much as 4× is throught to occur [Lefèvre *et al*. 2004].

Observations of ozone abundance on Mars are considered to be important for constraining photochemical models that seek to explain odd hydrogen chemistry and CO_2 stability. This will be explored and applied as follows:

- Briefly review the development of photochemical models of the Martian atmosphere.
- Examine the role of ozone in testing photochemical models.

- Apply the database of ozone column abundance and behavior from this work to the testing of the first three-dimensional photochemical model of Mars [Lefèvre *et al*. 2004].

II. Photochemical Models

Many photochemical models of the Martian atmosphere have been published. They are all based on the basic CO_2 reformation process catalyzed by odd hydrogen described in Ch. 1, but they differ in how they seek to come into agreement with available atmospheric data. Chemical reactions, reaction rates, eddy diffusion coefficients, photodissociation cross sections, temperature dependencies, hydrogen and oxygen escape rates, ionospheric processes, nitrogen chemistry, and heterogeneous (surface) chemistry are some of the issues that must be considered in modeling. Most photochemical models have been one-dimensional, meaning they examine the height variation of species and simulate transport through a vertical eddy diffusion coefficient.

The first results of one-dimensional calculations applying odd hydrogen-catalyzed recombination of CO_2 were in the groundbreaking papers of McElroy and Donahue [1972] and Parkinson and Hunten [1972]. Early models such as these and others (e.g. Kong and McElroy [1977a, 1977b]) employed fast eddy mixing or large amounts of water in order to reform CO_2 fast enough. It was later recognized that the room temperature value of the CO_2 absorption cross section needed to be reduced under Martian conditions to account for its temperature dependence. This has the effect of increasing the amount of radiation available to photolyze water vapor, creating the opposite problem of an overproduction of odd hydrogen resulting in too much CO_2

reformation and too little CO and ozone compared to observations. Other adjustments to models were needed to compensate.

Development continued on one-dimensional models that examined Martian photochemistry under mean global, seasonal, and diurnal conditions [e.g. Shimazaki 1989, Krasnopolsky 1993, 1995, Nair *et al.* 1994, Atreya and Gu 1994]. Some one-dimensional models were applied locally in order to calculate photochemical behavior with latitude or season [e.g. Shimazaki and Shimizu 1979, Shimazaki 1981, Clancy and Nair 1996]. A two-dimensional (i.e. zonally averaged) photochemical model of Earth was adapted to Mars by Moreau *et al.* [1991] to interactively treat photochemical and dynamic effects.

The one-dimensional photochemical models of the last decade differed in areas such as eddy diffusion, rate constants, water vapor distribution, and the chemistry of minor species. Some required a heterogeneous sink for odd hydrogen [e.g. Krasnopolsky 1993, Atreya and Gu 1994] while others found that gas phase chemistry could be sufficient [e.g. Nair *et al*. 1994, Krasnopolsky 1995]. All relied on the pool of available spacecraft and ground-based observations of Mars up to that point with which to construct and test their models. However, Krasnopolsky [2003*b*] points out that recent ground-based and spacecraft results have brought the models out of agreement with observations and point again to the need for heterogeneous chemistry to bring down odd hydrogen production.

III. Ozone as a Test of Photochemical Models

Krasnopolsky [2003b] notes that global mean photochemical models are important for investigating the chemistry of CO, O_2, and H_2, whose photochemical life times are much longer than atmospheric transport time scales. For example, Krasnopolsky [1993] determines mean lifetimes for CO, O_2 and H_2 of 6, 40 and 2000 years based on ratios of modeled column density to column loss rate. The one-dimensional models of the 1990's used ozone abundance retrieved from the infrared heterodyne analysis of Espenak *et al.* [1991] to test their models. However, because of the short photochemical lifetime of ozone and the spatial, seasonal, and orbital variability seen in this work, ozone is not a very meaningful test of global mean photochemical models beyond indicating if modeled ozone abundance is within an acceptable range.

The larger pool of ozone abundance information now available through this work, as well as through $O_2(^1\Delta)$ and ultraviolet observations (Chs. 6, 7), is very important for testing photochemical models that address specific spatial, seasonal and orbital conditions. Such models are necessary to explain the variability of ozone and the odd hydrogen chemistry it probes.

For example, the seasonal behavior of ozone at 65°N and 65°S was modeled by local one-dimensional models of Shimazaki and Shimizu [1979] and Shimazaki [1981]. The models were developed to reproduce polar winter ozone abundances observed by Mariner 9 [Barth *et al.* 1973]. As the poles come out of winter, the modeled ozone abundances drop due to destruction by odd hydrogen resulting from increased water vapor photolysis. Note that the models at 65°N predict less than half the ozone seen by this work in mid- and late spring (L_S=40° and 74°, Tables 5.2 and 5.3) at 60°-65°N.

Since then, chemical parameters have been updated, and much of the work on Martian photochemistry has focused on mean conditions. Recently, a three-dimensional photochemical model has been developed [Lefèvre *et al*. 2004] that examines local photochemistry on a global and seasonal basis. The ozone abundances retrieved in this work are an excellent tool for testing specific predictions of this model.

IV. The First Three-Dimensional Model

A. Total Ozone Column Abundance and Seasonal/Orbital Variability

The first three-dimensional photochemical model of the atmosphere of Mars was developed by Lefèvre *et al*. [2004], which combines photochemistry with the general circulation model (GCM) of Forget *et al.* [1999]. Chemistry resulting from local conditions (including topography) is combined with three-dimensional atmospheric circulation and an annual water cycle in order to develop a comprehensive global, diurnal, and seasonal photochemical model. The model calculates water vapor profiles, but the GCM abundances are consistent with those measured by Mars Global Surveyor [Smith *et al*. 2002]. The model uses a constant dust optical depth consistent with seasons of minimal dust, simplified nitrogen chemistry, and it does not include cloud transport or heterogeneous processes.

Slices of the model corresponding to the orbital periods (L_S), longitudes, and local times of the heterodyne observations [F. Lefévre and S. Lebonnois, private communication] are show in Fig. 8.1, along with the 5 MHz resolution IR heterodyne ozone column density retrievals and 1σ uncertainties. Each model curve is for a different

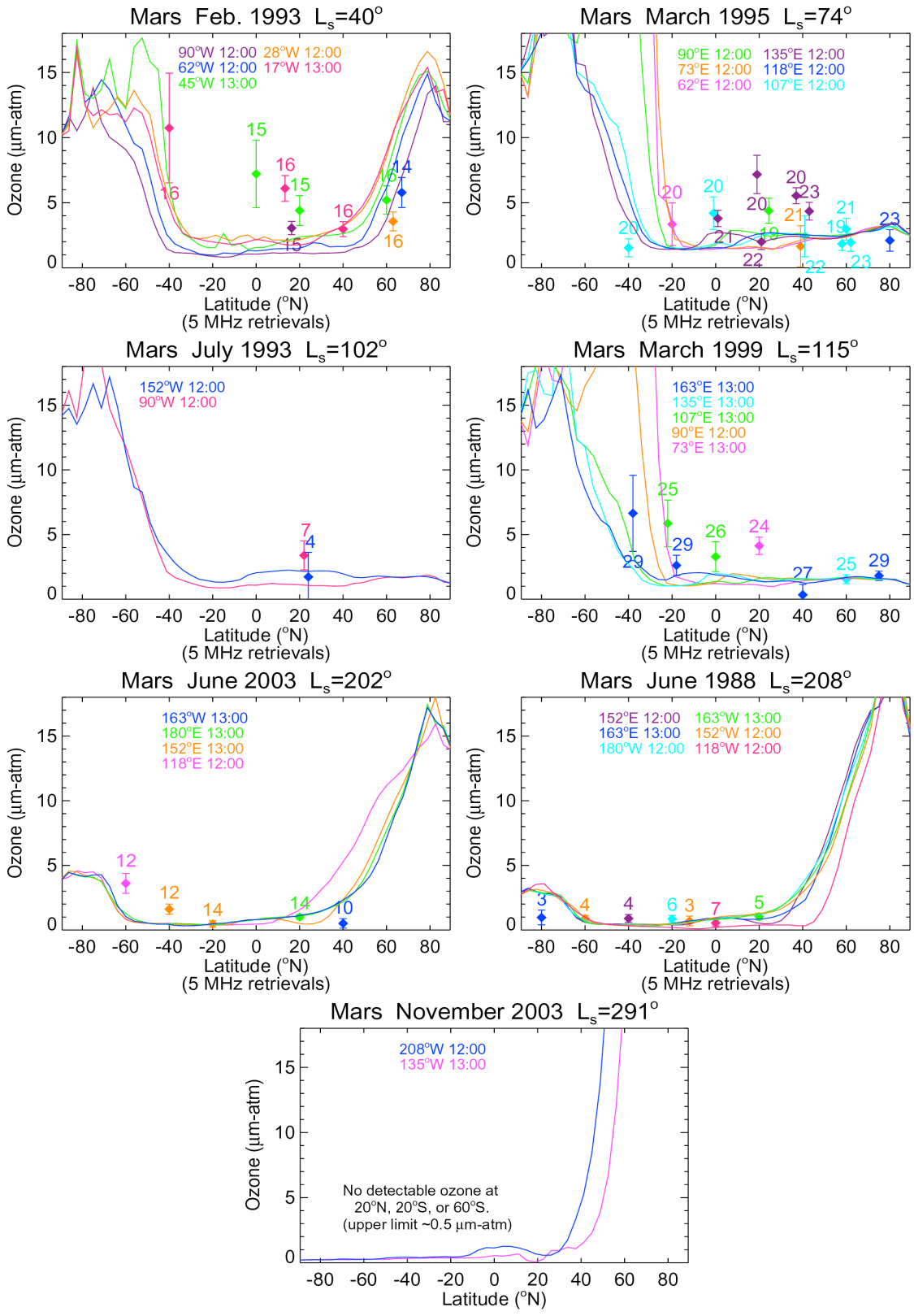
longitude and local time (indicated by colored text), and color indicates the correspondence between observed and modeled column density. The following behavior is noted:

- During the near-perihelion periods of L_S=202°, 208°, and 291°, modeled ozone abundances agree quite well with observations and upper limits.
- During the near-aphelion periods of L_S=40°, 74°, and 115°, although there is general agreement at higher latitudes, the model consistently underestimates low latitude ozone abundance as compared to observations.

The overall qualitative agreement in the behavior of ozone between aphelion and perihelion is good. The quantitative agreement around perihelion is very good, with the some departure seen at higher latitudes. That could possibly be attributed to a larger sampling of latitudes by the instrument beam toward a polar limb or to dynamical effects near the poles that result in ozone abundance variations (as seen by Mariner 9 [Barth *et al.* 1973]). During the aphelion periods of L_S=40°, 74°, and 115°, the agreement is good at higher latitudes, but the low latitude abundance is consistently underestimated by the model as compared to observations.

Similar behavior was noted by Lefèvre *et al*. [2004] when comparing their model to a limited set of observations (one $O_2(^1\Delta)$ dayglow and two ultraviolet data sets, and the published heterodyne analysis of Espenak *et al*. [1991]). The ozone retrievals in this work provide a more extensive sampling of orbital periods with which to test the model. This work has also revised the Espenak *et al*. [1991] retrievals at L_S=208° downward by ~30%, bringing them into better agreement with the perihelion model.

Figure 8.1. (following page) Ozone column abundances and 1σ uncertainties from this work are displayed with corresponding slices from the three-dimensional photochemical model of Lefèvre *et al*. [2004]. The longitudes and local times of the model curves are indicated on the plots by color-coded text, and are close to those of the observations. Color also indicates the correspondence between observed and modeled ozone column densities. Numbers displayed with data points indicate day of month of observation. The general behavior of ozone column abundance with L_S seen in the data is reproduced by the model, but there is significant quantitative departure of the model from the observed values at lower latitudes during aphelion periods. Better agreement overall is seen during perihelion periods. (Aphelion is at L_S=71° and perihelion is at L_S=251°.) The large ozone abundances modeled in the polar regions occur during their respective winters when those latitudes are not visible from Earth.


Mars Feb. 1993 Ls=40°
90°W 12:00 28°W 12:00
62°W 12:00 17°W 13:00
45°W 13:00
Mars March 1995 Ls=74°
90°E 12:00 135°E 12:00
73°E 12:00 118°E 12:00
62°E 12:00 107°E 12:00
Mars July 1993 Ls=102°
152°W 12:00
90°W 12:00
Mars March 1999 Ls=115°
163°E 13:00
135°E 13:00
107°E 13:00
90°E 12:00
73°E 13:00
Mars June 2003 Ls=202°
163°W 13:00
180°E 13:00
152°E 13:00
118°E 12:00
Mars June 1988 Ls=208°
152°E 12:00 163°W 13:00
163°E 13:00 152°W 12:00
180°W 12:00 118°W 12:00
Mars November 2003 Ls=291°
208°W 12:00
135°W 13:00
No detectable ozone at
20°N, 20°S, or 60°S.
(upper limit ~0.5 µm-atm)
Ozone (µm-atm)
Latitude (°N)
(5 MHz retrievals)

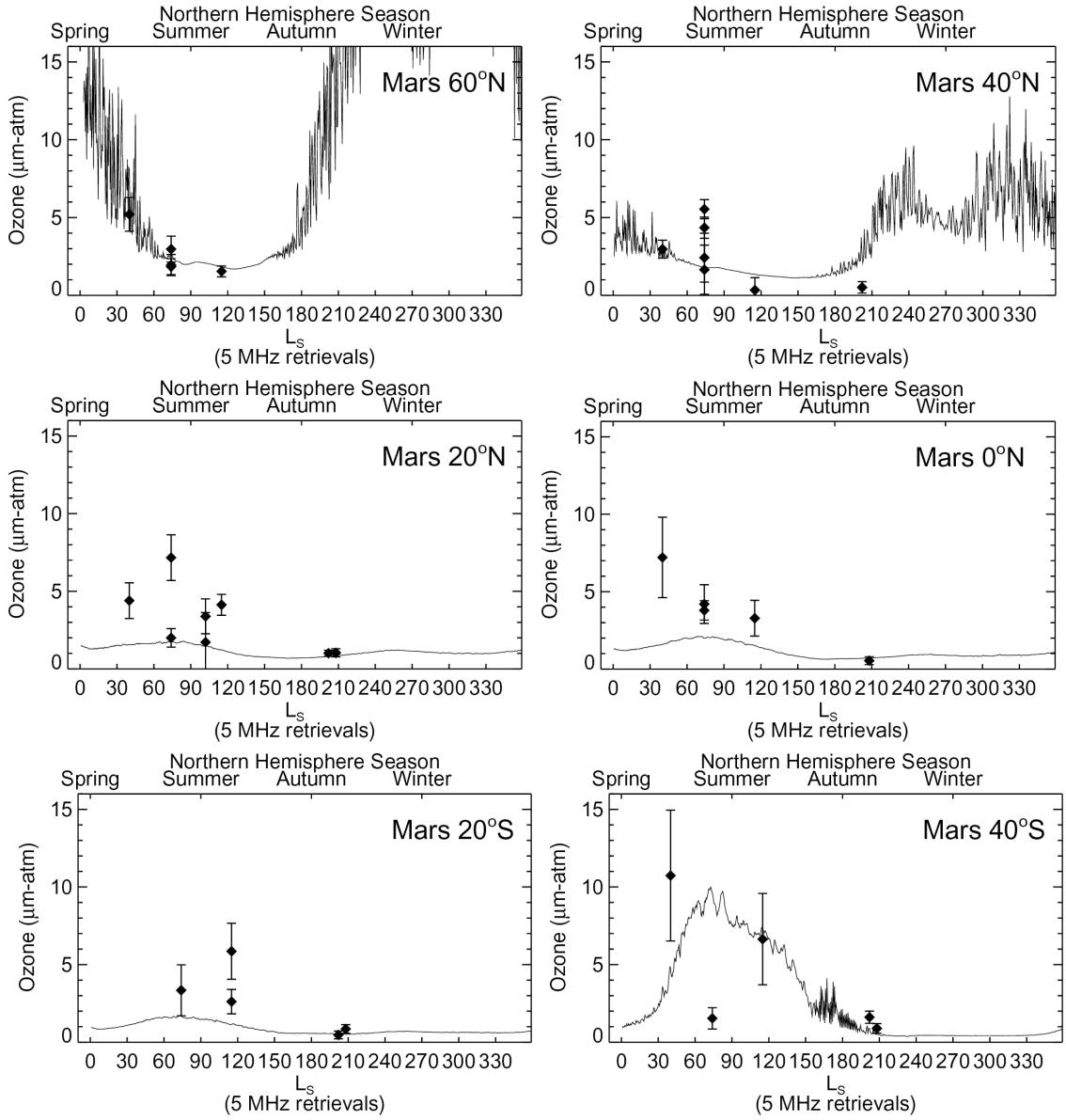


Figure 8.2. Ozone column abundances and 1σ uncertainties from this work are displayed as a function of L_S with model abundances from the three-dimensional photochemical model of Lefèvre *et al*. [2004] (0° longitude, 12:00 local time). Aphelion is at L_S=71° and perihelion is at L_S=251°. Excellent agreement is seen for the most part in the seasonal behavior at 60°N, and during perihelion seasons at lower latitudes, but the model consistently underestimates ozone at low latitudes during aphelion seasons.

Another view of the behavior of the observations and the model is given in Fig. 8.2, where retrieved ozone abundances at each target latitude are compared to model abundances as a function of season (L_S). The following behavior is noted:

- At 60°N, the agreement between the model and observations is excellent over the aphelion periods sampled (except for one data point with a large uncertainty).
- At 40°N, generally good agreement between the model and observations is seen around aphelion in spite of the scatter at L_S=74°.
- At 20°N, 0°N, and 20°S, there is excellent agreement between the model and observations approaching perihelion, but the model underestimates the amount of ozone during the aphelion periods.
- At 40°S, there is large scatter and uncertainty in the observations around aphelion but there is the is excellent agreement between the model and the data approaching perihelion,

At 40°N, the discrepancy between the model and the single data point at L_S=208° could possibly be due to that observation being toward the extreme northern observable latitudes, which could magnify the effect of any pointing and tracking uncertainties. Similarly, the aphelion aspect geometry of Mars may contribute to the uncertainties and scatter in the ozone retrievals at 40°S around that time, but observations approaching perihelion agree well with the model. There is otherwise very good agreement except at low latitudes during aphelion periods, and this is considered to be the most significant and repeatable departure of the model from the observations. Although the qualitative seasonal behavior of ozone is reproduced at low latitudes by the model, the quantitative

results around aphelion require an examination of the chemistry and assumptions incorporated in the model.

Lefèvre *et al*. [2004] noted the low latitude problem in their comparison of limited ultraviolet and infrared observations to their model and explored possible reasons for the underestimation of ozone at low latitudes. An overabundance of water vapor would lead to increased odd hydrogen production and ozone destruction, but they note that the water abundances in the GCM compare well with those from Mars Global Surveyor. They point to uncertainties in photochemical and kinetics parameters, and the fact that a constant, low dust abundance is assumed. As mentioned earlier, the temperature dependence of CO_2 can have a great effect on water photolysis, and the model uses a constant cross section below 200K. However, they note that if they extrapolate the temperature dependence, the ozone abundances are further decreased. They see better water cross section data at low temperatures as important, and they also point to updated reaction rates from terrestrial research, but it still does not solve the aphelion problem.

They do see heterogeneous chemistry as promising for resolving the discrepancy. Loss of odd hydrogen onto dust particles would allow ozone abundance to increase, but dust is abundant during the warmer perihelion period, and this is when the model was more consistent with observations. They propose that heterogeneous chemistry involving water ice cloud particles may be a solution because that sort of chemistry would dominate during the cooler aphelion period when low latitude clouds are more abundant [Smith 2004]. Increased ozone production in the presence of water ice clouds was suggested by Krasnopolsky and Parshev [1979] as a way of explaining the abundance of ozone in a morning layer observed by Mars 5.

B. Ozone Altitude Distribution

Clancy & Nair [1996] used the Nair *et al.* [1994] model to investigate photochemistry at 30° latitude over the course of the Martian year by utilizing observed variations in temperature and water saturation altitude, or hygropause, in their model. They modeled ozone seasonal behavior at 20 and 40 km (along with the behavior of CO, O_2, and odd hydrogen). They showed that variation in ozone number density at 20 and 40 km between perihelion and aphelion is much greater than that of the total ozone column because of the behavior of the ozone distribution in response to the water distribution and the hygropause altitude. This behavior shows why a strict anticorrelation of total ozone column density with total water vapor abundance is not observed (Ch. 5) and highlights the importance of understanding both abundance and height distribution of atmospheric constituents. As the hygropause altitude decreases around the cooler aphelion periods, ozone abundance can increase at high altitudes. During the perihelion periods, the hygropause level rises in response to warmer temperatures, resulting in odd hydrogen production that destroys high altitude ozone.

The three-dimensional model of Lefèvre *et al*. [2004] predicts altitude distribution of ozone based on the chemistry resulting from the changing water vapor distribution as calculated by the GCM over the course of the year on Mars. As with the model of Clancy and Nair [1996], a high altitude layer of ozone forms during the cooler seasons around aphelion when the hygropause is at lower altitude (~10-15 km). During the perihelion seasons, that layer disappears due to the warmer conditions and higher hygropause (~30-40 km). The altitude analysis performed in Ch. 6 can be compared to

the behavior of ozone distribution in response to water vapor distribution as seen in the model [Fig. 2 of Lefèvre *et al*. 2004].

At L_S=291°, no ozone or $O_2(^1\Delta)$ was measured, and that is not inconsistent with the altitude distribution predicted at that perihelion period. The high altitude layer has disappeared in the model and the low altitude component is also somewhat lower than many other orbital periods. The only high abundance of ozone is at the winter pole, which is not visible, so the observations do not contradict the model.

At L_S=74° and 102°, the results do not exclude a high altitude layer, which is expected by the model during those aphelion periods. The L_S=115° results are more difficult to understand in terms of the model. Unlike the other periods, the data sets in this analysis were taken within days of each other, lending weight to the results. However, they do not indicate a high altitude layer as predicted by the model, which actually underestimates total ozone column abundance at low latitudes (Fig. 8.1). It is possible the conditions were atypical, but observations of water vapor, clouds, and dust made by Mars Global Surveyor during that year and others do no support that view [Smith 2004]. Problems could lie with the ozone measurements which were not targeted toward this sort of study, low $O_2(^1\Delta)$ intensities which differed between data sets, or with the ozone distributions assumed in the analysis (Ch. 6). The consistent underestimation of low latitude ozone by the model during the aphelion seasons also points to possible issues with the modeled altitude distribution, but if the heterogeneous processes proposed earlier were incorporated into the model, then the high altitude abundance would actually increase.

Coordinated observations targeting ozone altitude distribution will help to provide better information with which to compare models. Planned observing schemes by SPICAM on Mars Express [Bertaux *et al*. 2000, 2004] should also provide altitude information for ozone that can be used to test distributions predicted by models.

V. Correcting Photochemical Models

The ozone abundances from this work were used to test the three-dimensional photochemical model of Lefèvre *et al*. [2004], and the greatest discrepancy is an underestimation of low latitude ozone around aphelion periods. An overproduction of odd hydrogen in the model would lead to lower ozone abundances relative to measurements. Observations of the distributions of ozone and water vapor in the atmosphere are important. Although the water vapor column abundances calculated by the GCM are consistent with observations, the altitude distribution itself has been shown to affect the ozone distribution and lead to a less strict anticorrelation of water and ozone total column abundance. Total column abundance provides a good test of a model, and measurement of altitude distribution provides an even stricter test of model predictions.

Heterogeneous chemistry could hold the key. The fact that low latitude observations agree with the model at perihelion but not at aphelion is a very important clue. A heterogeneous sink of odd hydrogen onto dust particles would not solve the problem at aphelion because dust is less abundant than at perihelion, when the sink would only lead to an overestimate of ozone abundance. Observations by Mars Global Surveyor show water ice particles at low latitudes only during aphelion seasons [Smith 2004]. A sink of odd hydrogen onto ice particles could probably be implemented in the model in

such a way as to resolve the discrepancy between the model and observations. However, the accuracy of such a model would be questionable without laboratory studies to back up the choice of efficiency for the odd hydrogen sink. Laboratory studies of heterogeneous process involving both dust and ices (CO_2 and H_2O_2 as well as water) under Martian conditions are required. Heterogeneous chemistry in recent one-dimensional global mean models was identified as both important [Krasnopolsky 1993, Atreya and Gu 1994] and unnecessary [Nair *et al*. 1994, Krasnopolsky 1995]. In the seasonal three-dimensional model of Lefèvre *et al*. [2004], the need for heterogeneous chemistry in addition to gas phase chemistry can be limited to particular latitudes and seasons, and a possible surface for that chemistry can be identified (water ice clouds). Laboratory measurements are required in order to understand the overall role of heterogeneous chemistry on Mars and produce a model that is consistent with observed ozone behavior that has a basis in tested chemistry.

Updated laboratory information on reaction rates and temperature dependent photodissociation cross sections are important for modeling. Some information can be adapted from terrestrial work. For instance, rates for terrestrial reactions that involve a third body are adjusted to take into account the efficiency of reactions involving the more massive and abundant CO_2 molecule in the case of Mars. Reaction rates that have been updated according to terrestrial observations should continue to be considered. At the same time, the application of terrestrial results to the atmospheric modeling of Mars must proceed with caution, as issues such as temperature dependency may come into play in adapting results to the conditions on Mars. Photochemical modeling of the atmospheres

of Earth and Mars can be very complementary to each other because they provide different conditions under which model assumptions about chemistry can be tested.

Dust storms affect the warmer perihelion season and, although the data in this work are fairly consistent with the three-dimensional model around perihelion, another factor that should be considered is the recent work by Atreya *et al*. [2004] on oxidant production in dust devils and storms. They find that triboelectricity (electricity produced through friction) in dust devils and storms results in increased production of OH and O^- and ultimately H_2O_2 at levels much higher than from photochemical production alone. The life issue is of course the thrust of that study, but the effect on ozone would be worth exploring to be able to support interpretation of perihelion observations and model predictions. Increased OH production during dust activity would lead to ozone destruction, and the model predicts a significant decrease in ozone abundance, but dust opacity has not yet been accounted for [A. S. Wong, private communication]. Observations of ozone during global dust storms would not be able to probe the abundance near the surface. Localized dust phenomena could lead to localized depletion of ozone relative to model predictions or previous observations. The effects of triboelectricity on chemistry and abundance deserve study beyond the H_2O_2 issue.

Chapter 9: Conclusions

I. Ozone, Photochemistry, and CO_2 Stability on Mars

The recognition of the important role that odd hydrogen chemistry could play in the atmospheric stability of Mars gave direction to the solution of CO_2 reformation. Odd hydrogen resulting from water vapor photolysis can participate in catalytic reactions to reform CO_2, and it also destroys ozone (Ch. 1). These issues are not entirely unique to Mars. The stability of CO_2 in the stratosphere of Venus is thought to be maintained through catalytic chemistry involving chlorine species, and ozone in the Earth's stratosphere is catalytically destroyed by odd hydrogen, as well as by nitrogen, chlorine, and bromine species [cf. Yung and DeMoore 1999].

Since ozone is destroyed by odd hydrogen, it follows that measurements of ozone abundance can trace the abundance of odd hydrogen species that have not yet been directly observed in the atmosphere of Mars. Infrared heterodyne spectroscopy can measure ozone absorption features on Mars when they are Doppler shifted away from their telluric counterparts, allowing the only direct measurement of Martian ozone from the surface of the Earth. This makes it possible to conduct ground-based studies of the atmospheric stability of Mars through a tracer of the odd hydrogen species thought to participate in the reformation of CO_2.

Photochemical models of the atmosphere of Mars have had to rely on limited observations of ozone to test their predictions of odd hydrogen chemistry. The analysis technique developed in this work and applied to infrared heterodyne data sets has

provided the most extensive sampling of spatial, seasonal, and orbital behavior of ozone on Mars available to date. The application of this valuable ozone database resulted in:

- Confirmation that odd hydrogen chemistry is responsible for the reformation of CO_2 and the stability of the atmosphere of Mars.
- Validation of the three-dimensional photochemical model of Lefévre *et al*. [2004] (Ch. 8).
- Demonstration of the general spatial and orbital consistency of infrared heterodyne and ultraviolet measurements of ozone column density (Ch.7).
- Exploration of techniques to retrieve the altitude distribution of ozone using total ozone column densities from this work and $O_2(^1\Delta)$ dayglow intensities, which probe ozone above ~20 km (Ch. 6).

In addition to these important results, this work has provided the following contributions:

- Demonstration of qualitative but not strict anticorrelation of ozone and water vapor column abundance (Ch. 5), pointing to the role of altitude distribution of constituents.
- Confirmation of the need to explore the role of heterogeneous chemistry in the atmosphere of Mars, along with laboratory measurements under Martian conditions (Ch. 7, 8).
- Validation of infrared heterodyne spectroscopy as a passive technique for retrieving altitude profiles of terrestrial ozone (Ch. 3).

- Development of a technique for analyzing telluric-contaminated infrared heterodyne spectra of Mars (Ch. 4).

The improvement in computer technology over the years has been matched by increasing complexity of modeling code. This trend will continue, as computational ability will never be able to keep pace with the desire to understand the universe around us. Post and Votta [2005] stress that successful coding projects must involve verification, validation, and quality management. They find that these practices routinely developed and employed in the information technology community are not well implemented in the science community. The contribution of this work falls under the area of validation. Observed ozone abundances were used to test and validate photochemical models (Ch. 8) with the assumption that they were already verified. Many one-dimensional models predicting average conditions were validated with a few measurements, including ozone, and it has been indicated in this work that it is not entirely meaningful to validate such models with ozone due to its short photochemical lifetime and high spatial, seasonal, and orbital variability. However measurements of ozone are very important for the validation of models that make specific spatial, orbital/seasonal, and diurnal predictions. In fact, such models require a very extensive pool of observations as well as laboratory data for validation.

The analysis of infrared heterodyne spectra of Mars in this work confirmed in general the ozone/water anticorrelation expected by odd hydrogen photochemistry. Higher ozone column abundance was observed during the cooler aphelion periods when less water is expected to be present in vapor form. The warmer perihelion periods saw a

drop in ozone column abundance. For particular orbital periods (L_S), some anticorrelation was seen in the behavior of ozone and water vapor column abundance with latitude (Ch. 5). However, the quantitative behavior of ozone abundance did not show the degree of variation that water vapor is observed to undergo. This supports predictions that the altitude distribution of the constituents is important to the photochemistry and resulting column abundances [e.g. Clancy *et al*. 1996, Lefèvre *et al*. 2004].

The ozone abundances in this work were used to test spatial, seasonal, and orbital variability of ozone predicted by the first three-dimensional photochemical model of the Martian atmosphere [Lefèvre *et al*. 2004] (Ch. 8). The overall consistencies give confirmation to the role of odd hydrogen chemistry in maintaining the stability of the CO_2 atmosphere of Mars and validate the model. The underestimate of low latitude ozone during aphelion periods points to additional processes, such as heterogeneous chemistry, that must be taken into account in order to better reproduce the atmospheric conditions. However, the general agreement is very encouraging for this first attempt at combining photochemistry and global circulation into a three-dimensional model, as well as for our understanding of the Martian CO_2 stability issue.

Techniques for extracting information on the altitude distribution of ozone from total ozone column densities and $O_2(^1\Delta)$ dayglow intensities were explored (Ch. 6). There were mixed results in terms of confirming high altitude layers predicted by photochemical models at the aphelion periods sampled, and uncertainties were high. Altitude distributions produced by photochemical models (e.g. Fig. 6.1) indicate that alternative distributions may need to be tested beyond the simple ones investigated. It is

also important to make coordinated observations that specifically target this sort of study, with longer integration times in order to increase the signal-to-noise ratio of spectral features.

The general agreement between ozone column densities retrieved from infrared heterodyne and ultraviolet spectra (Ch. 7) means that retrievals can be combined to broaden the pool of available data with which to validate photochemical models. The few discrepancies at some northernmost and southernmost visible latitudes may have their origins in observational or modeling technique, or in actual chemistry probed differently by IR and UV. Additional comparisons will be helpful, as will laboratory measurements of ozone in the presence of ices under Martian conditions.

The most readily accessible atmosphere for remote and in situ study of photochemistry is the atmosphere of the Earth. Laboratory measurements of reaction rates, photolytic cross section, three body reactions, and other properties tend to be at temperatures and under conditions reflecting those on Earth. Extrapolations are made to adapt them to Mars. For instance, much of what has been learned about odd hydrogen chemistry in the Earth's atmosphere has been applied to models of the Martian atmosphere [e.g. Nair *et al.* 1994, Lefévre *et al*. 2004]. Ozone has been shown to be an important tool for validating photochemical models of the Martian atmosphere, but the underlying assumptions about chemistry must also be validated. Laboratory measurements of chemical properties under Martian conditions are important for validating photochemical models, as well as expanding them to include processes such as heterogeneous chemistry.

II. Looking to the Future

Infrared heterodyne spectroscopy has been shown to be an important technique for studying Mars ozone. The technique is utilized for the study of other planetary atmospheres such as Jupiter [e.g. Kostiuk *et al.* 1987, Fast *et al.* 2002], Titan [e.g. Kostiuk *et al.* 1997, 2001, Livengood *et al.* 2002], and Venus [e.g. Goldstein *et al.* 1991]. In this work and in Fast *et al.* [2004], infrared heterodyne spectroscopy is shown to be a useful tool for uplooking studies of the atmosphere of Earth, passively reproducing the general distribution of ozone that must otherwise be retrieved through active and in situ means (Ch. 3).

Infrared heterodyne spectroscopy will continue to play an important role in the ongoing studies of planetary atmospheres, including that of Mars. Observations of ozone on Mars can be made from the surface of the Earth and are limited only by Doppler shift due to the relative motion of Mars, not by the need to go beyond Earth's atmosphere. Spacecraft missions that target atmospheric properties such as Mars Global Surveyor and Mars Express are providing a wealth of data with excellent spatial, diurnal, and orbital resolution, but there is always a need for Earth-based observations to validate and complement spacecraft data. Spacecraft have limited instrumentation and lifetimes, and sending spacecraft to Mars is an enormous (and not always successful) undertaking. Ongoing Earth-based observations of atmospheric constituents over longer time spans and with higher spectral resolution such as infrared heterodyne measurements of ozone will continue to improve the understanding of the stability of the Martian atmosphere.

This study has provided the most extensive database to date on spatial, seasonal, and orbital behavior of ozone on Mars. It has placed the odd hydrogen solution to the

CO_2 stability problem on firmer footing than was possible through previously published ozone data. Other than recent detections of H_2O_2 [Clancy *et al*. 2004, Encrenaz *et al*. 2004], odd hydrogen has not been directly observed in the atmosphere of Mars. Measurement of odd hydrogen species is an important next step. Photochemistry predicted an anticorrelation of ozone and water vapor abundance. Although that was seen in total column density, it was not to the extent originally predicted by photochemistry, and it became clear that constituent vertical distribution plays an important role. Photochemistry also predicts that ozone can trace odd hydrogen. This prediction has been utilized in this work in order to test the prevailing theory of Martian CO_2 stability. However, the only way to verify this prediction on Mars is to directly and contemporaneously measure both ozone and odd hydrogen abundances and their altitude distributions. If the current understanding of the relationship between ozone and odd hydrogen can be confirmed through measurement, that would provide further "stability" to the odd hydrogen solution to the problem of CO_2 stability in the atmosphere of Mars.

Appendix 1: Significance of the Reflected Solar Spectrum

The analysis of spectra of Earth's atmospheric transmittance backlit by the Moon in Ch. 3 assumes that contribution to the flat blackbody emission of the Moon by the reflected solar spectrum is negligible. This can be shown to be an acceptable assumption by comparing the reflected solar intensity with the blackbody intensity of the Moon in the 9.7 μm region explored in this work.

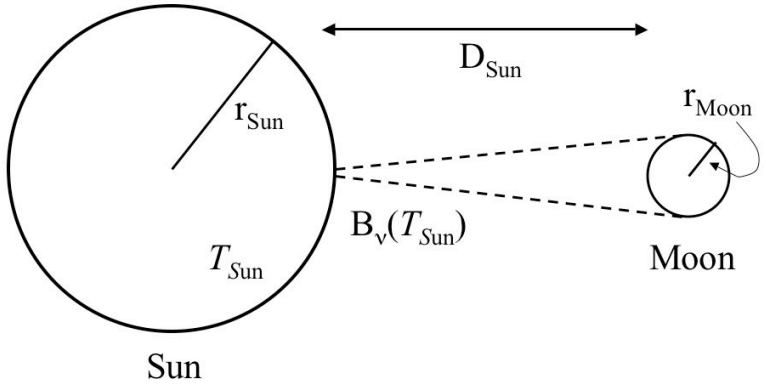


Figure A1.1. Geometry for determining intensity of the solar spectrum reflected from the Moon.

The reflected intensity of the Sun at a particular frequency, ν, can be expressed as:

$$I_\nu = \varepsilon \cdot B_\nu(T_{Sun}) \cdot \left[\pi r_{Sun}^2\right] \cdot \left[\frac{\pi r_{Moon}^2}{D_{Sun}^2}\right] \cdot \left[\frac{1}{2\pi}\right] \cdot \left[\frac{1}{\pi r_{Moon}^2}\right] \qquad \text{(A1.1)}$$

The emissivity of the Moon is ε. Each point on the Sun puts out $B_\nu(T_{Sun})$ ergs cm^{-2} s^{-1} $ster^{-1}$ wn^{-1} (wn is the inverse of wavelength in cm^{-1}). Multiplying by the cross-section area of the Sun, πr_{Sun}^2 cm^{-2}, gives the total energy coming from the sun in ergs s^{-1} $ster^{-1}$ wn^{-1}. The Moon subtends $\pi r_{Moon}^2/D_{Sun}^2$ steradians as seen from the Sun (at

a distance of D_{Sun}), and multiplying by that term gives the amount of energy hitting the Moon in ergs s^{-1} wn^{-1}. That energy is reflected by the Moon into 2π steradians by a surface that is πr_{Moon}^2 in cross-sectional area, and dividing by those terms results in the intensity of the reflected solar spectrum from the Moon in ergs cm^{-2} s^{-1} $ster^{-1}$ wn^{-1}. The expression in Eq. A1.1 reduces to:

$$I_\nu = \frac{1}{2}\varepsilon \cdot B_\nu(T_{Sun}) \cdot \left[\frac{r_{Sun}}{D_{Sun}}\right]^2 \qquad \text{(A1.2)}$$

Using a conservative emissivity of unity, the value for the intensity I_ν at 1031.4774 cm^{-1} (9.7 μm) is calculated to be 0.5 ergs cm^{-2} s^{-1} $ster^{-1}$ wn^{-1} (using $D_{Sun}=1.50\times10^8$ km, $r_{Sun}=6.96\times10^5$ km, $T_{Sun}=5800$ K). This can be compared to the blackbody emission from the moon at 380 K, which is 268 ergs cm^{-2} s^{-1} $ster^{-1}$ wn^{-1}. Therefore, the assumption that the reflected solar spectrum at 9.7 μm is negligible is good to a few tenths of a percent.

Appendix 2: Observational Details

The tables that follow contain details about the Martian ozone observations (e.g. dates, times, spatial coverage on Mars). The last table contains information about the aspect geometry of Mars for each observing run.

Table A2.1. Observational Details of Infrared Heterodyne Martian Ozone Campaigns (June 1888, February & July 1993)

filename	Ls	date	time	Air-mass	start time of first scan	start time of last scan	scan int. time	end time of last scan	total time of obs.	int. time (s)	sub-solar long offset	beam lat.	beam long. offset
MarsSS03Jun88LR.FITS	208	06/03/88	14:03:10	1.42	13:48:47	14:15:10	0:02:08	14:17:18	0:28:31	1024	46.5	-11.9	46.5
Mars60SA03Jun88LR.FITS	208	06/03/88	15:19:53	1.20	14:47:54	15:51:06	0:02:08	15:53:14	1:05:20	2048	46.5	-60.0	60
Mars80S03Jun88LR.FITS	208	06/03/88	17:58:31	1.32	17:09:13	18:47:25	0:02:08	18:49:33	1:40:20	3584	46.5	-80.0	20
Mars60SA04Jun88LR.FITS	208	06/04/88	15:46:00	1.24	14:04:00	17:45:00	0:02:08	17:47:08	3:43:08	6400	46.5	-60.0	60
Mars40S04Jun88LR.FITS	208	06/04/88	18:51:00	1.56	18:10:00	19:28:00	0:02:08	19:30:08	1:20:08	3072	46.5	-40.0	60
Mars40S05Jun88LR.FITS	208	06/05/88	14:43:00	1.30	13:44:00	16:13:00	0:02:08	16:15:08	2:31:08	3072	46.5	-40.0	60
Mars20N05Jun88LR.FITS	208	06/05/88	17:31:00	1.27	16:24:00	18:31:00	0:02:08	18:33:08	2:09:08	4352	46.5	20.0	35
Mars60SC06Jun88LR.FITS	208	06/06/88	14:22:46	1.32	13:31:59	15:11:56	0:02:08	15:14:04	1:42:05	4096	46.5	-60.0	-35
Mars60SB06Jun88LR.FITS	208	06/06/88	16:30:57	1.20	15:20:10	17:33:57	0:02:08	17:36:05	2:15:55	3584	46.5	-60.0	5
Mars20S06Jun88LR.FITS	208	06/06/88	18:27:33	1.44	17:40:58	19:09:03	0:02:08	19:11:11	1:30:13	3584	46.5	-20.0	55
MarsEq07Jun88LR.FITS	208	06/07/88	15:15:00	1.21	14:28:00	16:02:00	0:02:08	16:04:08	1:36:08	3840	46.5	0.0	45
Mars60SA07Jun88LR.FITS	208	06/07/88	17:53:00	1.31	17:05:00	18:42:00	0:02:08	18:44:08	1:39:08	3840	46.5	-60.0	60
Mars65N14Feb93LR.FITS	40	02/14/93	7:19:53	1.01	6:46:51	7:52:37	0:02:08	7:54:45	1:07:54	2560	-24.5	65.0	0
Mars65N15Feb93LR.FITS	40	02/15/93	5:40:11	1.10	5:29:48	5:48:28	0:02:08	5:50:36	0:20:48	1024	-24.5	65.0	0
Mars40N15Feb93LR.FITS	40	02/15/93	6:04:09	1.06	5:56:24	6:09:47	0:02:08	6:11:55	0:15:31	768	-24.5	40.0	-50
Mars55S15Feb93LR_1.FITS	40	02/15/93	7:19:54	1.01	6:50:06	7:41:16	0:02:08	7:43:24	0:53:18	1792	-24.5	-55.0	0
Mars55S15Feb93LR_2.FITS	40	02/15/93	8:13:08	1.03	8:02:40	8:21:29	0:02:08	8:23:37	0:20:57	1024	-24.5	-55.0	0
Mars20N15Feb93LR.FITS	40	02/15/93	8:45:30	1.07	8:29:43	8:59:41	0:02:08	9:01:49	0:32:06	1536	-24.5	20.0	-55
MarsEqL15Feb93LR.FITS	40	02/15/93	9:38:05	1.19	9:21:30	9:53:48	0:02:08	9:55:56	0:34:26	1536	-24.5	0.0	-55
Mars20S15Feb93LR.FITS	40	02/15/93	10:14:40	1.32	10:03:01	10:24:06	0:02:08	10:26:14	0:23:13	1024	-24.5	-20.0	-55
Mars40S15Feb93LR.FITS	40	02/15/93	11:00:54	1.59	10:38:23	11:18:31	0:02:08	11:20:39	0:42:16	1536	-24.5	-40.0	-45
MarsSSP15Feb93LR.FITS	40	02/15/93	11:46:44	2.08	11:28:57	12:01:48	0:02:08	12:03:56	0:34:59	1536	-24.5	16.3	-24.5
MarsSSP16Feb93LR.FITS	40	02/16/93	6:21:41	1.03	6:11:12	6:29:58	0:02:08	6:32:06	0:20:54	1029	-24.5	16.3	-24.5
Mars40N16Feb93LR.FITS	40	02/16/93	6:54:13	1.01	6:37:57	7:08:23	0:02:08	7:10:31	0:32:34	1540	-24.5	40.0	-50
Mars40S16Feb93LR.FITS	40	02/16/93	7:32:48	1.01	7:17:18	7:46:41	0:02:08	7:48:49	0:31:31	1540	-24.5	-40.0	-45
Mars65N16Feb93LR.FITS	40	02/16/93	8:18:53	1.04	7:57:46	8:38:13	0:02:08	8:40:21	0:42:35	2053	-24.5	65.0	0
Mars60N16Feb93LR.FITS	40	02/16/93	9:10:28	1.13	8:48:36	9:31:55	0:02:08	9:34:03	0:45:27	2051	-24.5	60.0	-35
MarsCtr04Jul93LR.FITS	102	07/04/93	4:08:25	2.15	5:38:22	6:59:35	0:02:09	7:01:44	1:23:22	2846	-32.9	24.7	0
Mars60N05Jul93LR.FITS	102	07/05/93	5:33:35	1.61	5:03:06	6:02:26	0:02:09	6:04:35	1:01:29	2072	-32.9	60.0	0
MarsSS05Jul93LR.FITS	102	07/05/93	6:35:23	2.46	6:08:14	7:03:38	0:02:09	7:05:47	0:57:33	2073	-32.9	25.0	-33
Mars60NW06Jul93LR.FITS	102	07/06/93	5:44:57	1.72	5:17:16	6:10:07	0:02:09	6:12:16	0:55:00	2073	-32.9	60.0	-40
Mars20S06Jul93LR.FITS	102	07/06/93	6:36:42	2.52	6:17:13	6:56:35	0:02:09	6:58:44	0:41:31	1556	-32.9	-20.0	0
MarsCtr07Jul93LR.FITS	102	07/07/93	3:07:55	1.06	2:27:50	3:46:11	0:02:09	3:48:20	1:20:30	3112	-32.9	24.7	0

Table A2.1. (continued)

filename	beam lat. range	beam long. range	local time	local time range	start cml	end cml	west beam edge W long. at start	east beam edge W long. at end	midpt. W long.	south beam edge lat.	north beam edge lat.	avg. alt. (km)	sdev alt. (km)
MarsSS03Jun88LR.FITS	10.3	14.9	12:00:00	0:59:36	86	92	125	146	136	-17	-7	2.9	1.5
Mars60SA03Jun88LR.FITS	8.0	24.2	11:06:00	1:36:48	99	115	147	187	167	-64	-56	1.9	0.6
Mars80S03Jun88LR.FITS	13.9	57.4	13:46:00	3:49:36	134	205	125	254	190	-87	-73	2.7	0.6
Mars60SA04Jun88LR.FITS	8.0	24.2	11:06:00	1:36:48	79	133	127	205	166	-64	-56	2.0	0.5
Mars40S04Jun88LR.FITS	9.4	19.1	11:06:00	1:16:24	139	158	189	228	209	-45	-35	1.7	0.6
Mars40S05Jun88LR.FITS	9.4	19.1	11:06:00	1:16:24	65	101	115	171	143	-45	-35	2.3	0.8
Mars20N05Jun88LR.FITS	15.6	15.5	12:46:00	1:02:00	103	135	130	178	154	12	28	-1.4	4.3
Mars60SC06Jun88LR.FITS	12.5	22.1	17:26:00	1:28:24	52	77	6	53	30	-66	-54	1.1	1.2
Mars60SB06Jun88LR.FITS	13.7	21.1	14:46:00	1:24:24	79	111	73	127	100	-67	-53	1.9	0.5
Mars20S06Jun88LR.FITS	9.8	17.0	11:26:00	1:08:00	113	134	160	198	179	-25	-15	1.1	0.9
MarsEq07Jun88LR.FITS	11.5	15.6	12:06:00	1:02:24	61	79	98	132	115	-6	6	5.6	2.1
Mars60SA07Jun88LR.FITS	8.0	24.2	11:06:00	1:36:48	94	118	142	190	166	-64	-56	1.9	0.6
Mars65N14Feb93LR.FITS	22.0	23.9	10:22:00	1:35:36	62	78	50	90	70	54	76	-4.0	0.7
Mars65N15Feb93LR.FITS	22.0	23.9	10:22:00	1:35:36	34	39	22	51	37	54	76	-4.7	0.2
Mars40N15Feb93LR.FITS	11.7	18.5	13:42:00	1:14:00	40	44	341	3	352	34	46	-2.1	2.4
Mars55S15Feb93LR_1.FITS	19.8	16.4	10:22:00	1:05:36	53	66	45	74	60	-65	-45	0.8	1.6
Mars55S15Feb93LR_2.FITS	19.8	16.4	10:22:00	1:05:36	71	76	63	84	74	-65	-45	1.8	0.8
Mars20N15Feb93LR.FITS	10.0	17.7	14:02:00	1:10:48	78	86	14	40	27	15	25	-2.7	0.7
MarsEqL15Feb93LR.FITS	9.9	17.6	14:02:00	1:10:24	90	99	26	53	40	-5	5	-0.8	1.6
Mars20S15Feb93LR.FITS	10.3	19.8	14:02:00	1:19:12	101	106	36	61	49	-25	-15	1.3	1.8
Mars40S15Feb93LR.FITS	14.1	19.5	13:22:00	1:18:00	109	119	54	84	69	-47	-33	3.1	1.0
MarsSSP15Feb93LR.FITS	10.0	11.3	12:00:00	0:45:12	121	130	91	111	101	11	21	3.5	2.7
MarsSSP16Feb93LR.FITS	10.0	11.3	12:00:00	0:45:12	35	40	5	21	13	11	21	-1.7	0.5
Mars40N16Feb93LR.FITS	11.7	18.5	13:42:00	1:14:00	41	49	342	8	355	34	46	-2.1	2.4
Mars40S16Feb93LR.FITS	14.1	19.5	13:22:00	1:18:00	51	59	356	24	10	-47	-33	0.8	2.9
Mars65N16Feb93LR.FITS	22.0	23.9	10:22:00	1:35:36	61	71	49	83	66	54	76	-4.2	0.5
Mars60N16Feb93LR.FITS	17.3	22.3	12:42:00	1:29:12	73	84	27	60	44	51	69	-4.5	0.3
MarsCtr04Jul93LR.FITS	24.3	26.8	9:48:24	1:47:12	151	172	138	185	162	13	37	-3.0	0.9
Mars60N05Jul93LR.FITS	30.5	48.3	9:48:24	3:13:12	133	148	109	172	141	45	75	-3.2	1.1
MarsSS05Jul93LR.FITS	24.0	31.0	12:00:24	2:04:00	149	163	101	146	123	13	37	1.8	3.3
Mars60NW06Jul93LR.FITS	24.0	50.5	12:28:24	3:22:00	127	140	62	125	94	48	72	-2.7	1.2
Mars20S06Jul93LR.FITS	37.1	26.6	9:48:24	1:46:24	141	152	128	165	147	-39	-1	1.5	1.4
MarsCtr07Jul93LR.FITS	24.3	26.8	9:48:24	1:47:12	76	96	63	109	86	13	37	1.2	1.5

Table A2.1. (continued)

filename	max alt. (km)	min alt. (km)	avg. pres. (mbar)	sdev pres. (mbar)	max pres. (mbar)	min pres. (mbar)	L.O. cm-1	rvel (km/s)	Dop. shift (MHz)
MarsSS03Jun88LR.FITS	7.8	-0.1	4.0	0.6	5.4	2.5	1031.4774	-12.07	1245.0
Mars60SA03Jun88LR.FITS	3.4	-0.7	4.4	0.3	5.8	3.8	1031.4774	-11.94	1231.6
Mars80S03Jun88LR.FITS	4.1	0.0	4.1	0.2	5.3	3.5	1031.4774	-11.64	1200.6
Mars60SA04Jun88LR.FITS	3.4	-0.7	4.4	0.2	5.8	3.8	1031.4774	-11.95	1232.6
Mars40S04Jun88LR.FITS	3.9	-0.8	4.5	0.3	5.8	3.6	1031.4774	-11.51	1187.2
Mars40S05Jun88LR.FITS	6.5	-1.0	4.3	0.4	5.9	2.8	1031.4774	-11.90	1227.5
Mars20N05Jun88LR.FITS	21.5	-4.8	6.5	1.6	8.7	0.6	1031.4774	-11.60	1196.5
Mars60SC06Jun88LR.FITS	5.0	-3.2	4.8	0.6	7.4	3.2	1031.4774	-11.89	1226.4
Mars60SB06Jun88LR.FITS	3.5	-0.1	4.4	0.2	5.4	3.8	1031.4774	-11.66	1202.7
Mars20S06Jun88LR.FITS	3.5	-2.2	4.8	0.4	6.6	3.8	1031.4774	-11.45	1181.0
MarsEq07Jun88LR.FITS	14.4	1.2	3.1	0.6	4.7	1.3	1031.4774	-11.75	1212.0
Mars60SA07Jun88LR.FITS	3.4	-0.7	4.4	0.3	5.8	3.8	1031.4774	-11.46	1182.1
Mars65N14Feb93LR.FITS	-1.3	-5.3	8.6	0.5	9.7	6.5	1035.4736	13.02	-1348.2
Mars65N15Feb93LR.FITS	-3.9	-5.6	9.1	0.1	10.0	8.5	1035.4736	13.03	-1349.2
Mars40N15Feb93LR.FITS	7.0	-5.9	7.3	1.5	10.3	2.8	1035.4736	13.07	-1353.4
Mars55S15Feb93LR_1.FITS	4.2	-3.9	5.3	0.9	8.4	3.7	1035.4736	13.21	-1367.9
Mars55S15Feb93LR_2.FITS	4.2	-1.1	4.8	0.4	6.3	3.7	1035.4736	13.31	-1378.2
Mars20N15Feb93LR.FITS	-0.5	-4.7	7.5	0.5	9.2	6.0	1035.4736	13.36	-1383.4
MarsEqL15Feb93LR.FITS	2.5	-4.7	6.3	1.0	9.2	4.4	1035.4736	13.45	-1392.7
Mars20S15Feb93LR.FITS	6.2	-4.7	5.1	1.0	9.1	3.1	1035.4736	13.50	-1397.9
Mars40S15Feb93LR.FITS	6.9	-1.1	4.2	0.4	6.4	2.9	1035.4736	13.55	-1403.1
MarsSSP15Feb93LR.FITS	18.5	1.5	4.1	0.7	4.9	0.9	1035.4736	13.60	-1408.2
MarsSSP16Feb93LR.FITS	-0.3	-3.8	6.8	0.4	8.3	5.9	1035.4736	13.29	-1376.1
Mars40N16Feb93LR.FITS	7.0	-5.9	7.2	1.5	10.3	2.8	1035.4736	13.35	-1382.4
Mars40S16Feb93LR.FITS	9.1	-7.4	5.5	2.0	12.0	2.3	1035.4736	13.42	-1389.6
Mars65N16Feb93LR.FITS	-2.5	-5.3	8.7	0.5	9.7	7.3	1035.4736	13.50	-1397.9
Mars60N16Feb93LR.FITS	-2.7	-5.6	8.9	0.3	10.0	7.5	1035.4736	13.59	-1407.2
MarsCtr04Jul93LR.FITS	7.8	-4.8	7.0	0.6	8.3	2.4	1035.4736	11.77	-1218.8
Mars60N05Jul93LR.FITS	5.0	-5.5	7.1	0.7	9.0	3.1	1035.4736	11.80	-1221.9
MarsSS05Jul93LR.FITS	21.5	-3.6	4.5	1.2	7.4	0.6	1035.4736	11.86	-1228.1
Mars60NW06Jul93LR.FITS	1.3	-5.2	6.8	0.8	8.7	4.5	1035.4736	11.73	-1214.6
Mars20S06Jul93LR.FITS	5.1	-2.8	4.5	0.7	6.8	3.1	1035.4736	11.77	-1218.8
MarsCtr07Jul93LR.FITS	14.7	-2.6	4.6	0.6	6.7	1.2	1035.4736	11.43	-1183.5

Table A2.2. Observational Details of Infrared Heterodyne Martian Ozone Campaigns (March 1995, March 1999)

filename	Ls	date	time	Air-mass	start time of first scan	start time of last scan	scan int. time	end time of last scan	total time of obs.	int. time (s)	sub-solar long offset	beam lat.	beam long. offset
MarsSS19Mar95LR.FITS	74	03/19/95	7:30:18	1.00	7:22:11	7:34:48	0:01:48	7:36:36	0:14:25	866	-26.3	24.4	-26.3
Mars60NA19Mar95LR_1.FITS	74	03/19/95	8:17:10	1.01	7:44:28	8:48:29	0:01:48	8:50:17	1:05:49	2168	-26.3	60.0	-55
Mars60NA19Mar95LR.FITS	74	03/19/95	9:13:15	1.12	7:44:28	10:44:47	0:01:48	10:46:35	3:02:07	3903	-26.3	60.0	-55
Mars60NA19Mar95LR_2.FITS	74	03/19/95	10:23:22	1.26	9:58:17	10:44:47	0:01:48	10:46:35	0:48:18	1734	-26.3	60.0	-55
Mars40N20Mar95LR.FITS	74	03/20/95	6:18:17	1.06	5:54:43	6:38:38	0:01:48	6:40:26	0:45:43	1742	-26.3	40.0	-65
Mars20N20Mar95LR.FITS	74	03/20/95	7:07:46	1.01	6:44:53	7:29:35	0:01:48	7:31:23	0:46:30	1735	-26.3	20.0	-65
Mars40S20Mar95LR.FITS	74	03/20/95	7:56:25	1.00	7:34:39	8:17:52	0:01:48	8:19:40	0:45:01	1735	-26.3	-40.0	-50
MarsEq20Mar95LR.FITS	74	03/20/95	8:46:03	1.04	8:29:39	9:02:13	0:01:48	9:04:01	0:34:22	1301	-26.3	0.0	-60
Mars20S20Mar95LR.FITS	74	03/20/95	11:03:09	1.48	10:48:09	11:16:29	0:01:48	11:18:17	0:30:08	1301	-26.3	-20.0	-25
MarsEq21Mar95LR.FITS	74	03/21/95	8:00:01	1.01	7:38:20	8:19:07	0:01:48	8:20:55	0:42:35	1744	-26.3	0.0	-60
Mars80N21Mar95LR.FITS	74	03/21/95	8:56:17	1.06	8:34:00	9:19:00	0:01:48	9:20:48	0:46:48	1732	-26.3	80.0	0
Mars60NA21Mar95LR.FITS	74	03/21/95	9:48:31	1.17	9:25:13	10:13:34	0:01:48	10:15:22	0:50:09	1731	-26.3	60.0	-55
Mars40N21Mar95LR.FITS	74	03/21/95	11:36:39	1.81	11:20:04	11:56:27	0:01:48	11:58:15	0:38:11	1300	-26.3	40.0	-65
MarsEq22Mar95LR.FITS	74	03/22/95	6:48:36	1.02	6:16:34	7:22:03	0:01:48	7:23:51	1:07:17	2601	-26.3	0.0	-60
Mars20N22Mar95LR.FITS	74	03/22/95	8:02:04	1.01	7:29:52	8:35:59	0:01:48	8:37:47	1:07:55	2600	-26.3	20.0	-65
Mars40N22Mar95LR.FITS	74	03/22/95	10:17:31	1.35	9:12:50	11:37:29	0:01:48	11:39:17	2:26:27	3684	-26.3	40.0	-65
Mars80N23Mar95LR.FITS	74	03/23/95	6:42:06	1.02	6:03:21	7:15:26	0:01:48	7:17:14	1:13:53	2819	-26.3	80.0	0
Mars60NB23Mar95LR.FITS	74	03/23/95	8:18:13	1.03	7:46:59	8:49:18	0:01:48	8:51:06	1:04:07	2602	-26.3	60.0	0
Mars40N23Mar95LR.FITS	74	03/23/95	9:27:42	1.14	9:03:36	9:50:36	0:01:48	9:52:24	0:48:48	2168	-26.3	40.0	-65
Mars40S23Mar95LR.FITS	74	03/23/95	10:16:15	1.30	9:57:30	10:33:19	0:01:48	10:35:07	0:37:37	1735	-26.3	-40.0	-25
R20_80N23Mar95LR.FITS	74	03/23/95	11:14:07	1.67	10:51:35	11:32:31	0:01:48	11:34:19	0:42:44	1735	-26.3	80.0	0
Mars20NB24Mar99LR.FITS	115	03/24/99	15:20:15	1.53	14:31:58	16:01:29	0:02:35	16:04:04	1:32:06	3588	22.0	20.0	0
Mars60NB25Mar99LR.FITS	115	03/25/99	11:28:05	1.38	9:58:49	12:58:09	0:02:35	13:00:44	3:01:55	4782	22.0	60.0	0
Mars40SB25Mar99LR.FITS	115	03/25/99	13:38:01	1.23	13:03:40	14:11:00	0:02:35	14:13:35	1:09:55	2990	22.0	-40.0	0
Mars20SB25Mar99LR.FITS	115	03/25/99	14:50:58	1.40	14:16:00	15:21:42	0:02:35	15:24:17	1:08:17	2990	22.0	-20.0	0
Mars20SB26Mar99LR.FITS	115	03/26/99	10:47:03	1.42	10:15:14	11:17:01	0:02:35	11:19:36	1:04:22	2990	22.0	-20.0	0
Mars40SB26Mar99LR.FITS	115	03/26/99	12:55:18	1.24	11:30:50	14:05:46	0:02:35	14:08:21	2:37:31	4285	22.0	-40.0	0
Mars40SA26Mar99LR.FITS	115	03/26/99	14:29:19	1.33	14:16:35	14:39:21	0:02:35	14:41:56	0:25:21	1245	22.0	-40.0	37
Mars00B26Mar99LR.FITS	115	03/26/99	15:02:59	1.46	14:50:37	15:13:05	0:02:35	15:15:40	0:25:03	1245	22.0	0.0	0
Mars40NB27Mar99LR.FITS	115	03/27/99	11:07:32	1.33	10:43:09	11:29:14	0:02:35	11:31:49	0:48:40	2487	22.0	40.0	0
Mars40SB29Mar99LR.FITS	115	03/29/99	10:41:30	1.39	10:10:15	11:09:30	0:02:35	11:12:05	1:01:50	3110	22.0	-40.0	0
Mars75NB29Mar99LR.FITS	115	03/29/99	11:54:22	1.22	11:15:19	12:31:48	0:02:35	12:34:23	1:19:04	3728	22.0	75.0	0
Mars20SB29Mar99LR.FITS	115	03/29/99	13:13:58	1.22	12:44:22	13:44:57	0:02:35	13:47:32	1:03:10	2800	22.0	-20.0	0
Mars40SA29Mar99LR.FITS	115	03/29/99	14:25:22	1.37	13:54:04	14:54:09	0:02:35	14:56:44	1:02:40	3109	22.0	-40.0	37
Mars40SC29Mar99LR.FITS	115	03/29/99	15:34:38	1.77	15:02:19	16:03:45	0:02:35	16:06:20	1:04:01	2795	22.0	-40.0	-37

Table A2.2. (continued)

filename	beam lat. range	beam long. range	local time	local time range	start cml	end cml	west beam edge W long. at start	east beam edge W long. at end	midpt. W long.	south beam edge lat.	north beam edge lat.	avg. alt. (km)	sdev alt. (km)
MarsSS19Mar95LR.FITS	9.6	11.7	11:59:50	0:46:48	287	292	255	272	263	20	29	-3.3	0.2
Mars60NA19Mar95LR_1.FITS	10.1	22.7	13:54:38	1:30:48	294	310	228	266	247	55	65	-4.0	0.2
Mars60NA19Mar95LR.FITS	10.1	22.7	13:54:38	1:30:48	294	338	228	294	261	55	65	-3.8	0.3
Mars60NA19Mar95LR_2.FITS	10.1	22.7	13:54:38	1:30:48	327	338	261	294	278	55	65	-3.6	0.2
Mars40N20Mar95LR.FITS	7.8	20.9	14:34:38	1:23:36	258	269	183	214	199	36	44	-3.2	0.5
Mars20N20Mar95LR.FITS	9.0	20.8	14:34:38	1:23:12	270	281	195	226	211	16	25	-0.3	1.6
Mars40S20Mar95LR.FITS	20.2	15.2	13:34:38	1:00:48	282	293	224	251	238	-50	-30	1.6	0.6
MarsEq20Mar95LR.FITS	10.0	20.4	14:14:38	1:21:36	296	304	226	254	240	-5	5	0.1	1.2
Mars20S20Mar95LR.FITS	13.2	19.0	11:54:38	1:16:00	330	337	296	322	309	-27	-13	1.7	1.1
MarsEq21Mar95LR.FITS	10.0	20.4	14:14:38	1:21:36	274	285	204	235	220	-5	5	-1.6	1.1
Mars80N21Mar95LR.FITS	14.1	52.9	10:14:38	3:31:36	288	299	262	325	294	73	87	-3.6	0.6
Mars60NA21Mar95LR.FITS	10.1	22.7	13:54:38	1:30:48	300	312	234	268	251	55	65	-4.0	0.2
Mars40N21Mar95LR.FITS	7.8	20.9	14:34:38	1:23:36	328	337	253	282	268	36	44	-3.9	0.5
MarsEq22Mar95LR.FITS	10.0	20.4	14:14:38	1:21:36	245	261	175	211	193	-5	5	-2.3	0.4
Mars20N22Mar95LR.FITS	9.0	20.8	14:34:38	1:23:12	263	280	188	225	207	16	25	-0.6	1.7
Mars40N22Mar95LR.FITS	7.8	20.9	14:34:38	1:23:36	288	324	213	269	241	36	44	-4.3	0.3
Mars80N23Mar95LR.FITS	14.1	52.9	10:14:38	3:31:36	233	251	207	277	242	73	87	-3.8	0.6
Mars60NB23Mar95LR.FITS	13.7	18.8	10:14:38	1:15:12	258	274	249	283	266	53	67	-3.8	0.2
Mars40N23Mar95LR.FITS	7.8	20.9	14:34:38	1:23:36	277	288	202	233	218	36	44	-3.7	0.5
Mars40S23Mar95LR.FITS	20.2	15.2	11:54:38	1:00:48	290	299	257	282	270	-50	-30	-3.1	2.2
R20_80N23Mar95LR.FITS	14.1	52.9	10:14:38	3:31:36	303	314	277	340	309	73	87	-3.6	0.7
Mars20NB24Mar99LR.FITS	9.1	9.2	13:28:00	0:36:48	268	290	263	295	279	15	25	-1.6	1.8
Mars60NB25Mar99LR.FITS	12.1	17.3	13:28:00	1:09:12	192	237	183	246	215	54	66	-3.9	0.2
Mars40SB25Mar99LR.FITS	15.8	11.2	13:28:00	0:44:48	237	254	231	260	246	-48	-32	1.1	0.7
Mars20SB25Mar99LR.FITS	10.1	9.0	13:28:00	0:36:00	255	272	251	277	264	-25	-15	2.1	0.7
Mars20SB26Mar99LR.FITS	10.1	9.0	13:28:00	0:36:00	187	203	183	208	195	-25	-15	0.9	0.9
Mars40SB26Mar99LR.FITS	15.8	11.2	13:28:00	0:44:48	206	245	200	251	226	-48	-32	1.6	0.6
Mars40SA26Mar99LR.FITS	17.0	16.3	11:00:00	1:05:12	246	252	275	297	286	-49	-32	-5.9	0.7
Mars00B26Mar99LR.FITS	9.4	8.8	13:28:00	0:35:12	254	260	250	264	257	-5	5	0.4	0.8
Mars40NB27Mar99LR.FITS	9.9	10.8	13:28:00	0:43:12	185	196	180	201	191	35	45	-3.2	0.6
Mars40SB29Mar99LR.FITS	15.8	11.2	13:28:00	0:44:48	159	174	153	180	167	-48	-32	1.8	0.9
Mars75NB29Mar99LR.FITS	17.9	32.9	13:28:00	2:11:36	175	194	159	210	185	66	84	-4.2	0.2
Mars20SB29Mar99LR.FITS	10.1	9.0	13:28:00	0:36:00	197	211	193	216	204	-25	-15	1.4	0.9
Mars40SA29Mar99LR.FITS	17.0	16.3	11:00:00	1:05:12	214	228	243	273	258	-49	-32	-0.6	2.2
Mars40SC29Mar99LR.FITS	17.0	16.3	15:56:00	1:05:12	230	245	185	216	201	-49	-32	1.6	0.6

Table A2.2. (continued)

filename	max alt. (km)	min alt. (km)	avg. pres. (mbar)	sdev pres. (mbar)	max pres. (mbar)	min pres. (mbar)	L.O. cm-1	rvel (km/s)	Dop. shift (MHz)
MarsSS19Mar95LR.FITS	-2.4	-4.2	7.8	0.2	8.6	7.2	1035.4736	11.34	-1174.2
Mars60NA19Mar95LR_1.FITS	-3.5	-4.4	8.4	0.1	8.7	8.0	1035.4736	11.44	-1184.6
Mars60NA19Mar95LR.FITS	-3.2	-4.6	8.2	0.2	8.9	7.7	1035.4736	11.54	-1194.9
Mars60NA19Mar95LR_2.FITS	-3.2	-4.6	8.0	0.2	8.9	7.7	1035.4736	11.66	-1207.4
Mars40N20Mar95LR.FITS	-0.1	-4.2	7.7	0.4	8.6	5.7	1035.4736	11.42	-1182.5
Mars20N20Mar95LR.FITS	12.2	-3.5	5.8	0.9	8.0	1.7	1035.4736	11.51	-1191.8
Mars40S20Mar95LR.FITS	3.8	-0.9	4.8	0.3	6.1	3.8	1035.4736	11.60	-1201.1
MarsEq20Mar95LR.FITS	2.7	-3.7	5.6	0.7	8.2	4.3	1035.4736	11.70	-1211.5
Mars20S20Mar95LR.FITS	4.5	-1.8	4.7	0.5	6.7	3.6	1035.4736	11.92	-1234.3
MarsEq21Mar95LR.FITS	2.4	-4.2	6.6	0.6	8.5	4.4	1035.4736	11.81	-1222.9
Mars80N21Mar95LR.FITS	-2.1	-4.7	8.0	0.5	9.0	6.9	1035.4736	11.91	-1233.2
Mars60NA21Mar95LR.FITS	-3.5	-4.4	8.4	0.1	8.7	8.0	1035.4736	12.00	-1242.6
Mars40N21Mar95LR.FITS	-2.4	-5.9	8.3	0.4	10.1	7.2	1035.4736	12.15	-1258.1
MarsEq22Mar95LR.FITS	-0.9	-4.2	7.1	0.3	8.5	6.1	1035.4736	11.87	-1229.1
Mars20N22Mar95LR.FITS	12.2	-3.4	6.0	0.9	7.9	1.7	1035.4736	12.01	-1243.6
Mars40N22Mar95LR.FITS	-3.4	-5.9	8.6	0.3	10.1	7.9	1035.4736	12.24	-1267.4
Mars80N23Mar95LR.FITS	-2.1	-4.4	8.2	0.4	8.7	6.9	1035.4736	12.04	-1246.7
Mars60NB23Mar95LR.FITS	-3.3	-4.6	8.2	0.2	8.9	7.8	1035.4736	12.22	-1265.3
Mars40N23Mar95LR.FITS	-2.3	-4.9	8.1	0.4	9.1	7.1	1035.4736	12.35	-1278.8
Mars40S23Mar95LR.FITS	2.7	-6.6	7.8	1.7	10.9	4.3	1035.4736	12.42	-1286.1
R20_80N23Mar95LR.FITS	-2.1	-4.7	8.0	0.5	9.0	6.9	1035.4736	12.50	-1294.3
Mars20NB24Mar99LR.FITS	2.1	-3.7	5.9	1.0	7.1	4.0	1031.4774	-11.50	1186.2
Mars60NB25Mar99LR.FITS	-3.1	-5.0	7.3	0.1	8.2	6.7	1031.4774	-11.70	1206.8
Mars40SB25Mar99LR.FITS	3.8	-2.1	4.4	0.3	6.1	3.4	1031.4774	-11.45	1181.0
Mars20SB25Mar99LR.FITS	4.5	-1.4	4.0	0.3	5.7	3.2	1031.4774	-11.31	1166.6
Mars20SB26Mar99LR.FITS	3.5	-2.2	4.5	0.4	6.1	3.5	1031.4774	-11.53	1189.3
Mars40SB26Mar99LR.FITS	3.9	-0.9	4.2	0.3	5.4	3.4	1031.4774	-11.29	1164.5
Mars40SA26Mar99LR.FITS	-1.9	-7.4	9.0	0.5	10.4	6.0	1031.4774	-11.10	1144.9
Mars00B26Mar99LR.FITS	3.2	-2.2	4.8	0.4	6.1	3.6	1031.4774	-11.05	1139.8
Mars40NB27Mar99LR.FITS	-0.1	-4.0	6.8	0.4	7.3	5.0	1031.4774	-11.25	1160.4
Mars40SB29Mar99LR.FITS	4.2	-1.0	4.1	0.4	5.5	3.3	1031.4774	-10.79	1113.0
Mars75NB29Mar99LR.FITS	-3.1	-5.7	7.5	0.2	8.7	6.8	1031.4774	-10.66	1099.6
Mars20SB29Mar99LR.FITS	3.5	-2.2	4.3	0.4	6.1	3.5	1031.4774	-10.49	1082.0
Mars40SA29Mar99LR.FITS	3.8	-5.7	5.4	1.3	8.8	3.4	1031.4774	-10.36	1068.6
Mars40SC29Mar99LR.FITS	3.9	-0.8	4.2	0.2	5.3	3.3	1031.4774	-10.24	1056.2

Table A2.3. Observational Details of Infrared Heterodyne Martian Ozone Campaigns (June & November 2003)

filename	Ls	date	time	Air-mass	start time of first scan	start time of last scan	scan int. time	end time of last scan	total time of obs.	int. time (s)	sub-solar long offset	beam lat.	beam long. offset
Mars10Jun03_40N_MGS_LR.FITS	202	06/10/03	12:14:46	1.83	11:29:20	12:58:04	0:01:17	12:59:21	1:30:01	4293	41.0	40.0	11
Mars10Jun03_0S_55E_LR.FITS	202	06/10/03	14:24:30	1.26	13:43:17	15:07:44	0:01:17	15:09:01	1:25:44	3067	41.0	0.0	55
Mars10Jun03_60S_MGS_LR.FITS	202	06/10/03	14:25:20	1.32	13:01:46	13:35:21	0:01:17	13:36:38	0:34:52	3680	41.0	-60.0	11
Mars10Jun03_60S_MGS_LR.FITS	202	06/10/03	14:25:20	1.32	15:11:34	15:52:10	0:01:17	15:53:27	0:41:53	3680	41.0	-60.0	11
Mars12Jun03_40S_60E_LR.FITS	202	06/12/03	12:42:59	1.61	11:38:06	13:42:48	0:01:17	13:44:05	2:05:59	5520	41.0	-40.0	60
Mars12Jun03_60S_60E_LR.FITS	202	06/12/03	15:00:59	1.24	14:03:50	15:51:58	0:01:17	15:53:15	1:49:25	4906	41.0	-60.0	60
Mars14Jun03_20N_45E_LR.FITS	202	06/14/03	12:47:09	1.54	11:50:47	13:38:08	0:02:33	13:40:41	1:49:54	6135	41.0	20.0	45
Mars14Jun03_20S_60E_LR.FITS	202	06/14/03	15:05:14	1.24	14:00:16	16:04:32	0:02:33	16:07:05	2:06:49	6743	41.0	-20.0	60
Mars16Jun03_60S_60E_LR.FITS	202	06/16/03	14:07:15	1.32	12:19:41	15:49:37	0:02:33	15:52:10	3:32:29	11034	41.0	-60.0	60
Mars01Nov03_20N_45W_LR.FITS	291	11/01/03	9:54:57	2.10	9:17:45	10:31:18	0:04:16	10:35:34	1:17:49	3067	-41.9	20.0	-45
Mars02Nov03_60S_72W_LR.FITS	291	11/02/03	8:42:07	1.57	7:19:06	10:08:54	0:04:16	10:13:10	2:54:04	4599	-41.9	-60.0	-72
Mars03Nov03_20S_67W_LR.FITS	291	11/03/03	9:04:27	1.64	8:08:01	9:51:55	0:04:16	9:56:11	1:48:10	4599	-41.9	-20.0	-67

Table A2.3. (continued)

filename	beam lat. range	beam long. range	local time	local time range	start cml	end cml	west beam edge W long. at start	east beam edge W long. at end	midpt. W long.	south beam edge lat.	north beam edge lat.	avg. alt. (km)	sdev alt. (km)
Mars10Jun03_40N_MGS_LR.FITS	18.4	11.1	13:59:53	0:44:24	145	167	150	184	167	31	49	-3.6	0.1
Mars10Jun03_0S_55E_LR.FITS	9.2	15.5	11:03:53	1:02:00	178	199	225	262	244	-5	5	0.2	1.2
Mars10Jun03_60S_MGS_LR.FITS	10.3	16.3	13:59:53	1:05:12	167	176	170	195	183	-65	-55	1.9	0.5
Mars10Jun03_60S_MGS_LR.FITS	10.3	16.3	13:59:53	1:05:12	199	209	202	228	215	-65	-55	1.7	0.6
Mars12Jun03_40S_60E_LR.FITS	6.2	15.2	10:43:53	1:00:48	128	159	180	227	204	-43	-37	1.6	0.6
Mars12Jun03_60S_60E_LR.FITS	7.0	17.9	10:43:53	1:11:36	163	190	214	259	237	-64	-57	1.8	0.7
Mars14Jun03_20N_45E_LR.FITS	11.9	14.6	11:43:53	0:58:24	112	139	150	191	171	14	26	-3.1	0.4
Mars14Jun03_20S_60E_LR.FITS	6.9	15.0	10:43:53	1:00:00	143	174	196	242	219	-23	-17	2.0	0.7
Mars16Jun03_60S_60E_LR.FITS	7.0	17.9	10:43:53	1:11:36	100	152	151	221	186	-64	-57	1.9	0.6
Mars01Nov03_20N_45W_LR.FITS	11.7	13.3	12:12:24	0:53:12	231	250	179	212	196	14	26	-1.7	1.3
Mars02Nov03_60S_72W_LR.FITS	4.0	17.2	14:00:24	1:08:48	192	235	111	172	142	-62	-58	2.0	0.5
Mars03Nov03_20S_67W_LR.FITS	6.1	16.3	13:40:24	1:05:12	195	220	120	161	141	-23	-17	2.5	1.4

Table A2.3. (continued)

filename	max alt. (km)	min alt. (km)	avg. pres. (mbar)	sdev pres. (mbar)	max pres. (mbar)	min pres. (mbar)	L.O. cm-1	rvel (km/s)	Dop. shift (MHz)
Mars10Jun03_40N_MGS_LR.FITS	-2.5	-4.1	7.7	0.1	8.0	6.9	1031.4774	-11.85	1222.3
Mars10Jun03_0S_55E_LR.FITS	3.2	-3.7	5.3	0.7	7.8	3.9	1031.4774	-11.64	1200.6
Mars10Jun03_60S_MGS_LR.FITS	3.4	0.4	4.4	0.2	5.2	3.8	1031.4774	-11.64	1200.6
Mars10Jun03_60S_MGS_LR.FITS	3.1	-0.6	4.5	0.3	5.7	3.9	1031.4774	-11.64	1200.6
Mars12Jun03_40S_60E_LR.FITS	3.9	0.1	4.5	0.3	5.3	3.6	1031.4774	-11.65	1201.7
Mars12Jun03_60S_60E_LR.FITS	3.5	-0.6	4.5	0.3	5.7	3.8	1031.4774	-11.41	1176.9
Mars14Jun03_20N_45E_LR.FITS	-1.2	-4.8	7.3	0.3	8.6	6.0	1031.4774	-11.48	1184.1
Mars14Jun03_20S_60E_LR.FITS	3.5	-1.1	4.4	0.3	6.0	3.8	1031.4774	-11.24	1159.4
Mars16Jun03_60S_60E_LR.FITS	3.4	-0.7	4.4	0.2	5.8	3.8	1031.4774	-11.18	1153.2
Mars01Nov03_20N_45W_LR.FITS	6.3	-4.5	7.1	0.8	9.3	3.2	1035.4736	11.91	-1233.2
Mars02Nov03_60S_72W_LR.FITS	3.3	-0.3	4.9	0.2	6.1	4.3	1035.4736	11.91	-1233.2
Mars03Nov03_20S_67W_LR.FITS	6.8	-0.8	4.7	0.6	6.5	3.0	1035.4736	12.04	-1246.7

Table A2.4. Mars Aspect Geometry Information

Aspect Information	June 3-7, 1988	Feb. 14-16, 1993	July 4-7, 1993	March 17-23, 1995	March 24-29, 1999	June 10-16, 2003	Nov. 1-3, 2003
diameter (arcsec)	10.6	11.6	4.6	11.6	13.3	13.62	14.75
SubEarth Lat. (deg)	-23.2	3.7	24.7	16.8	15.3	-21	-23.7
North Pole Position Angle (CCW)	344.8	338.2	14.3	359.5	38.3	351.8	345.3
SubSolar Long. (deg)	-11.9	16.3	24.8	24.4	23	-8.8	-23.7
SubSolar Long. Offset (deg)	46.5	-24.4	-32.9	-26.3	21.1	41	-41.9
Ls (deg)	208	40	102	74	115	202	291

Appendix 3: Analysis Details

The tables that follow contain details of the radiative transfer analysis of infrared heterodyne spectra of Mars ozone.

Table A3.1. June 1988 Analysis Details

filename	Reso-lution. (MHz)	Fit Doppler Shift	1 sig	Fit Scale Factor	1 sig	MGS Tsurf K	Fit Tsurf K	1 sig	Fit Tlayer1 K	MGS delta K	1 sig	O3 MF x1E-8	1 sig	O3 CD mu-atm	1 sig	Terr CO2 Scale Factor	1 sig	Terr O3 Scale Factor	1 sig
:Mars20N05Jun88LR:	25	3.7	3.7	1.61	0.07	269.4	268.7	2.1	230.1	0.6	1.9	1.19	0.49	1.02	0.42	0.75	0	1.02	0.01
:Mars20N05Jun88LR:	5	8.8	3.5	1.45	0.06	269.4	265.8	2.3	232.4	3	2.5	1.21	0.31	1.03	0.26	0.64	0.13	1.09	0.02
:MarsEq07Jun88LR:	25	0.7	2.9	1.33	0.09	285.7	271.2	3.2	234	-5.9	2.5	0.94	0.62	0.72	0.47	1.28	0.06	1.02	0.02
:MarsEq07Jun88LR:	5	2.3	2.8	1.27	0.05	285.7	269.3	2.1	237	-2.9	2.9	0.71	0.33	0.54	0.25	1.42	0.08	1.01	0.02
:MarsSS03Jun88LR:	25	-0.9	5	1.05	0.13	285.7	273.3	6.6	227.1	-12.8	2.8	0.86	0.61	0.74	0.52	0.94	0.21	1.01	0.02
:MarsSS03Jun88LR:	5	-1.1	5.2	0.99	0.12	285.7	273.2	6.2	232.4	-7.5	3.8	0.81	0.44	0.7	0.38	1.27	0.19	1.04	0.02
:Mars20S06Jun88LR:	25	4.8	3.1	2.81	0.12	287.1	301.8	2.1	258.6	20.6	2.2	1.74	0.73	1.07	0.44	0.53	0.08	1.09	0.02
:Mars20S06Jun88LR:	5	3.8	3.2	2.88	0.16	287.1	303.3	3.6	258.2	20.2	2.8	1.39	0.45	0.85	0.28	0.61	0.14	1.09	0.02
:Mars40S04Jun88LR:	25	-7.2	4.3	2.3	0.35	280.5	286	8.1	233.8	1.7	3.6	1.66	1.01	1.08	0.66	0.58	0.15	1.02	0.02
:Mars40S04Jun88LR:	5	-10.4	3.5	2.24	0.27	280.5	284.8	6.3	237.2	5.1	3	1.36	0.47	0.89	0.31	0.73	0.06	1	0.02
:Mars40S05Jun88LR:	25	19.1	2.9	3.43	0.35	280.5	282.6	5.2	232.7	0.5	1.7	1.39	0.67	0.91	0.44	1.06	0.02	1.07	0.02
:Mars40S05Jun88LR:	5	18.8	2.5	3.47	0.32	280.5	282.7	4.8	233.2	1	1.8	0.6	0.3	0.39	0.2	1.11	0.08	1.06	0.01
:Mars60SA04Jun88LR_45:	25	-0.1	2.9	0.8	0.06	244.6	255.9	2.9	224.4	12	3.5	1.44	0.73	0.96	0.49	0.14	0.02	1.2	0.02
:Mars60SA04Jun88LR_46:	25	6.8	2.6	1.02	0.05	244.6	255.8	2.1	225.3	12.8	2.7	1.9	0.74	1.26	0.5	0.82	0.01	1.09	0.02
:Mars60SB06Jun88LR:	25	-0.2	1.8	1.32	0.06	244.6	267.1	2	233.2	20.7	2.2	2.04	0.84	1.36	0.56	1.18	0.11	1.02	0.02
:Mars60SB06Jun88LR:	5	1.6	2	1.25	0.07	244.6	265.6	2.5	233.4	20.9	3	2.63	0.47	1.75	0.31	1.23	0.08	1.04	0.02
:Mars60SC06Jun88LR:	25	2.7	2.8	1.16	0.08	244.6	245.9	3.1	229.8	17.3	6.4	2.45	1.19	1.63	0.79	0.94	0.08	1.07	0.02
:Mars60SC06Jun88LR:	5	2.3	2.9	1.16	0.09	244.6	245.8	3.5	230.1	17.6	7	2.18	0.65	1.45	0.43	0.97	0.16	1.07	0.02
:Mars80S03Jun88LR:	25	-8.8	3.7	1.71	0.21	153.8	249.8	5.6	237.7	38.7	9.6	1.75	1.27	1.09	0.8	0.92	0.1	1.03	0.02
:Mars80S03Jun88LR:	5	-5.6	4.1	1.65	0.02	153.8	249.8	0	243.3	44.2	3	1.55	0.91	0.97	0.57	0.88	0.03	1.1	0.03

Table A3.2. February 1993 Analysis Details

filename	Reso-lution. (MHz)	Fit Doppler Shift	1 sig	Fit Scale Factor	1 sig	MGS Tsurf K	Fit Tsurf K	1 sig	Fit Tlayer1 K	MGS delta K	1 sig	O3 MF x1E-8	1 sig	O3 CD mu-atm	1 sig	Terr CO2 Scale Factor	1 sig	Terr O3 Scale Factor	1 sig
:Mars40S16Feb93LR:	25	0	0	2.01	1.12	222.2	227.4	19.8	213.8	33.9	22.1	20.1	8.73	13.62	5.91	0.91	0.33	1	0
:Mars40S16Feb93LR:	5	0	0	1.99	0.05	222.2	227.4	0	212.9	33	7.4	15.85	6.22	10.74	4.21	1.01	0.16	1	0
:MarsEqL15Feb93LR:	25	0	0	3.34	1.6	269.4	259.3	21.9	250.2	30.4	34.8	7.71	5.06	6.38	4.18	0.86	0.09	1	0
:MarsEqL15Feb93LR:	5	0	0	3.24	0.6	269.4	259.1	8.6	242.7	22.9	19.2	8.72	3.14	7.21	2.59	0.98	0.09	1	0
:MarsSSP16Feb93LR:	25	0	0	1.44	0.41	271.9	285.6	15.3	250.5	33.1	8.8	6.52	2.69	5.92	2.45	1.72	0.17	1.04	0.06
:MarsSSP16Feb93LR:	5	0	0	1.6	0.48	271.9	289.7	16.9	248.5	31.1	7.6	6.71	1.09	6.1	0.99	1.66	0.22	0.99	0.06
:MarsSSP15Feb93LR:	25	0	0	1	0.74	271.9	267.6	34.3	206.1	-11.3	5.2	2.67	1.11	2.42	1.01	1.22	0.08	1.05	0.03
:MarsSSP15Feb93LR:	5	0	0	0.96	0.02	271.9	267.5	0	205.6	-11.8	5.7	3.37	0.56	3.06	0.51	1.27	0.05	1.08	0.03
:Mars20N15Feb93LR:	25	0	0	2.65	0.66	272.6	266.9	12.6	248.8	31.8	13.9	6.33	2.72	5.9	2.53	1.44	0.18	1.04	0.07
:Mars20N15Feb93LR:	5	0	0	2.85	0.13	272.6	266.9	0	240.4	23.4	12.1	4.71	1.23	4.4	1.15	1.16	0.29	0.95	0.05
:Mars40N16Feb93LR:	25	0	0	2.16	0.45	266.6	271.7	11	234.1	17.8	6.7	2.36	1.14	2.32	1.12	1.98	0.22	1.07	0.03
:Mars40N16Feb93LR:	5	0	0	2.15	0.67	266.6	270.5	15.1	232.5	16.1	6.4	3.02	0.58	2.97	0.57	1.87	0.13	1.07	0.07
:Mars60N16Feb93LR:	25	0	0	1.59	0.25	247.6	237.7	7.1	219.3	6.2	10.6	3.49	1.19	4	1.37	1.22	0.19	1	0
:Mars60N16Feb93LR:	5	0	0	1.65	0.01	247.6	237.7	0	216.3	3.2	9.3	4.54	0.95	5.2	1.09	1.03	0.01	1	0
:Mars65N14Feb93LR:	25	0	0	1.07	0.13	230.9	223.9	4.2	210	-0.5	10.6	3.89	1.28	4.63	1.52	1	0	1	0
:Mars65N14Feb93LR:	5	0	0	1.1	0.13	230.9	225.5	4	209.8	-0.6	8.9	4.86	0.97	5.78	1.15	1	0	1	0
:Mars65N16Feb93LR:	25	0	0	2.29	0.33	230.9	249.3	7.4	221.1	10.6	6.2	3.98	1.37	4.73	1.63	1.51	0.24	1	0
:Mars65N16Feb93LR:	5	0	0	2.58	0.11	230.9	249.3	0	204	-6.5	9.2	3	0.61	3.56	0.72	0.96	0.3	1	0

Table A3.3. July 1993 Analysis Details

filename	Reso-lution. (MHz)	Fit Doppler Shift	1 sig	Fit Scale Factor	1 sig	MGS Tsurf K	Fit Tsurf K	1 sig	Fit Tlayer1 K	MGS delta K	1 sig	O3 MF x1E-8	1 sig	O3 CD mu-atm	1 sig	Terr CO2 Scale Factor	1 sig	Terr O3 Scale Factor	1 sig
:Mars60N05Jul93LR:	25	-12.5	11.9	1.74	0.38	265.5	255.3	13.2	235.9	13.4	11.8	9.16	4.8	9.78	5.12	2.35	0.41	1.02	0.05
:MarsCtr04Jul93LR:	25	-12	16.1	1.86	0.4	271.2	259.1	9.5	228.2	20.3	8.3	1.83	5.52	1.56	4.72	1.37	0.1	0.83	0.05
:MarsCtr07Jul93LR:	25	10.6	5.1	1.79	0.32	271.2	252.5	7.5	217.2	9.3	5.3	4.55	2.44	3.89	2.09	1.06	0.25	1.08	0.04
:MarsCtr07Jul93LR:	5	11.1	0	1.88	0.36	271.2	254.5	7.9	216.7	8.8	4.4	3.95	1.31	3.38	1.12	1.09	0.04	1.07	0.03
:MarsSS05Jul93LR:	25	-11.1	13.4	1.67	0.35	271.2	268.1	11.9	247.5	39.5	10.2	5.08	4.54	4.35	3.88	1.3	0.15	0.87	0.05

Table A3.4. March 1995 Analysis Details

filename	Reso-lution. (MHz)	Fit Doppler Shift	1 sig	Fit Scale Factor	1 sig	MGS Tsurf K	Fit Tsurf K	1 sig	Fit Tlayer1 K	MGS delta K	1 sig	O3 MF x1E-8	1 sig	O3 CD mu-atm	1 sig	Terr CO2 Scale Factor	1 sig	Terr O3 Scale Factor	1 sig
:Mars40S20Mar95LR:	25	0	0	1.1	0.57	199.1	210.1	14.6	178.7	-2	7.5	2.53	1.67	1.96	1.29	1.4	0.45	0.98	0.07
:Mars40S20Mar95LR:	5	0	0	1.22	0.97	199.1	209.9	22.5	176.7	-4	8.9	1.99	0.89	1.54	0.69	0.98	0.39	0.88	0.08
:Mars20S20Mar95LR:	25	0	0	1.95	1.25	242.3	248.1	25.3	211.2	12.1	9.8	5.01	3.99	3.25	2.59	1	0	1.04	0.07
:Mars20S20Mar95LR:	5	0	0	2	0.07	242.3	248.1	0	212.8	13.6	14.2	5.15	2.53	3.35	1.64	1	0	1.01	0.07
:MarsEq20Mar95LR:	25	0	0	1.34	0.21	261	237.5	6.7	214.9	6	9.9	3.03	1.62	2.32	1.24	1.04	0.22	1	0
:MarsEq20Mar95LR:	5	0	0	1.41	0.26	261	239.6	7.7	215.1	6.1	11.9	5.48	1.63	4.2	1.25	0.99	0.17	1	0
:MarsEq21Mar95LR:	25	0	0	1.48	0.22	261	263.3	8.5	230.3	21.4	5.4	4.49	1.49	3.44	1.14	1.45	0.31	0.99	0.04
:MarsEq21Mar95LR:	5	0	0	1.48	0.25	261	263.2	7.8	231.3	22.3	5.2	4.95	0.82	3.79	0.62	1.41	0.15	1.01	0.05
:Mars20N20Mar95LR:	25	0	0	1.88	0.28	269.1	254.1	9.9	227.8	18.8	7.6	3.77	2	3.43	1.82	1.38	0.51	1	0
:Mars20N20Mar95LR:	5	0	0	2.1	0.07	269.1	254.1	0	238.6	29.6	5.9	7.9	1.62	7.17	1.47	0.43	0.24	1	0
:Mars20N22Mar95LR:	25	0	0	2.47	0.23	269.1	239	3.9	212	3	5	2.56	0.87	2.33	0.79	1.09	0.19	1	0
:Mars20N22Mar95LR:	5	0	0	2.47	0	269.1	239	0	212	3	0	2.2	0.65	2	0.59	1	0	1	0
:MarsSS19Mar95LR:	25	0	0	1.29	0.16	270.6	270.3	7.5	233.9	22.6	4	6.34	3.02	5.78	2.75	1.12	0.26	0.97	0.03
:MarsSS19Mar95LR:	5	0	0	1.43	0.23	270.6	273.6	8	230.1	18.8	4.5	4.81	1.06	4.39	0.96	1.03	0.14	0.9	0.03
:Mars40N20Mar95LR:	25	0	0	1.36	0.12	269.6	243.6	5	220.9	1.7	4.7	3.03	1.13	3.06	1.14	1.15	0.26	1	0
:Mars40N20Mar95LR:	5	0	0	1.54	0.12	269.6	250.4	5	227	7.8	4.5	5.49	0.61	5.54	0.61	1.3	0.24	1	0
:Mars40N21Mar95LR:	25	0	0	2.57	0.46	269.6	264	8.4	228.1	8.9	7.6	2.9	2.53	2.92	2.55	1.51	0.12	1	0
:Mars40N21Mar95LR:	5	0	0	2.57	0.77	269.6	263.6	18.3	226.4	7.2	15.2	1.63	1.56	1.65	1.58	1.56	0.34	1	0
:Mars40N22Mar95LR:	25	0	0	2.19	0.68	269.6	246.4	12.7	237.9	18.6	18.4	1.9	2.08	1.92	2.1	0.45	0.04	1.04	0.08
:Mars40N22Mar95LR:	5	0	0	2.21	1.2	269.6	245.8	21.9	241	21.8	30.5	2.4	1.56	2.42	1.57	0.29	0.01	1.07	0.05
:Mars40N23Mar95LR:	25	0	0	2.78	0.27	269.6	296.4	8.8	249.9	30.6	3.8	3.57	1.26	3.6	1.27	2.53	0.32	1	0
:Mars40N23Mar95LR:	5	0	0	2.73	0.29	269.6	294.3	9.6	251.7	32.4	3.6	4.31	0.67	4.35	0.68	2.44	0.33	1	0
:Mars60NA19Mar95LR_1:	25	0	0	1.28	0.17	262.3	259.6	7.7	227.8	4.4	3.3	2.11	1.1	2.43	1.27	1.55	0.33	0.94	0.03
:Mars60NA19Mar95LR_1:	5	0	0	1.3	0.19	262.3	257.8	7.8	226.5	3.1	2.2	1.6	0.45	1.84	0.51	1.32	0.25	0.91	0.04
:Mars60NA21Mar95LR:	25	0	0	1.84	0.25	262.3	260.8	6.1	229.3	6	3.5	3.51	1.04	4.04	1.2	1.4	0.1	0.94	0.04
:Mars60NA21Mar95LR:	5	0	0	1.82	0.34	262.3	258.8	8.8	228.9	5.5	5.1	2.58	0.73	2.97	0.84	1.28	0.2	0.93	0.05
:Mars60NB23Mar95LR:	25	0	0	1.35	0.11	262.3	259.5	5.1	226.1	2.8	3.8	2.57	1.02	2.95	1.17	1.1	0.31	1	0
:Mars60NB23Mar95LR:	5	0	0	1.36	0.12	262.3	259.1	3.8	225.9	2.5	3.9	1.69	0.59	1.95	0.68	1.04	0.01	1	0
:Mars80N23Mar95LR:	5	0	0	1.32	0.18	194.1	227.7	4.9	213.2	-4	15.2	1.73	0.68	2.1	0.83	1	0	1	0

Table A3.5. March 1999 Analysis Details

filename	Reso-lution. (MHz)	Fit Doppler Shift	1 sig	Fit Scale Factor	1 sig	MGS Tsurf K	Fit Tsurf K	1 sig	Fit Tlayer1 K	MGS delta K	1 sig	O3 MF x1E-8	1 sig	O3 CD mu-atm	1 sig	Terr CO2 Scale Factor	1 sig	Terr O3 Scale Factor	1 sig
:Mars75NB29Mar99LR:	25	-4.5	3.2	1.18	0.08	250	248.2	2.3	212.3	-7.5	2	1.79	0.61	1.82	0.62	0.59	0.13	1.05	0.03
:Mars75NB29Mar99LR:	5	-5.9	2.6	1.16	0.07	250	248.7	2.4	213.5	-6.3	3	1.77	0.35	1.81	0.36	0.65	0.23	1.09	0.02
:Mars60NB25Mar99LR:	25	-0.7	3.6	1.41	0.16	263.5	266.5	5.2	219.3	-4.7	2.1	1.31	0.61	1.3	0.6	1.57	0.05	1.31	0.02
:Mars60NB25Mar99LR:	5	2	3.1	1.34	0.15	263.5	265	5.1	220.6	-3.4	2.3	1.55	0.35	1.54	0.35	1.33	0.16	1.34	0.03
:Mars40NB27Mar99LR:	5	-9.1	6.6	1.81	0.38	272.8	266.5	9.8	222.6	0.5	5.1	0.36	0.87	0.34	0.8	1.19	0.3	1.25	0.05
:Mars20NB24Mar99LR:	25	4.8	2.6	1.06	0.3	269.2	257.2	12.1	212.5	-0.9	3.5	4.42	1.63	3.54	1.31	2.28	0.21	1.18	0.03
:Mars20NB24Mar99LR:	5	8.3	2.5	1.08	0.32	269.2	257.7	12.9	212.6	-0.8	3.6	5.15	0.84	4.13	0.67	2.16	0.07	1.17	0.02
:Mars00B26Mar99LR:	25	-5	4	1.69	0.74	261.7	274.5	21.2	218.8	7.1	4.1	4.33	2.78	2.82	1.81	1.43	0.21	1.34	0.06
:Mars00B26Mar99LR:	5	-6.9	4.8	1.79	1.11	261.7	272.6	29.7	218.6	6.9	5.7	5.03	1.77	3.28	1.15	1.08	0.14	1.25	0.07
:Mars20SB25Mar99LR:	25	-9.2	6.1	1.45	0.31	244.3	242.9	8.8	215.3	16.1	13.2	12.1	5.31	6.58	2.89	2.18	0.55	1.32	0.08
:Mars20SB25Mar99LR:	5	-2.9	4.1	1.48	0.27	244.3	243.9	7.7	215.8	16.6	10.5	10.77	3.31	5.86	1.8	2.65	0.41	1.29	0.07
:Mars20SB29Mar99LR_3:	25	-9.3	2.9	1.03	0.08	244.3	248.6	3.3	221.1	21.9	5.3	4.13	2.14	2.42	1.25	0.68	0.3	1.08	0.04
:Mars20SB29Mar99LR_3:	5	-9.5	3.1	1.04	0.1	244.3	248.3	4	221.9	22.7	6.2	4.47	1.34	2.62	0.78	0.48	0.11	1.07	0.03
:Mars40SB26Mar99LR_A:	25	-13	7	1	0	203.4	231.2	2.6	194.4	13.2	9.6	3.56	3.39	2.03	1.94	1.87	0.47	1.34	0.06
:Mars40SB29Mar99LR_3:	25	-4.8	9.2	1	0	203.4	232.8	3.3	193.7	12.5	11.1	4.51	7.15	2.51	3.99	3.16	1.16	1	0
:Mars40SB29Mar99LR_3:	5	-10.5	8.7	1	0	203.4	234.4	3.3	195.9	14.7	15.9	11.91	5.28	6.64	2.94	3.5	0.51	1	0
:Mars40SA26Mar99LR:	25	-6	22.4	1	0	203.4	203.6	0.9	189.3	8.1	5.7	3.2	3.76	3.92	4.59	1	0	1	0
:Mars40SA26Mar99LR:	5	14.2	12.4	1	0	203.4	204.6	1	192.7	11.5	6.8	8.77	6.8	10.73	8.32	1	0	1	0
:Mars40SA29Mar99LR:	25	-7.1	3.3	0.75	0.21	203.4	212.3	8.2	181.1	-0.1	3.1	2.77	1.14	2.03	0.84	0.58	0.23	1.19	0.04
:Mars40SA29Mar99LR:	5	-2.6	5.1	0.8	0.33	203.4	214	12.4	181.8	0.6	4.8	1.01	0.67	0.74	0.49	0.46	0.04	1.18	0.05
:Mars40SC29Mar99LR:	25	-11.1	4.3	1	0	203.4	224.4	0.4	189.5	8.4	4.6	5.61	1.87	3.2	1.07	0.3	0.01	1	0
:Mars40SC29Mar99LR:	5	-8.4	4.1	1	0	203.4	225	0.4	187.5	6.4	5.5	5.58	1.15	3.19	0.66	0.68	0.02	1	0

Table A3.6. June 2003 Analysis Details

filename	Reso-lution. (MHz)	Fit Doppler Shift	1 sig	Fit Scale Factor	1 sig	MGS Tsurf K	Fit Tsurf K	1 sig	Fit Tlayer1 K	MGS delta K	1 sig	O3 MF x1E-8	1 sig	O3 CD mu-atm	1 sig	Terr CO2 Scale Factor	1 sig	Terr O3 Scale Factor	1 sig
:Mars10Jun03_40N_MGS_LR:	25	12.8	5.7	1.14	0.07	235.4	242.9	2.2	206.3	3.3	1.8	0.99	0.63	1.04	0.66	0.17	0.03	1.09	0.02
:Mars10Jun03_40N_MGS_LR:	5	-1.5	11	1.12	0.13	235.4	249.2	4.9	211.1	8.1	4.1	0.49	0.35	0.51	0.37	1.28	0.1	1.13	0.03
:Mars14Jun03_20N_45E_LR:	25	8.4	3.2	1.32	0.04	269.4	261.1	1.4	224.5	-5	1.6	1.24	0.32	1.23	0.32	0.54	0.03	1.06	0.01
:Mars14Jun03_20N_45E_LR:	5	20.6	2.6	1.2	0.08	269.4	256.9	2.9	222.6	-6.9	3.6	1.02	0.19	1.01	0.19	0.51	0.03	1.1	0.02
:Mars10Jun03_0S_55E_LR:	25	-1.1	4.4	2.07	0.14	285.7	251.6	3.1	230.1	-9.8	6.5	0.01	0	0.01	0	1.18	0.19	1.14	0.03
:Mars10Jun03_0S_55E_LR:	5	-1.1	6.7	2.12	0.24	285.7	251.3	4.8	227.7	-12.2	9	0.01	0	0.01	0	1.02	0.23	1.13	0.04
:Mars14Jun03_20S_60E_LR:	25	-1.7	2.5	1.87	0.09	287.1	252.9	2.2	240	2	7.2	1.21	0.86	0.72	0.51	0.13	0.01	1.11	0.02
:Mars14Jun03_20S_60E_LR:	5	0.2	3.2	1.86	0.12	287.1	253.5	3.1	241.1	3.1	8.5	0.78	0.42	0.47	0.25	0.12	0.03	1.13	0.02
:Mars12Jun03_40S_60E_LR:	25	-0.3	2.8	2.46	0.18	280.5	255.3	3.1	228.2	-3.9	5.3	1.83	1.28	1.12	0.78	0.08	0.01	1.11	0.02
:Mars12Jun03_40S_60E_LR:	5	-3.1	3.5	2.6	0.3	280.5	257.8	5	230.3	-1.8	7.1	2.63	0.64	1.61	0.39	0.19	0.02	1.09	0.03
:Mars12Jun03_60S_60E_LR:	25	0	0	3.81	0.97	209.6	233.5	9.1	212.5	0	0	4.96	2.56	3.04	1.57	0.37	0.12	0.96	0.06
:Mars12Jun03_60S_60E_LR:	5	0	0	3.7	1.14	209.6	234.6	11	212.5	0	0	5.9	1.26	3.61	0.77	0.37	0	1.02	0.06

References

Abbas, M. M., V. G. Kunde, M. J. Mumma, T. Kostiuk, D. Buhl and M. A. Frerking 1979. Stratospheric sounding by infrared heterodyne spectroscopy**.** *JGR 84*, 2681-2690.

Anderson, G. P., S. A. Clough, F. X. Kneizys, J. H. Chetwynd and E. P. Shettle 1986. AFGL Atmospheric Constituent Profiles (0-120km). AFGL-TR-86-0110, Environmental Research Papers, No. 984.

Atreya, S. K. and Z. G. Gu 1994. Stability of the martian atmoshere: Is heterogeneous catalysis essential? *J. Geophys. Res*. **99**, 13,133-13,145.

Atreya, S. K. and Z. G. Gu 1995. Photochemistry and stability of the atmosphere of Mars. *Adv. Space Res*. **16**, (6)57-(6)68.

Atreya, S. K., A. S. Wong, N. O. Renno, W. M. Farrell, G. T. Delory, D. Sentman, S. Cummer, J. Marshall, S. Rafkin, D. Catling 2004. Oxidant Enhancement in Martian dust devils and storms: II. Electrochemistry and oxidant production. *BAAS*, 36.4102A.

Barth, C. A. and C. W. Hord 1971. Mariner ultraviolet spectrometer: topography and polar cap. *Science* **173**, 197-201.

Barth, C. A., C. W. Hord, A. I. Stewart, A. L. Lane, M. L. Disk, G. P. Anderson 1973. Mariner 9 ultraviolet spectrometer experiment: seasonal variations of ozone on Mars. *Science* **179**, 795-796.

Bertaux, J. -L., D. Fonteyn, O. Korablev, E. Chassefière, E. Dimarellis, J. P. Dubois, A. Hauchecorne, M. Cabane, P. Rannou, A. C. Levasseur-Regourd, G. Cernogora, E. Quemerais, C. Hermans, G. Kockarts, C. Lippens, M. De. Maziere, D. Moreau, C. Muller, B. Neefs, P. C. Simon, F. Forget, F. Hourdin, O. Talagrand, V. I. Moroz, A. Rodin, B. Sandel, and A. Stern 2000. The study of the Martian atmosphere from top to bottom with SPICAM light on Mars Express. *Planet. Space Sci*. **48**, 1303-1320.

Bertaux, J. -L., O Korablev, E. Quemerais, S. Perrier, A. Fedorova, C. Muller, and The Spicam Team 2004. Spicam on Mars Express: First results and first observations of water ice at south pole. In *35th Lunar and Planetary Science Conference, March 15-19, 2004, League City, Texas.* Abstract no. 2178.

Blamont, J. E., and E. Chassefiére 1993. First detection of ozone in the middle atmosphere of Mars from solar occultation measurements. *Icarus* **104**, 324-336.

Clancy, R. T. and H. Nair 1996. Annual (perihelioin-aphelion) cycles in the photochemical behavior of the global Mars atmosphere. *Journal Geophys. Res.* **101**, 12,785-12,790.

Clancy, R. T., B. J Sandor and G. H. Moriarty-Schieven 2004. A measurement of the 362 GHz absorption line of Mars atmospheric H_2O_2. *Icarus* **168**, 116-121.

Clancy, R. T., M. J. Wolff, P. B. James, E. Smith, Y. N. Billawala, S. W. Lee, and M. Callan 1996. Mars ozone measurements near the 1995 aphelion: Hubble Space Telescope ultraviolet spectroscopy with the Faint Object Spectrograph. *Journal Geophys. Res.* **101**, 12,777-12,783.

Clancy, R. T., M. J. Wolff, and P. B. James 1999. Minimal aerosol loading and global increases in atmospheric ozone during the 1996-1997 Martian northern spring season. *Icarus* **138**, 49-63.

Dlugokencky, E. J. and A. R. Ravishankara 1992. Laboratory measurements of direct ozone loss on ice and doped-ice surfaces. *Geophys. Res. Lett*. **19**, 41-44.

Edwards, D. P. 1992. GENLN2: A general line-by-line atmospheric transmittance and radiance model: Version 3.0 description and users guide, Rep. NCAR/TN-367+STR, Natl. Cent. for Atmos. Res., Boulder, Colo.

Encrenaz, Th., B. Bézard, T. K. Greathouse, M. J. Richter, J. H. Lacy, s. K. Atreya, A. S. Wong, S. Lebonnois, F. Lefèvre and F. Forget 2004. Hydrogen peroxide on Mars: evidence for spatial and seasonal variations. *Icarus* **170**, 424-429.

Encrenaz, Th., T. K. Greathouse, B. Bézard, S. K. Atreya, A. S. Wong, M. J. Richter and J. H. Lacy 2002. A stringent upper limit of the H_2O_2 abundance in the Martian atmosphere. *Astron. Astrophys*. **396**, 1037-1044.

Espenak, F., M. J. Mumma, and T. Kostiuk 1991. Ground-based infrared measurements of the global distribution of ozone in the atmosphere of Mars. *Icarus* **92**, 252-262.

Fast, K., T. Kostiuk, P. Romani, F. Espenak, T. Hewagama, A. Betz, R. Boreiko and T. Livengood 2002. Temporal behavior of stratospheric ammonia abundance and temperature following the SL9 impacts. *Icarus* **156**, 485-497.

Fast, K. E., T. Kostiuk, F. Espenak, T. A. Livengood, T. Hewagama, and M. F. A'Hearn 2004. Stratospheric ozone profiles from Mauna Kea, Hawai'i (19.8°N, 155.5°W) using infrared heterodyne spectroscopy, 1988-2003, *Geophys. Res. Lett*. **31**, L08109, doi:10.1029/2004GL019443.

Forget, F., F. Hourdin, R. Fournier, C. Hourdin, O. Talagrand, M. Collins, S. R. Lewis, P. L. Read and J. –P. Hout 1999. Improved general circulation models of the Martian atmosphere from the surface to above 80 km. *J. Geophys. Res*., **104**(E10), 24,155-24,176.

Frerking, M.A. and D. J. Muehlner 1977. Infrared heterodyne spectroscopy of atmospheric ozone**.** *Appl. Opt. 16*, 526-528.

Fukunishi, H., S. Okano, M. Taguchi and T. Ohnuma 1990. Laser heterodyne spectroscopy using liquid nitrogen cooled tunable diode laser for remote measurements of atmospheric O_3 and N_2O**.** *Appl. Opt. 29*, 2722-2728.

Goldstein, J., M. J. Mumma, T. Kostiuk, D. Deming, F. Espenak, and D. Zipoy 1991. Absolute wind velocities in the lower thermosphere of Venus using infrared heterodyne spectroscopy. *Icarus* **94**, 45-63.

Hewagama, T., J. Goldstein, D. Buhl, F. Espenak, K. Fast, T. Kostiuk, T. Livengood, F. Schmuelling, T. Sodroski. 2005 Beam integrated high-resolution spectra: plane parallel, extended, clear atmospheres. In preparation.

James, P. B., B. A. Cantor, M. J. Wolff, S. W. Lee, R. T. Clancy, J. F. Bell, III, L. J. Martin 1997. Hubble Space Telescope observations of Martian north polar cap: 1990-1997. In *Mars telescopic observations workshop II,* A. L. Sprague, J. F. Bell, III, eds. LPI Technical Report, LPITR 97-03. Houston, p17.

Johnson, B. J., S. J. Oltmans, H. Vömel, H. G. J. Smit, T. Deshler and C. Kroger 2002. Electrochemical ozonesonde (ECC) pump efficiency measurements and tests on the sensitivity to ozone of buffered and unbuffered ECC sensor cathode solutions, *JGR 107*, 4393.

Komhyr, W. D., G. C. Reinsel, R. D. Evans, D. M. Quincy, R. D. Grass and R. K. Leonard 1997, Total ozone trends at sixteen NOAA/CMDL and cooperative Dobson spectrophotometer observations during 1979-1996*, GRL 24*, 3225-3228.

Koide, M., M. Taguchi, H. Fukunishi and S. Okano 1995. Ground-based remote sensing of methane height profiles with a tunable diode laser heterodyne spectrometer, *GRL 22*, 401-404.

Kong, T. Y. and M. B. McElroy 1977a. Photochemistry of the martian atmosphere. *Icarus* **32**, 168-189.

Kong, T. Y. and M. B. McElroy 1977b. The global distribution of O_3 on Mars. *Planet. Space Sci*. **25**, 839-857.

Kostiuk, T. 1994. Physics and chemistry of upper atmospheres of planets from infrared observations. *Infrared Phys. Technol.* **35**, 243–266.

Kostiuk, T., D. Buhl, F. Espenak, P. Romani, G. Bjoraker, K. Fast, T. Livengood, and D. Zipoy 1996. Stratospheric ammonia on Jupiter after the SL9 collisions. *Icarus* **121**, 431-441.

Kostiuk, T., F. Espenak, M.J. Mumma, D. Deming, and D. Zipoy 1987. Variability of ethane on Jupiter. *Icarus* **72**, 394-410.

Kostiuk, T., K. Fast, T. A. Livengood, J. Goldstein, T. Hewagama, D. Buhl, F. Espenak, and K. H. Ro 1997. Ethane abundance on Titan. *Planet. Space Sci.,* **45**, 931-939.

Kostiuk, T., K. Fast, T. A. Livengood, T. Hewagama, J. Goldstein, F. Espenak, and D. Buhl 2001. Direct measurement of winds on Titan. *Geophys. Res. Lett*. **28**, 2361-2364.

Kostiuk, T., and M. J. Mumma 1983. Remote sensing by IR heterodyne spectroscopy. *Appl. Opt. 17*, 2644-2654.

Krasnopolsky, V. A. 1986. *Photochemistry of the atmospheres of Mars and Venus*. Springer-Verlag, Berlin.

Krasnopolsky, V. A. 1993. Photochemistry of the Martian atmosphere (mean conditions). *Icarus* **101**, 313-332.

Krasnopolsky, V. A. 1995. Uniqueness of a solution of a steady-state photochemical problem: Applications to Mars *JGR* **100**, 3263-3276.

Krasnopolsky, V. A. 2003*a*. Mapping of Mars O_2 1.27 μm dayglow at four seasonal points. *Icarus* **165**, 315-325.

Krasnopolsky, V. A. 2003*b*. Mars photochemistry: weak points and search for solutions. In *Sixth International Conference on Mars, July 20-25 2003, Pasadena, California,* abstract no. 3002.

Krasnopolsky, V. A. and G. L. Bjoraker 2000. Mapping of Mars $O_2(^1\Delta)$ dayglow. *JGR* **105**, 20,179-20,188.

Krasnopolsky, V. A. and V. A. Parshev 1979. Ozone and photochemistry of the Martian lower atmosphere. *Planet. Space Sci.* **27**, 113-120.

Krasnopolsky, V. A., V. A. Parshev, A. A. Krysko, and V. N. Rogachev 1980. Structure of the lower and middle atmosphere of Mars based on the Mars 5 ultraviolet photometry. *Cosmic Res.* **18***,* 94-113.

Lane, A. L., C. A. Barth, C. W. Hord, and A. I. Stewart 1973. Mariner 9 ultraviolet spectrometer experiment: Observations of ozone on Mars. *Icarus* **18**, 102-108.

Leblanc, T. and I. S. McDermid 2000. Stratospheric ozone climatology from lidar measurements at Table Mountain (34.4°N, 117.7°W) and Mauna Loa (19.5°N, 155.6°W)**.** *JGR 105*, 14,613-14,625.

Lefèvre, F., S. Lebonnois, F. Montmessin, F. Forget 2004. Three-dimensional modeling of ozone on Mars. *J. Geophys. Res*., **109**, E07004, doi:10.1029/2004JE002268.

Lindner, B. L. 1995. Mars ozone: Mariner 9 revisited. *Icarus* **113**, 213-216.

Livengood, T., T. Hewagama, T. Kostiuk, K. Fast, and J. Goldstein 2002, Improved determination of ethane (C_2H_6) abundance in Titan's stratosphere, *Icarus* **157,** 249-253.

McDermid, I. S., T. D. Walsh, A. Deslis and M. White 1995. Optical systems design for a stratospheric lidar system**.** *Appl. Opt. 34*, 6201-6210.

McElroy, C. T., A. Goldman, P. F. Fogal and D. G. Murcray 1990. Heterodyne spectrophotometery of ozone in the 9.6 μm band using a tunable diode laser. *JGR 95*, 5567-5575.

McElroy, M. B., and T. M. Donahue 1972. Stability of the Martian atmosphere. *Science* **177**, 986-988.

McPeters, R. D., D. J. Hofman, M. Clark, L. Fllynn, L. Froidevaux, M. Gross, b. Johnson, G. Koenig, X. Liu, S. McCermid, R. McGee, F. Murcray, M. J. Newshurch, S. Oltmans, A. Parrish, R. Schnell, U. Singh, J. J. Tsou, T. Walsh and J. M. Zawodny 1999. Results from the 1995 stratospheric ozone profile intercomparison at Mauna Loa**.** *JGR* **104***,* 30,505-30,514.

Moreau, D., L. W. Esposito and G. Brasseur 1991. The chemical composition of the dust-free martian atmosphere: Preliminary results of a two-dimensional model. *J. Geophys. Res.* **96**, 7933-7945.

Mouanda, J. C., A. Hamdouni, D. Courtois and C. Thiebeaux 1996. Total ozone determination by infrared heterodyne spectrophotometry, *Infrared Phys. Technol. 37*, 575–578.

Mumma, M. J., J. D. Rogers, T. Kostiuk, D. Deming, J. J. Hillman and D. Zipoy 1983. Is there any chlorine monoxide in the stratosphere?, Science 221, 268.

Nair, H. M. Allen, A. D. Anbar, Y. L. Yung, and R. T. Clancy 1994. A photochemical model of the Martian atmosphere. *Icarus* **111**, 124-150.

Noll, K. S., R. E. Johnson, A. L. Lane, D. L Domingue, H. A. Weaver 1996. Detection of ozone on Ganymede. *Science* **273**, 341-343.

Novak, R. E., M. J. Mumma, M. A. DiSanti and N. Dello Russo 2002. Mapping of ozone and water in the atmosphere of Mars near the 1997 aphelion. *Icarus* **158**, 14-23.

Noxon, J. F., W. A. Traub, N. P. Carleton, and P. Connes 1976. Detection of O_2 dayglow emission from Mars and the Martian ozone abundance. *Ap. J.* **207**, 1025-1035.

Orton, Glenn, and 57 co-authors 1995. Collision of comet Shoemaker-Levy 9 with Jupiter observed by the NASA Infrared Telescope Facility, *Science* **267**, 1277-1288.

Parkinson, T. M., and D. M. Hunten 1972. Spectroscopy and aeronomy of O_2 on Mars. *J. Atmos. Sci.* **29**, 1380-1390.

Post, D. E. and L. G. Votta 2005. Computational science demands a new paradigm. *Phys. Today* **58**, 35-41.

Rizk, B., W. K. Wells, D. M. Hunten, C. R. Stoker, R. S. Freedman, T. Rouch, J. B. Pollack, and R. M. Haberle 1991. Meridional Martian water abundance profiles during the 1988-1989 season. *Icarus* **90**, 205-213.

Shimazaki, T. 1981. A model of temporal variations in ozone density in the Martian atmosphere. *Planet. Sp. Sci.* **29**, 21-33.

Shimazaki, T. 1989. Photochemical stability of CO_2 in the Martian atmosphere: Reevaluation of the eddy diffusion coefficient and the role of water vapor. *J. Geomag. Geoelectr.* **41**, 273-301.

Shimazaki, T. and M. Shimizu 1979. The seasonal variation of ozone density in the Martian atmosphere. *J. Geophys. Res.* **84**, 1269-1276.

Smith, D. E., M. T. Zuber, H. V. Frey, J. B. Garvin, J. W. Head, D. O. Muhleman, G. H. Pettengill, R. J. Phillips, S. C. Solomon, H. J. Zwally, W. B. Banerdt, T. C. Duxbury, M. P. Golombek, F. G. Lemoine, G. A. Neumann, D. D. Rowlands, O. Aharonson, P. G. Ford, A. B. Ivanov, P. J. McGovern, J. B. Abshire, R. S. Afzal and X. Sun 2001. Mars Orbiter Laser Altimeter (MOLA): Experiment summary after the first year of global mapping of Mars, *J. Geophys. Res.,* **106**, 23,689-23,722.

Smith, M. D. 2002. The annual cycle of water vapor on Mars as observed by the Thermal Emission Spectrometer, *J. Geophys. Res.,* **107**(E11), 5115, doi:10.1029/2001JE001522.

Smith, M. D. 2004. Interannual variability in TES atmospheric observations of Mars during 1999-2003. *Icarus* **167**, 148-165.

Smith, M. D., J. C. Pearl, B. J. Conrath, and P. R. Christensen 2001. Thermal Emission Spectrometer results: Mars atmospheric thermal structure and aerosol distribution. *J. Geophys. Res* **106**, 23,929-23,945.

Sonnabend, G., D. Wirtz, F. Schmülling and R. Schieder 2002. Tunable heterodyne infrared spectrometer for atmospheric and astronomical studies, *Appl. Opt. 41*, 2978-2984.

Sprague, A. L., D. M. Hunten, R. E. Hill, B. Rizk, and W. K. Wells 1996. Martian water vapor, 1988-1995. *J. Geophys. Res* **101**, 23,229-23,241.

Sprague, A. L., D. M. Hunten, R. E. Hill, L. R. Doose, and B. Rizk 2001. Water vapor abundances over Mars north high latitude regions: 1996-1999. *Icarus* **154**, 183-189.

Tillman, J. E., N. C. Johnson, P. Guttorp, D. B. Percival 1993. The Martian annual atmospheric pressure cycle – Years without great dust storms. *J. Geophys. Res* **98**, 10,963-10,971.

Wehrbein, W. M., C. W. Hord, and C. A. Barth 1979. Mariner 9 ultraviolet spectrometer experiment: Vertical distribution of ozone on Mars. *Icarus* **38**, 188-199.

Yung, Y. L. and W. B. DeMore 1999. *Photochemistry of planetary atmospheres*. Oxford University Press: New York, Oxford.

Zurek, R. W., J. R. Barnes, R. M. Haberle, J. B. Pollack, J. E. Tillman and C. B. Leovy 1992. Dynamics of the atmosphere of Mars. In *Mars*, H. H. Kieffer, B. M. Jakosky, C. W. Snyder, M. S. Matthews, eds. The University of Arizona Press, Tucson. 839.

NAME: **KELLY ELIZABETH FAST**

DATE OF BIRTH: 09/10/68, Hollywood, California, USA

PROFESSIONAL ADDRESS: Code 693, NASA/Goddard Space Flight Center
Greenbelt, MD 20771

POSITIONS HELD:
2001-2005, Student Trainee - Astronomy, NASA/GSFC
1993-2001, Faculty Research Assistant at NASA/GSFC,
University of Maryland, Dept. of Astronomy
1992, Research Assistant at NASA/GSFC,
University of Maryland, Dept. of Astronomy
1990-1992, Teaching Assistant,
University of Maryland, Dept. of Astronomy
1988-1990 (academic year), Research Assistant,
Plasma Physics Laboratory, UCLA
1988-1989 (summer), Summer Student,
Los Alamos National Laboratory

EDUCATION:
2005, Ph.D., Astronomy, University of Maryland, College Park
1993, M.S., Astronomy, University of Maryland, College Park
1990, B.S., Astrophysics, University of California, Los Angeles

MEMBERSHIPS:
American Geophysical Union
Division for Planetary Sciences of the
American Astronomical Society

RELEVANT PUBLICATIONS:

Fast, K. E., T. Kostiuk, F. Espenak, T. A. Livengood, T. Hewagama, M. F. A'Hearn 2004. Stratospheric ozone profiles from Mauna Kea, Hawai'i (19.8°N, 155.5°W) using infrared heterodyne spectroscopy, 1988-2003. *Geophys. Res. Lett.*, **31**, No. 8, L08109.

Livengood, T., T. Hewagama, T. Kostiuk, K. Fast, J. Goldstein 2002. Improved determination of ethane (C_2H_6) abundance in Titan's stratosphere. *Icarus* **157,** 249-253.

Fast, K., T. Kostiuk, P. Romani, F. Espenak, T. Hewagama, A. Betz, R. Boreiko, T. Livengood 2002. Temporal behavior of stratospheric ammonia abundance and temperature following the SL9 impacts. *Icarus* **156,** 485-497.

Kostiuk, T., K. Fast, T. A. Livengood, T. Hewagama, J. Goldstein, F. Espenak, and D. Buhl 2001. Direct measurement of winds on Titan. *Geophys. Res. Lett.* **28**, 2361-2364.

Livengood, T., K. Fast, T. Kostiuk, F. Espenak, D. Buhl, J. Goldstein, T. Hewagama, and K. H. Ro 1999. Refraction by the Earth's atmosphere near 12 microns, *PASP*, **111**, 512.

Kostiuk, T., K. Fast, T. A. Livengood, J. Goldstein, T. Hewagama, D. Buhl, F. Espenak, and K. H. Ro 1997. Ethane abundance on Titan. *Planet. Space Sci.* **45**, 931-939.

Deming, D., D. Reuter, D. Jennings, G. Bjoraker, G. McCabe, K. Fast, and G. Wiedemann 1997. Observations and analysis of longitudinal thermal waves on Jupiter, *Icarus* **126**, 301-312.

Kostiuk, T., D. Buhl, F. Espenak, P. Romani, G. Bjoraker, K. Fast, T. Livengood, and D. Zipoy 1996. Stratospheric ammonia on Jupiter after the SL9 collisions. *Icarus* **121**, 431-441.

Orton, G. and 57 colleagues (including K. Fast) 1995. Collision of comet Shoemaker-Levy 9 with Jupiter observed by the NASA Infrared Telescope Facility, *Science* **267**, 1277-1288.

(as K. Kawan)
Cheung, P. Y., D. F. DuBois, T. Fukuchi, K. Kawan, H. A. Rose, D. Russell, T. Tanikawa, and A. Y. Wong 1992. Investigation of strong Langmuir turbulence in ionospheric modification, *JGR* **97**, 10575-10600.